TU **TECHNISCHE**
UNIVERSITÄT
WIEN

DOCTORAL THESIS

Spatial Resolved Dispersive X-Ray Absorption Spectroscopy and Coded Aperture X-Ray Fluorescence Imaging

submitted in satisfaction of the requirements for the degree of
Doctor of Technical Sciences
supervised by

Ao. Univ. Prof. Dipl.-Ing. Dr. techn. Christina Streli
E141 - Atominstitut

submitted at the Vienna University of Technology
Faculty of Physics

by

Anicó Kulow
Matr.-Nr. 01652081
Eisenacher Str. 66
12109 Berlin
Germany

Berlin, _____   _____

Abstract

X-ray based spectroscopic methods play a crucial role in material characterization. This is due to the fact that they provide non-destructive and fast information about the composition, the structure and the chemical state of various samples. Especially synchrotron-based methods are of unique usefulness, due to the advantageous properties of synchrotron radiation, e.g. energy tunability, high brightness, polarization and collimation, possible small beam size, and high power. This is of great importance in many fields of research, such as physics, chemistry, biology, and materials sciences. Especially the development of new materials would not be possible without a thorough characterization and investigation of these materials, during all stages of their lifetime, from synthesis to use and degradation.

X-ray fluorescence (XRF) spectroscopy is a valuable tool for the qualitative and quantitative determination of the elemental content in a sample, whereas X-ray absorption fine structure (XAFS) spectroscopy can provide information about the oxidation state, the local coordination geometry and the electron configuration of an element of interest in the sample, also on amorphous phases. This method entails both XANES (X-ray absorption near edge structure) and EXAFS (extended X-ray absorption fine structure) spectroscopy.

The BAM*line* at BESSY II is a hard X-ray beamline that provides among others set-ups for XAFS and XRF spectroscopy. It has two main optical elements, a double-crystal monochromator (DCM) that has a narrow bandwith $\Delta E/E$ of about $2 \cdot 10^{-4}$ and that is well suited for experiments where a high energy resolution is needed, such as sequential XAFS experiments, and a double-multilayer monochromator (DMM) with a bandwidth of about $1.7 \cdot 10^{-2}$ with a considerably higher photon flux, that is used for XRF experiments. Unlike most beamlines at third generation synchrotron facilities, the BAM*line* is no fixed end station, but is very universal. The experiments can be adapted to the needs of the users. The experimental possibilities are steadily expanded and improved. This comprises the implementation of new experimental setups. This work deals with new solutions for experimental requirements in the fields of the investigation of dynamic processes and X-ray imaging.

Time-resolved XAFS can be employed when real-time monitoring is necessary. This can be the case when chemical reactions are investigated, changes during a synthesis

process should be followed, or for the evaluation of the performance of a material under certain, possibly changing, conditions. Different beamlines around the world are specialized in time-resolved XAFS experiments. Usually, there are high requirements concerning the instrumentation.

One aim of this work was the development of a new setup for time- and laterally resolved XAFS measurements, based on the principle of dispersive XAFS. This setup is scanning free, stable, inexpensive, and straightforward to adjust for probing different elements. An incoming energetic broadband beam passes the sample and is diffracted afterwards by a bent Si (111) crystal. Thus, the different energies are spatially separated and can be detected by an area sensitive detector. The intensity pattern of the recorded image is a direct measure for the absorption in the sample. As all energies are recorded in a 'single shot', the acquisition time for a spectrum can be considerably reduced compared to conventional XAFS measurements. Depending on the photon flux and the required signal-to-noise-ratio (SNR), XANES and/or EXAFS spectra can be recorded with a time resolution of down to 1 s. For the proof of principle, reference Fe and Cu metal foils were measured at the BAM*line*. The first application was the time-resolved investigation of the early stages of zinc(II)2-methylimidazolate (ZIF-8) crystallization. Here, intermediates that are formed during the ZIF-8 synthesis could be identified.

Another important and increasing field for materials characterization is X-ray imaging; this includes the investigation of the elemental distributions, chemical states, and textural properties. X-ray imaging is used for example in astrophysics, biology, material sciences, and for the investigation of archaeological objects or art work. The imaging can be performed in scanning mode, where the sample is investigated point by point, or with full field methods.

Considering this, the second part of this work describes the implementation of a method for full field X-ray fluorescence imaging with coded apertures. Expensive and complicated X-ray optics, that are usually used for full field imaging, are replaced with a coded aperture that consists of many pinholes drilled in an X-ray opaque material. Coded apertures are inexpensive to fabricate, energy independent, and easy to use. The working principle is the same as with a pinhole camera, but the multiple holes allow a higher photon flux compared to a single pinhole or even a polycapillary optic, thus allowing the reduction of measurement time.

The image is recorded by an energy-sensitive 2D-detector, a pnCCD, and consists of overlapping projections of the object. A reconstruction step is performed to retrieve the object information. Different reconstruction methods are presented; the deconvolution with an antimask, an iterative reconstruction, an evolutionary algorithm, and a machine learning approach.

Firstly, extensive simulations have been performed to develop and improve the recon-

struction algorithms. In a second step, different samples were measured at the BAM*line* and could be successfully reconstructed with different reconstruction methods.

This method can be used for the investigation of the element distribution, for example in newly developed materials such as high entropy alloys (HEAs) or metalorganic frameworks (MOFs), but also for the investigation of the accumulation of elements in biological tissue, or the analysis of the elemental composition in artwork or archaeological objects for provenance research.

List of publications resulted from this thesis:

- A. Kulow, S. Witte, S. Beyer, A. Guilherme Buzanich, M. Radtke, U. Reinholz, H. Riesemeier, and C. Streli, *A new experimental setup for time- and laterally-resolved X-ray absorption fine structure spectroscopy in a 'single shot'.* **Journal of Analytical Atomic Spectrometry**, 2019, **34**(1): p. 239 - 246

- A. Kulow, A. Guilherme Buzanich, U. Reinholz, C. Streli, and M. Radtke, *On the way to full-field X-ray fluorescence spectroscopy imaging with coded apertures.* **Journal of Analytical Atomic Spectrometry**, 2020, **35**(2): p. 347 - 356

- A. Kulow, A. Guilherme Buzanich, U. Reinholz, F. Emmerling, S. Hampel, U. E. A. Fittschen, C. Streli, and M. Radtke, *Comparison of three reconstruction methods based on deconvolution, iterative algorithm and neural network for X-ray fluorescence imaging with coded aperture optics.* **Journal of Analytical Atomic Spectrometry**, 2020, **35**(7): p. 1423 - 1434

Kurzfassung

Röntgenbasierte spektroskopische Methoden spielen eine entscheidende Rolle bei der Materialcharakterisierung, da sie zerstörungsfrei und schnell Informationen über die Zusammensetzung, die Struktur und den chemischen Zustand, wie z.B. die Oxidationsstufe, verschiedener Proben liefern können. Besonders Synchrotron-basierte Methoden sind aufgrund der vorteilhaften Eigenschaften der Synchrotronstrahlung, wie z.B. Möglichkeit der Auswahl monochromatischer Strahlung, hohe Brillianz, Polarisation und Kollimation und mögliche kleine Strahlgröße (Mikro-Fokus), von einzigartigem Nutzen. Dies ist in vielen Forschungsbereichen wie Physik, Chemie, Biologie und Materialwissenschaften von großer Bedeutung. Insbesondere die Entwicklung neuer Materialien wäre ohne eine gründliche Charakterisierung und Untersuchung dieser Materialien in allen Phasen ihrer Lebensdauer, von der Synthese über die Verwendung bis hin zum Abbau, nicht möglich.

Die Röntgenfluoreszenzspektroskopie (X-ray fluorescence spectroscopy, XRF spectroscopy) ist ein wertvolles Werkzeug für die qualitative und quantitative Bestimmung des Elementgehalts in einer Probe, während die Röntgenabsorptions-Feinstrukturspektroskopie (X-ray absorption fine structure spectroscopy, XAFS spectroscopy) Informationen über den Oxidationszustand, die lokale Koordinationsgeometrie und die Elektronenkonfiguration des untersuchten Elements in der Probe liefern kann. Dabei kann die Probe sowohl kristallin, als auch flüssig oder amorph sein. Zu dieser Methode gehören sowohl die XANES (von englisch: X-ray absorption near edge structure)- als auch die EXAFS (von englisch: extended X-ray absorption fine structure)-Spektroskopie.

Die BAM*line* bei BESSY II ist eine Beamline für den harten Röntgenbereich von etwa 4 keV bis etwa 60 keV, die u.a. die Möglichkeit für XAFS- und XRF-Spektroskopie bietet. Sie verfügt über zwei Monochromatoren, einen Doppelkristall-Monochromator (DCM) mit einer schmalen Bandbreite $\Delta E/E$ von etwa $2 \cdot 10^{-4}$, der sich gut für Experimente eignet, bei denen eine hohe Energieauflösung erforderlich ist, wie z.B. bei sequentiellen XAFS-Experimenten, und einen Doppel-Multilayer-Monochromator (DMM) mit einer Bandbreite von etwa $1.7 \cdot 10^{-2}$ mit einem wesentlich höheren Photonenfluss, der für XRF-Experimente verwendet wird.

Im Gegensatz zu den meisten Beamlines an Synchrotronanlagen der dritten Generation hat die BAM*line* keine feste Endstation, sondern ist sehr flexibel. Die Experimente können an die Bedürfnisse der Nutzer angepasst werden. Die Experimentiermöglichkei-

ten werden ständig erweitert und verbessert. Dazu gehört auch die Realisierung neuer Versuchsaufbauten. Es gibt eine wachsende Nachfrage nach Möglichkeiten der zeitaufgelösten Analyse von Prozessen und nach Röntgenbildgebungsverfahren, und diese Arbeit trägt mit der Entwicklung von entsprechenden Methoden zu beiden Feldern bei.

Zeitaufgelöste XAFS Spektroskopie kann eingesetzt werden, wenn Echtzeit-Monitoring erforderlich ist. Dies ist nötig, um chemische Reaktionen zu untersuchen, Änderungen während eines Syntheseprozesses zu verfolgen oder die Leistung eines Materials unter bestimmten, anwendungsnahen und möglicherweise sich verändernden Bedingungen zu bewerten. Verschiedene Beamlines auf der ganzen Welt sind auf zeitaufgelöste XAFS Spektroskopie spezialisiert. In der Regel werden hierbei hohe Anforderungen an die Instrumente gestellt.

Ein Ziel dieser Arbeit war daher die Entwicklung eines neuen Aufbaus für zeit- und ortsaufgelöste XAFS-Messungen, basierend auf dem Prinzip der dispersiven XAFS, der einfach an der BAM*line* implementiert werden kann. Bei dieser Methode müssen die Spektren nicht Punkt für Punkt aufgenommen werden, sondern können in einem 'single shot' mit Hilfe eines ortsauflösenden Detektors aufgezeichnet werden. Der Aufbau ist stabil, einfach zu justieren und an verschiedene Energien anzupassen, um Proben mit unterschiedlichen Elementen zu untersuchen. Ein einfallender Strahl eines gewählten Energiefensters fällt auf die Probe, die die unterschiedlichen Energien unterschiedlich stark absorbiert. Der transmittierte Strahl wird anschließend von einem gebogenen Si(111)-Kristall reflektiert. Dabei werden die verschiedenen Energien aufgrund ihrer unterschiedlichen Bragg-Reflektionswinkel räumlich getrennt und können von einem flächenempfindlichen Detektor detektiert werden. Das Intensitätsmuster des aufgenommenen Bildes ist ein direktes Maß für die Absorption in der Probe. Dabei muss die Probe homogen und gleichmäßig dick sein, da sonst Unterschiede in der Absorption auftreten, die nicht von den Energien abhängig sind, und das Absorptionsspektrum überlagern. Da alle Energien in einem 'single shot' aufgezeichnet werden, kann die Aufnahmezeit für ein Spektrum im Vergleich zu herkömmlichen XAFS-Messungen erheblich verkürzt werden. Abhängig vom Photonenfluss und dem erforderlichen Signal-Rausch-Verhältnis (SNR) können XANES- und/oder EXAFS-Spektren mit einer Zeitauflösung von bis zu einer Minimalzeit von 1 s aufgenommen werden.

Um die Funktionsweise des Aufbaus zu demonstrieren, wurden an der BAM*line* Kupfer- und Eisen-Referenzfolien gemessen. Die erste Anwendung war die zeitaufgelöste Untersuchung der frühen Stadien der Kristallisation von Zink(II)2-Methylimidazolat (ZIF-8). Hier konnten Intermediate, die während der ZIF-8 Synthese auftreten, identifiziert werden.

Eine weitere wichtige Technik zur Charakterisierung von Materialien ist die Röntgenbildgebung; dazu gehört die Untersuchung von Elementverteilungen, der chemischen

Zustände und texturalen Eigenschaften. Die Röntgenbildgebung wird zum Beispiel in der Astrophysik, Biologie, den Materialwissenschaften und zur Untersuchung archäologischer Objekte oder Kunstwerke eingesetzt. Die Bildgebung kann im Rasterverfahren, bei dem die Probe Punkt für Punkt untersucht wird, oder mit Full-field-Methoden durchgeführt werden.

Der zweite Teil dieser Arbeit beschreibt die Implementierung einer Methode zur Full-field-Röntgenfluoreszenz-Bildgebung mit kodierten Aperturen. Teure und aufwendige Röntgenoptiken, die normalerweise für die Full-field-Bildgebung verwendet werden, werden durch eine kodierte Apertur ersetzt, die aus vielen Löchern in einem für die gewünschte Röntgenstrahlung undurchsichtigem Material besteht. Kodierte Aperturen können in einer üblichen mechanischen Werkstatt hergestellt werden, sind einfach in der Handhabung und die Transmission von Photonen ist energieunabhängig. Das Funktionsprinzip ist das gleiche wie bei einer Lochkamera, aber die große Anzahl an Löchern ermöglicht einen höheren Photonenfluss im Vergleich zu einer einzelnen Lochblende oder sogar einer Polykapillaroptik, wodurch die Messzeit verkürzt werden kann.

Das Bild wird von einem energieempfindlichen 2D-Detektor, hier einer pnCCD, aufgenommen und besteht aus überlappenden Projektionen des Objekts. Ein Rekonstruktionsschritt wird durchgeführt, um das Objekt zu rekonstruieren und die gewünschte Information, z.B. über die Elementverteilung, zu erhalten. In dieser Arbeit werden verschiedene Rekonstruktionsmethoden vorgestellt: die Dekonvolution mit einer Antimaske, eine iterative Rekonstruktion, ein genetischer Algorithmus und ein auf maschinellem Lernen basierender Ansatz.

Zunächst wurden umfangreiche Simulationen durchgeführt, um die Rekonstruktionsalgorithmen zu entwickeln und zu verbessern. In einem zweiten Schritt wurden verschiedene Proben an der BAM*line* vermessen und konnten mit verschiedenen Rekonstruktionsmethoden erfolgreich rekonstruiert werden.

Die Röntgenbildgebung mit kodierten Aperturen kann überall dort zum Einsatz kommen, wo die Elementverteilung einer Probe untersucht werden soll. Das können z.B. neu entwickelte Materialien wie Hochentropielegierungen (high entropy alloys, HEAs) oder Metallorganische Gerüstverbindungen (metalorganic frameworks, MOFs) sein, aber auch biologische Proben, bei denen die Anreicherung bestimmter Elemente untersucht werden soll, oder Kunstwerke, bei denen Untersuchungen der elementaren Zusammensetzung Hinweise auf die Herkunft geben können.

Acknowledgements

First of all I want to thank my supervisor Dr. Christina Streli who gave me the opportunity to create this work. I am very grateful for the good and uncomplicated communication and her support in all questions regarding the dissertation.

Special thanks go to my supervisors at BAM, Dr. Ana Guilherme Buzanich and Dr. Martin Radtke, who inspired me, leaded me, answered a million of questions and helped me a lot with the beamline experiments.

Many thanks to my experienced colleagues Dr. Heinrich Riesemeier and Dr. Uwe Reinholz, who know at least everything about the BAM*line* and synchrotron radiation and were always willing to share their knowledge with me.

Many practical work would not have been possible without all the helping hands at the beamline and in the workshop. Thank you, Monika Klinger, Bettina Röder, Christoph Naese, Jürgen Wenzel, Michael Sintschuk and Ralf Britzke.

Another important part of the daily work were Anke Kabelitz, Hannes Kulla, Kevin Linberg and Maria Heilmann, who were most of the time of my PhD my office mates. I'm very thankful for tea, talks and sweets!

I would also like to thank my colleagues at the division Structure Analysis and the head of this division, Franziska Emmerling, for a pleasant, inspiring and open working environment.

Thank you my wonderful parents and sister, who always believed in me, sometimes more than I did.

I want to thank Cauchy, Chebychev, Bernoulli and Cavalieri and the children they belong to. Sometimes, they even let me work at home, and they always made clear, what are the really important things in life.

This work would not have been possible without the caring support of Ronny Krüger, who saved the family's everyday life when I was not able to do so.

Contents

Appendix 142

List of Figures

List of Tables

Abbreviations

CAI	-	coded aperture imaging
CT	-	computed tomography
DCM	-	double-chrystal monochromator
DMM	-	double-multilayer monochromator
DXAFS	-	dispersive X-ray absorption fine structure
EDXRF	-	energy dispersive X-ray fluorescence
EXAFS	-	extended X-ray absorption fine structure
FOV	-	field of view
FWHM	-	full width at half maximum
HEA	-	high entropy alloy
LINAC	-	linear accelerator
ML	-	machine learning
MOF	-	metal organic framework
MURA	-	modified uniformly redundant array
QEXAFS	-	quick EXAFS
SNR	-	signal-to-noise ratio
URA	-	uniformly redundant array
WDXRF	-	wavelength dispersive X-ray fluorescence
WLS	-	wavelength shifter
XANES	-	X-ray absorption near edge structure
XAS	-	X-ray absorption spectroscopy
XRF	-	X-ray fluorescence
ZIF-8	-	zinc(II)2-methylimidazolate

Physical Constants

$$h \quad = \quad 6.626 \times 10^{-34}\,\mathrm{J\,s} \qquad \text{Planck's constant}$$

$$\hbar \quad = \quad \tfrac{h}{2\pi} = 1.055 \times 10^{-34}\,\mathrm{J\,s} \qquad \text{reduced Planck's constant}$$

$$c \quad = \quad 2.997\,924\,58 \times 10^{8}\,\mathrm{m\,s^{-1}} \qquad \text{velocity of light}$$

$$\text{d Si(111)} \quad = \quad 3.1356\,\text{Å} \qquad \text{lattice plane spacing of Si(111)}$$

1 Introduction

X-ray spectroscopic methods play a crucial role in science. They are indispensable tools for the non-destructive characterization of materials. Since the discovery of X-rays in the last decade of the 19th century, various methods have been developed to benefit from the outstanding properties of X-rays. These developments comprise the sources, the methods and instrumentation, such as detectors, optics, electronics and computer technology, as well as the evaluation tools.

One important step on the way to the actual success and importance of X-ray analytical methods was the discovery of synchrotron radiation in the 1940's, and even more the construction of dedicated synchrotron radiation facilities for research. Today, there are more than 50 lightsources all over the world, most of them so-called third generation lightsources that are optimized for modern insertion devices that produce synchrotron radiation with a high intensity and desired properties.

BESSY II, an electron storage ring in Berlin Adlershof, operated by the Helmholtz-Zentrum Berlin (HZB) is such a third generation synchrotron ligthsource. It provides extremely brilliant X-ray radiation to researchers from all over the world and from a a large variety of research fields.

One of the beamlines located in the storage ring of BESSY II is the BAM*line*. This is a high energy beamline planned and installed in 2000 by the Federal Institute for Materials Research and Testing (Bundesanstalt für Materialforschung und -prüfung, BAM) and the National Metrology Insitute of Germany (Physikalisch-Technische Bundesanstalt, PTB).

The BAM*line* is partially operated by the BAM division Structure Analysis. The main focus is the material characterization and the investigation of the structure property relationship. The group has a long experience in X-ray analytical methods, such as X-ray absorption and X-ray fluorescence spectroscopy for different applications in various fields. These include the investigation of the elemental composition of materials, *e.g.*, in the context of provenance research, the mapping of elements in a sample, *e.g.*, to investigate the accumulation of nutrients or contaminants, but also the determination of chemical states and the electronic structure.

The wide variety of experimental challenges requires a flexible beamline with setups that are adapted to the needs of the user and a continuous improvement of the existing

possibilities as well as the development of new methods and instrumentation.

The work presented in this dissertation deals with method development for application with synchrotron radiation.

One part was the development of a setup for dispersive X-ray absorption fine structure spectroscopy. This method allows the acquisition of an X-ray absorption spectrum in a single shot rather than the step-by-step collection of absorption values for the desired energy range. Thus, the acquisition time decreases considerably, and it is possible to record time series, *e.g.*, for the study of chemical reactions or monitoring of the behavior of material, *e.g.*, catalysts, under changing conditions. For the implementation at the BAM*line* it was necessary to build a stable and easy to install setup that can be used with different samples and can easily be adapted to different energies. The main part of the setup is a dispersive element, a Si (111) wafer, that is bent convexly by means of a so-called wafer bender, that has been developed especially for this purpose. An energetic broadband beam passes through a sample. The bent wafer reflects all transmitted energies under different angles, hence the different energies are spatially separated. An area sensitive CCD camera detects the different energies at different positions. The intensity pattern on the CCD screen is a direct measure for the absorption in the sample.

The second part of this work was the implementation of a method for full-field X-ray fluorescence imaging with coded apertures. The principle of coded aperture imaging, a method that was first used in astrophysics, is very simple. Multiple pinholes act each as a pinhole camera, allowing the projection of an object. A large number of pinholes increases the photon flux and hence also the statistics of the measurement. Usually, the projections of the individual pinholes overlap and the object is not recognizable in the original detector image. The information can be retrieved when the mask pattern is known using a reconstruction procedure. In the course of this work, different reconstruction methods have been developed and tested, based on deconvolution, iterative reconstruction, evolutionary algorithm and neural network.

The work is divided in three parts.

Chapter 2 provides an overview over the properties of X-rays, their generation and their interactions with matter. The BAM*line*, where all experiments reported in this work has been performed, is introduced, and the used spectroscopic methods, namely X-ray absorption fine structure spectroscopy and X-ray fluorescence spectroscopy are described.

Chapter 3 is concerned with the setup for dispersive X-ray absorption fine structure spectroscopy. After a general overview over the possibilities of time-resolved X-ray fine structure spectroscopy, the characterization of the dispersive element in different preliminary experiments is presented. Afterwards, the experiments at the BAM*line*

with reference foils and the case study of the time-resolved investigation of a chemical reaction are described.

Chapter 4 deals with the new method for X-ray fluorescence imaging with coded aperture. First, the principle and theory of coded aperture imaging and the used reconstruction methods are shortly described. Next, simulations that were used to better understand the imaging system are presented. Finally, the experiments conducted at the BAM*line* and the results are reported.

Chapter 5 sums up the work presented in the thesis and provides a conclusion and outlook.

2 X-ray spectroscopy

X-rays have been discovered in 1895 by W. C. Röntgen. Since then they have attracted a growing and unbroken interest. Their characteristic properties make them a valuable tool for many applications. Nowadays they are a indispensable instrument both in all day life, including medical and safety applications, and in research. X-rays are a part of the electromagnetic spectrum between ultraviolet radiation and gamma radiation and have wavelengths from approximately $12.4\,\text{nm}$ to $12.4\,\text{pm}$ corresponding to frequencies from approximately $24.2 \times 10^{15}\,\text{Hz}$ to $24.2 \times 10^{18}\,\text{Hz}$ and energies of approximately $100\,\text{eV}$ to $100\,\text{keV}$(see Figure 2.1). According to the wave-particle-dualism, X-rays can be regarded as particles or as wave packets to which an energy and a frequency or wavelength can be assigned. X-rays are invisible and propagate with the velocity of light. Their energy is high enough to ionize gases and to liberate electrons from atoms. They are absorbed by materials depending on the composition, density and thickness. These properties are the basis for X-ray spectroscopic methods. As for every electromagnetic wave, the energy of X-rays is proportional to their frequency:

$$E = h\nu \tag{2.1}$$

h is the Planck's constant and ν is the frequency of the electromagnetic wave. With $\nu = c/\lambda$, where c is the velocity of light and λ the wavelength, it follows that the energy is inversely proportional to the wavelength of the wave:

$$E = \frac{hc}{\lambda} \tag{2.2}$$
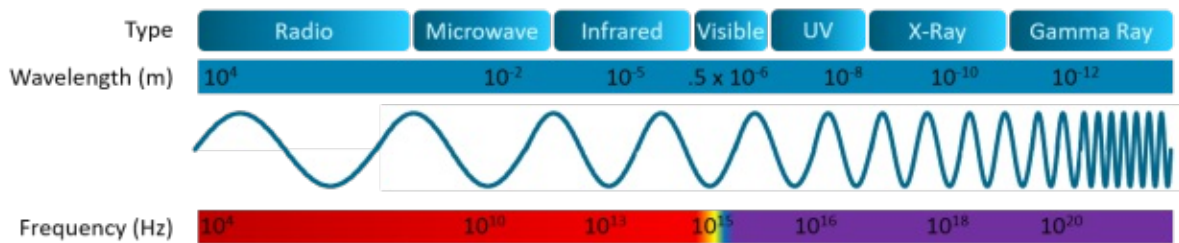
Figure 2.1: A rough overview of the electromagnetic spectrum

Putting in the values for h and c, the energy in electronvolt is approximately

$$E[\text{eV}] = \frac{1239.8}{\lambda[\text{nm}]}. \tag{2.3}$$

In the following, the most important interactions of X-rays with matter will be shortly explained in section 2.1, an overview of the generation of X-rays will be given in section 2.2, and then the principles of X-ray fluorescence (XRF) spectroscopy and X-ray absorption fine structure (XAFS) spectroscopy will be presented in section 2.4.

2.1 X-ray interactions with matter

Different interactions of X-rays with matter are possible, *e.g.*, elastic scattering (Thomson or Rayleigh), inelastic scattering (Compton), photoelectric absorption, photonuclear absorption, and, for energies above 1.022 MeV, electron positron pair production. For the indication of the probability for a certain interaction of a photon with matter, the quantity cross section can be used. The cross section has the unit of an area; for particle physics, the conventional unit of the cross section is the barn, b, with $1\,\text{b} = 10^{-24}\,\text{cm}^2$. Often, the cross section is given in barns/atom or $\text{cm}^2\,\text{g}^{-1}$. The cross sections for the different interactions depend on the material, and the energy of the incoming photon, but qualitatively the absorption cross section spectra are similar. As an example, the cross sections for Copper are shown as an example in Figure 2.2.

2.1.1 Photoelectric effect

For X-rays up to 100 keV, the photoelectric effect is the most important interaction of the photons with matter. In the photoelectric effect, a photon is absorbed by an atom, and an electron, the so called photo electron, is released.

X-ray photons have an energy in the same order of magnitude as the binding energies of inner shell (K, L, M) electrons in atoms, so they can interact with these electrons. If the energy of the incoming photon is equal to or higher than the binding energy of the electron, it can deliberate a core electron. The photon transfers all of its energy to the electron, so the kinetic energy of the outgoing photo electron is equal to the photon energy reduced by the binding energy.

$$E_{photoelectron} = E_{photon} - E_{binding} \tag{2.4}$$

As a result of the ejection of the photo electron, a vacancy in the core shell is created, also called core hole, and the atom is in an energetically unfavorable state. The core
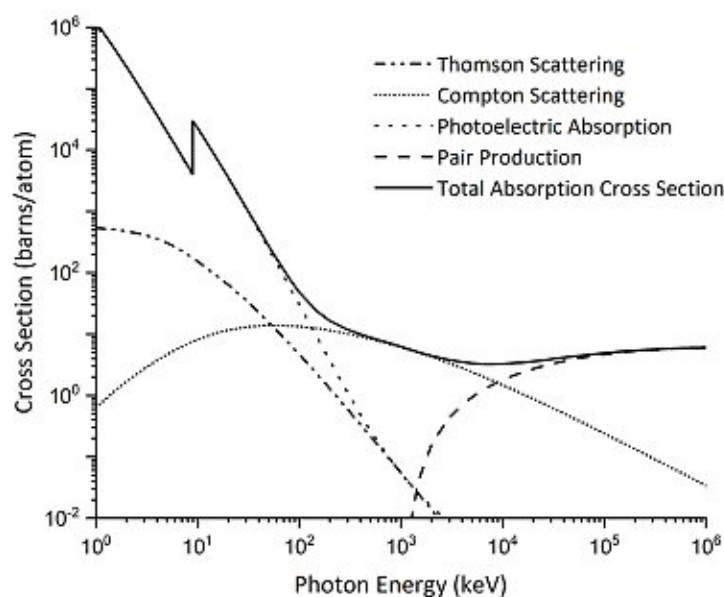
Figure 2.2: Cross section of the different interactions of X-rays with matter for copper as a function of energy. In the X-ray region up to 100 keV the photoelectric absorption is the dominant process. Data from the NIST XCOM: Photon Cross Sections Database[1].

hole will be filled by an electron from an outer shell. This can produce a fluorescence photon with an energy that is equal to the energy difference between the energy of the core hole shell and the shell from which the electron filling the core hole originates. As the energy levels are different for every element, every element has another characteristic fluorescence radiation.

Another relaxation pathway is the production of an Auger electron. This happens when the energy released by the electron filling the core hole is transmitted to another electron from the same atom that is then emitted. A scheme of the photo effect and the possible following processes is shown in Figure 2.3.

The probability for the Auger process to occur is higher for light elements than that for a fluorescent decay. This is shown for the example of K-shell vacancies in Figure 2.4.

2.1.2 Scattering

Another important effect, that can not be neglected in X-ray spectroscopy, is scattering. A photon entering into matter can be scattered. The scattering can be either elastic (Rayleigh and Thomson scattering), that means that the energy of the photon is the same before and after the scattering process, or inelastic (Compton scattering), when
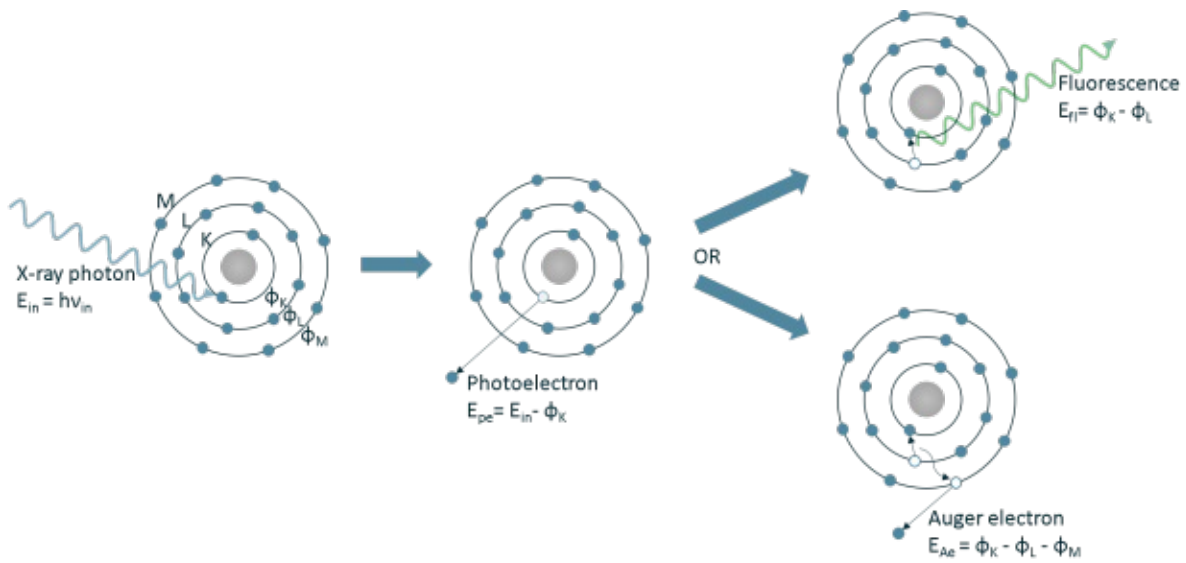
Figure 2.3: Photoeffect: The vacancy that is produced by the ejection of an inner shell electron by an X-ray photon is filled by an electron from a higher shell. The released energy is either emitted as fluorescence radiation or can eject another electron, the so called Auger electron.
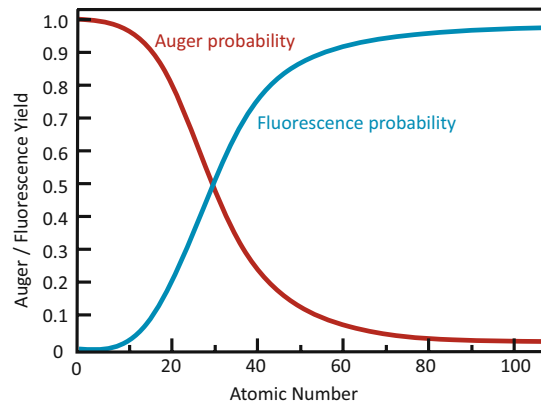
Figure 2.4: Comparison of the probability for Auger and fluorescence decay of an atom with a vacancy in the K-shell as a function of atomic number.

the photon loses some of its initial energy in the scattering process.

Thomson or Rayleigh scattering is the coherent scattering of a photon on free or, compared to the photon energy, weakly bound charged particles, *e.g.*, electrons. Thomson scattering is the scattering of photons on quasi-free electrons, and Rayleigh scattering describes the scattering of photons on weakly bound electrons, whole atoms or small molecules, *i.e.*, with a radius much smaller than the wavelength of the incoming light. The photon stimulates the particle to oscillate at the same frequency. This oscillating particle acts as dipole and emits radiation of the same frequency as the incoming photon, but with a changed direction.

Thomson scattering is sometimes referred to as the low energy limit of Compton scattering, if the incoming photon doesn't change the kinetic energy of the scattering particle.

In Compton scattering, a part of the energy of the incoming photon is transferred to the scattering electron of rest mass m_e that is recoiled. The outgoing, scattered photon has lower energy, *i.e.*, larger wavelength λ_{out}, than the incoming photon with wavelength λ_{in}, and the wavelength shift, also called Compton shift, depends on the scattering angle θ.

$$\lambda_{out} - \lambda_{in} = \frac{h}{m_e c} \cdot (1 - \cos\theta) \tag{2.5}$$

The scattering intensity is dependent on the direction of the observer relative to the polarization of the incoming X-ray. This is an important fact, because it allows to considerably reduce the scattering contribution in an X-ray experiment by placing the detector perpendicular to the polarization direction[2].

2.1.3 Attenuation of X-rays

All of the effects of interaction between X-rays and matter described in the previous sections lead to an attenuation of the intensity of X-rays passing through a material. This attenuation follows the law of Lambert-Beer:

$$I = I_0 e^{-\mu(E)x} \tag{2.6}$$

This equation describes the attenuation of an incoming X-ray beam of intensity I_0 that travels through an absorber of thickness x. After the absorber, the intensity has reduced to the value I. The linear attenuation coefficient, $\mu(E)$, depends on the energy of the incoming photons and the material. It is related to the absorption cross section $\sigma(E)$ through:

$$\mu(E) = \rho\sigma(E) \tag{2.7}$$

Here, ρ is the density of the absorber material in $\mathrm{g\,cm^{-3}}$, and σ is the total absorption cross section in $\mathrm{cm^2\,g^{-1}}$, *e.g.*, the sum of the cross sections for the Thomson and Compton scattering, the photoelectric absorption and the pair production.

$$\sigma_{tot} = \sigma_{Thomson} + \sigma_{Compton} + \sigma_{pe} + \sigma_{pair} \tag{2.8}$$

Another quantity, derived from the linear attenuation coefficient, is the mass attenuation coefficient, $\mu_m = \mu/\rho$. If the absorber is composed of a mixture of different materials, the attenuation coefficient must be calculated from the attenuation coefficients of all components:

$$\mu_m = \sum_i \mu_{m_i} \cdot c_i = \sum_i \frac{\mu_i}{\rho_i} \cdot c_i = \sum_i \frac{\rho_i \sigma_i}{\rho_i} \cdot c_i = \sum_i \sigma_i \cdot c_i \tag{2.9}$$

with c_i the atomic weight ratio of the ith component.

The attenuation coefficient depends on the material, as already seen, and on the energy. The functional dependence is approximately described in the Bragg-Pierce law:

$$\mu = C \cdot \frac{Z^a}{E^b}, \tag{2.10}$$

where $a \approx 3$ and $b \approx 4$.

Elements with higher atomic number Z absorb more than lighter elements. The energy dependence results in a smooth decrease in the attenuation coefficient with increasing energy. At some points, the so-called absorption edges, it raises abruptly. The X-ray absorption spectroscopy investigates these edges and their vicinity. As an example, the energy dependence of the mass attenuation coefficient for lead is shown in Figure 2.5.

The edges occur at energies that are high enough to deliberate an electron of an inner shell. They are named K-, L-, M-, ... edges, corresponding to the shells from which the electron is ejected. As the electrons in the K shell are most strongly bound, the energy of the K-edge is the highest. As can be seen in Figure 2.5, there are several L- and M-edges. This is due to the fact that the electrons in the higher shells are in different states, which are not energetically equivalent, when a transition occurs.

The energy of the absorption edges increases with increasing atomic number approx-
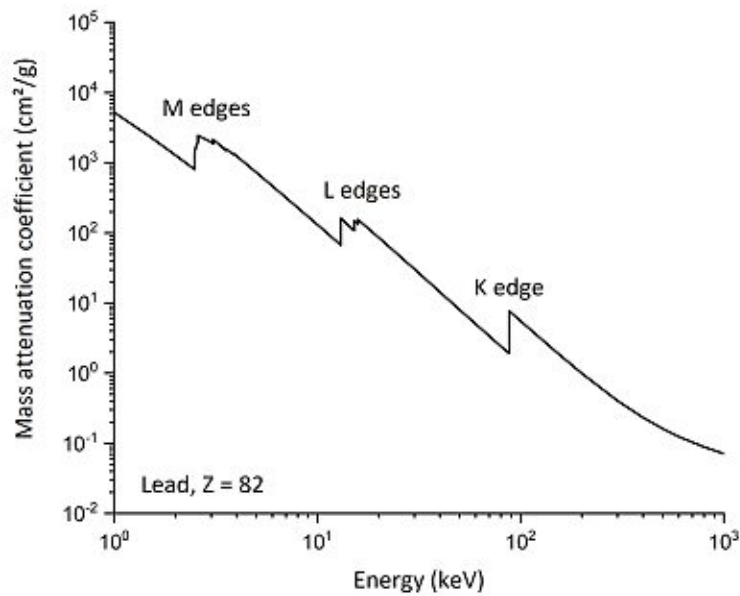
Figure 2.5: Mass attenuation coefficient for lead. The coefficient decreases with increasing energy. At some points, the absorption edges, the absorption changes abruptly. Data taken from the NIST X-ray attenuation coefficients data base[3].

imately according to Moseley's law.

$$E_{edge_Z} = k \cdot (Z - sc)^2 \tag{2.11}$$

where k is a constant and sc is a screening constant that takes different values for different shells.

2.2 Generation of X-rays

X-rays are produced in two different processes, by Bremsstrahlung and by transitions between electron shells in atoms or molecules. Different sources make use of these processes to generate X-rays:

- radioactive sources (transitions)

- X-ray tubes (transitions and Bremsstrahlung)

- free electron lasers (Bremsstrahlung)

- synchrotron radiation sources (Bremsstrahlung)

11
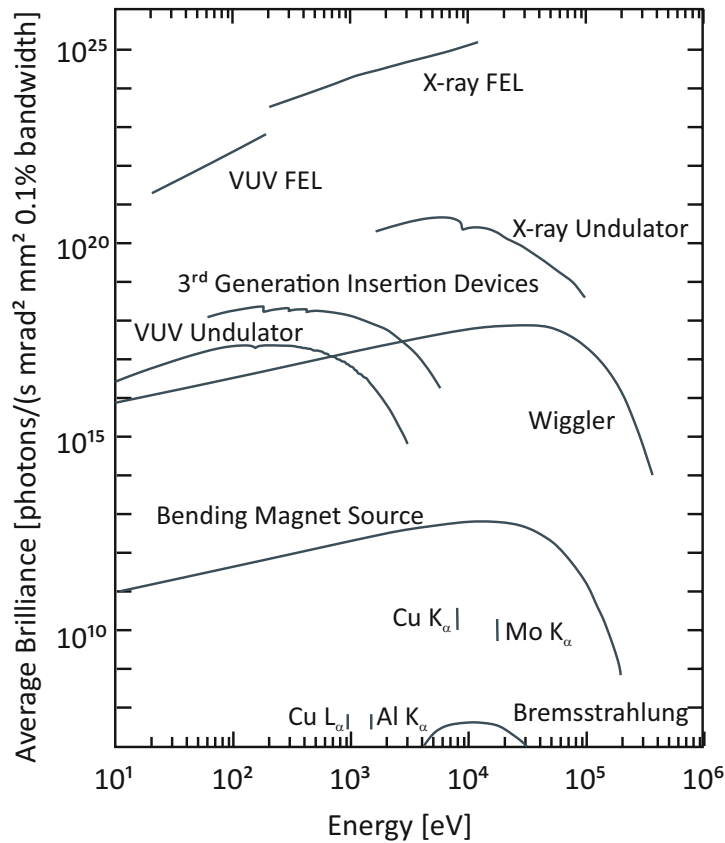
Figure 2.6: Comparison of the average brilliance of various X-ray sources depending on the energy. Illustration aadapted from[4].

Bremsstrahlung is produced, when a charged particle, *e.g.*, an electron, is accelerated, *e.g.*, by deflection of the trajectory by the Coulomb field of the nucleus of an atom when the electron penetrates matter, or by magnetic fields in a synchrotron.

The generated X-ray spectra have different spectral distributions and a different brilliance, *i.e.*, photons per second, emission angle and area of the beam, within an energy bandwidth of 0.1% . The average brilliance of different X-ray sources is sketched in Figure 2.6.

2.2.1 X-ray tubes

X-ray tubes are an established and widely used tool to produce X-rays. They are used for medical applications as well as for X-ray analytical methods. Contrary to synchrotron radiation, X-ray tubes are used in laboratory-based experiments, and are therefore indispensable for research.

An X-ray tube in its simplest form consists of a cathode, often a tungsten filament, and an anode, that are enclosed in an evacuated glass tube. The cathode is heated through
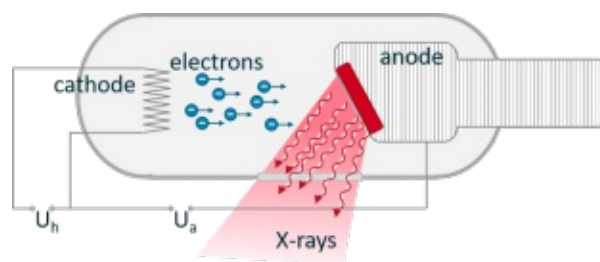
Figure 2.7: Simplified scheme of an X-ray tube. Cathode and anode are enclosed in an evacuated tube. The filament of the cathode is heated, and the ejected electrons are accelerated by the electrical field generated by a high voltage towards the anode. X-rays are produced, when these electrons hit the anode. For the dissipation of heat, the anode is cooled.

a current from a power supply and thermal electrons are emitted. These electrons are accelerated by a high voltage towards the anode, that usually consists of a very pure metal, for example molybdenum, copper or tungsten. When they hit the anode, Bremsstrahlung and characteristic radiation is emitted. Therefore, the spectrum of an X-ray tube consists of a continuous part (Bremsstrahlung) with a maximum that equals the maximum kinetic energy of the electrons that hit the anode, and the characteristic lines of the anode material. Figure 2.7 shows the scheme of an X-Ray tube.

The spectrum depends on the anode material, the acceleration voltage, and the take-off angle under which the X-rays leave the tube. Usually, the generated X-rays leave the tube through a Beryllium window. The conversion rate from electrical power to X-rays is only very low ($\approx 1\%$), the rest is converted into heat. As the heat load at the anode is very high, it has to be cooled. Cooling is possible with water or oil, or a rotating anode is used, where the heat of the focal spot, where the electrons hit the anode, is dispersed over a larger area, so that the lifetime of the anode can be prolonged. Another approach to address the issue of thermal damage in the anode and to enhance the power and brightness of X-ray sources is the liquid-metal-jet anode. In this technique, a liquid metal jet acts as anode, that is continuously regenerated.

The physics and characteristics of X-ray tubes, their spectra and how these spectra depend on different parameters, could be discussed in much more detail. However, as the only radiation source used in the course of this work is synchrotron radiation, further characteristics of X-ray tubes can be found elsewhere, for example in handbooks on X-ray spectroscopy and spectrometry such as [5,6].

2.2.2 Synchrotron radiation

As can be seen in Figure 2.6, synchrotron radiation from third generation light sources has a high brilliance and a broad spectrum. Furthermore, it is tunable, polarized ra-

diation can be used, both circular and linear, and small beam sizes and high intensity are possible. The accessible energy ranges from the infrared to the X-ray region. These advantageous properties make them a useful tool for many applications.

In this chapter, the term synchrotron refers always to an electron synchrotron, although there are also synchrotrons that are operated with positrons, protons or even heavier ions.

Introduction

Synchrotron radiation was predicted in 1944 by Iwanenko and Pomeranchuk[7] as a limiting factor for the attainable energy in a betatron, a magnetic-induction electron accelerator. It was first observed in 1947 at General Electrics (GE)[8] at a 70 MeV synchrotron. In the first time, synchrotron radiation was seen as an undesirable effect in particle accelerators as it was responsible for the energy loss of the accelerated particles. But the interest in this type of radiation grew quickly, and sources dedicated to the generation of synchrotron radiation were planned and constructed since the 1970's. The first experiments on a so-called second generation synchrotron source were conducted in 1981 at the Synchrotron Radiation Source (SRS) at Daresbury, and others followed quickly. Since the 1990's, third-generation synchrotron light sources are built, that are optimized for insertion devices such as undulators. Nowadays, the first fourth-generation synchrotrons are in operation, as MAX-IV in Sweden[9], or will start their operation in the near future, as SIRIUS in Brazil[10] and EBS, the upgrade of the ESRF in France[11]. These fourth-generation synchrotrons are characterized by a low emittance and high coherence of the X-rays produced. This is achieved by an innovative design of the magnetic lattice, the so-called multi-bend achromat lattices. Today, all in all around 50 synchrotron facilities in operation all over the world. More information about the early history of synchrotron radiation can be found for example in[12]. In the following only a brief summary on the theory of the synchrotron radiation is given, inspired the dissertation chapters of Buzanich[13] and Meirer[14]. More detailed information can be found in the original work from J.A. Schwinger[15] and in several books on the topic, for example [16–18].

Operation of a storage ring

In an electron synchrotron, an electron source creates electrons. These are accelerated, often first by a linear accelerator (LINAC) and then further with a synchrotron. When they reach near speed of light, they are injected in the storage ring. In a third-generation synchrotron light source, this storage ring consists of a magnetic structure that holds the electrons on a closed orbit, and several straight sections with insertion devices, such as bending magnets, undulators, wigglers, or wavelength shifters. The insertion de-

vices produce the synchrotron radiation, that reaches the experimental stations through beamlines.

A simple scheme of a synchrotron facility with electron source, accelerator, booster synchrotron and storage ring is shown in Figure 2.8.
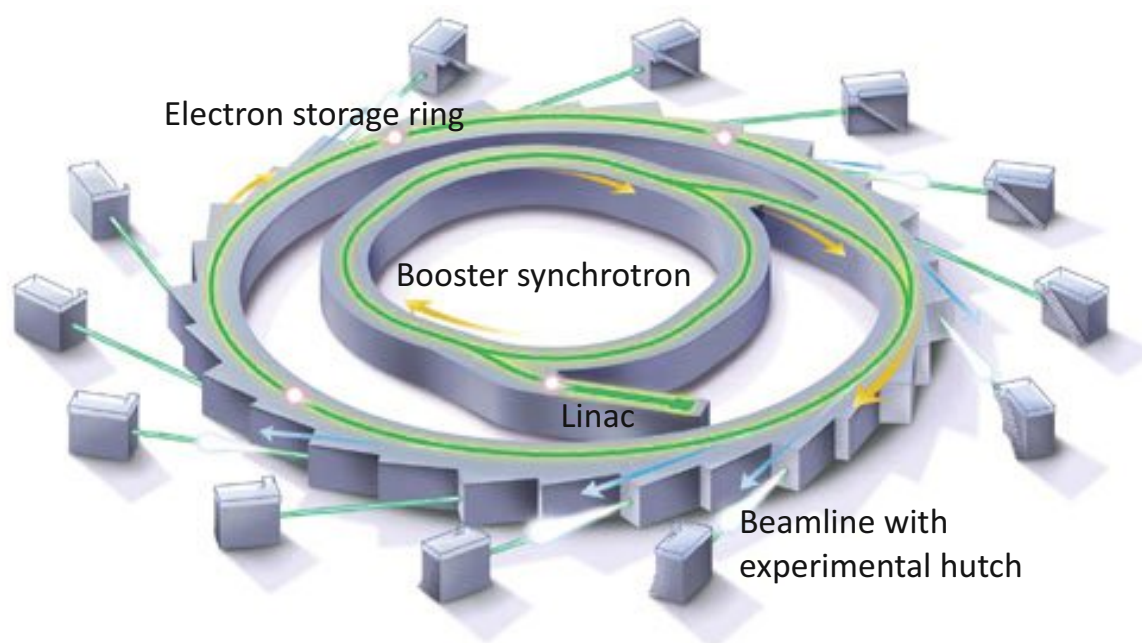
Figure 2.8: Scheme of a synchrotron, taken from[19]

The electron source can be an electron gun that works after the same principle as a cathode ray tube.

In the LINAC, the electrons are accelerated by means of a high frequency accelerating voltage. The principle can be explained by considering a simple drift tube LINAC, a so-called Wideroe accelerator, named after Rolf Wideroe, who implemented such an accelerator for the first time in 1927 after an idea of Ising, dating from 1924. Several drift tubes are placed in a line and a high frequency (radio frequency, RF) voltage is applied that leads to an acceleration of an electron in the gap between two drift tubes. The principle of the setup is shown in Figure 2.9. The energy gained by the electron depends on the voltage and the phase:

$$dE = qU_{eff} = qU_{max} \cdot \cos(\omega_{RF}t) \tag{2.12}$$

with U_{max} being the maximum value of the acceleration voltage and ω_{RF} the frequency of the acceleration voltage. If the electron sees always the same acceleration voltage, *i.e.*, if it traverses every drift tube in the time of half a period $T = 2\pi/\omega_{RF}$ of the acceleration voltage, the energy gain per section of the LINAC is constant. For electrons that are
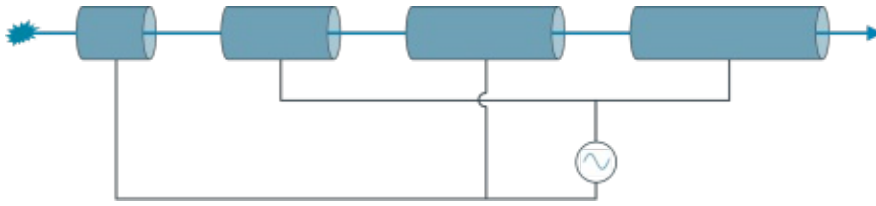
Figure 2.9: The principle of a Wideroe drift tube linear accelerator. The electrons passing through the acceleration path see an acceleration voltage in the gap between two drifttubes.

not relativistic, the gain in energy equals a gain in velocity, hence the drift tubes need to increase in length the long of the acceleration path. A reference electron, that fulfills this synchroism condition enters in a gap always with a phase ϕ_r, for example on the positive slope of the acceleration voltage, as depicted in Figure 2.10. If there is more than
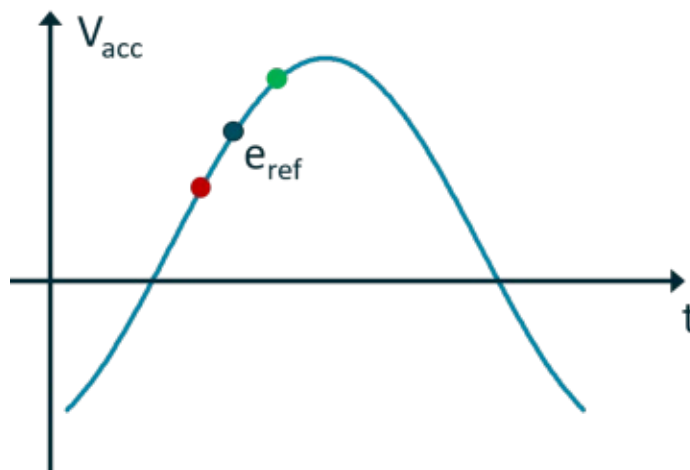
Figure 2.10: The appropriate choice of the reference phase on the positive slope of the high voltage makes sure, that slower electrons (green), that arrive later than the reference electron (deep blue) in the gap ($t > t_{ref}$), see a higher acceleration voltage and gain more energy than the reference electron in this section of the accelerator, so that the delay will be (partially) compensated in the next gap. Inversely, a faster electron (red) will see a lower voltage, and hence will gain less energy and velocity until the next gap, thus reducing the distance to the reference electron. This is the principle of phase stability.

one electron, they will have some velocity distribution and will not arrive at the same time at the gap. An electron with higher energy than the reference electron, arriving slightly before the reference electron in the gap, sees a lower acceleration voltage (see Figure 2.10). It will gain less energy and velocity until the next gap compared to the reference electron. In consequence, the distance to the reference electron will reduce. In contrary, an electron with lower energy and velocity, that arrives slightly after the

reference electron in the gap, will experience a higher voltage and gain more energy and velocity, thus taking less time to arrive at the next gap, and coming nearer to the reference electron. In consequence, if the reference phase is suitably chosen, this provides a focusing in the direction of the acceleration (longitudinal) of the electron beam, known as phase stability principle.

The Wideroe LINAC is a simple accelerator. For acceleration to higher electron energies, other accelerator structures are used, such as single or multiple cavities. Here, electromagnetic fields with an electric field component in the direction of propagation of the beam transfer energy to the electrons. They are operated at a frequency that matches the resonance frequency of the structure itself. However, the principle of phase stability remains the same. Hence, what is injected into the synchrotron after the first acceleration step is not a continuous beam, but packets of electrons, called bunches.

Single or multiple cavities are suitable not only for linear acceleration, but also for circular acceleration, where the beam passes more than one time by the accelerating structure. This is the case in booster synchrotrons, where the electrons are accelerated further, before they are injected to the storage ring. In the storage ring, RF-cavities are necessary to restore the energy that the electrons lose by radiation in every revolution.

For electrons with $\beta = \frac{v}{c} \approx 1$, that means traveling with nearly the speed of light, as is normally the case in synchrotrons, the increase in energy does not lead to an increase in velocity, but to an increase in momentum. The principle of phase focusing in the longitudinal direction in this case can be reached when an electron, that arrives earlier than a reference electron in the accelerating structure, gains more energy. This means a higher increase in momentum, leading to a larger radius inside the ring, because particles with a higher momentum are deflected less in the magnetic structure. As all electrons move with nearly the velocity of light, a larger radius means a longer time to travel around the whole ring, and in the next turn, the initial advanced electron will be nearer to the reference electron. The contrary effect is true for electrons arriving later than the reference electron. Thus, the (longitudinal) phase stability can also be assured in the synchrotron and later on in the storage ring. The storage ring is then filled with a number of electron bunches, that can be adjusted according to the needs of the user. For example, the fill pattern can be used for time-resolved measurements, as the circulation period can be calculated exactly and leads to well defined flashes of sychrotron light with a known duration and a known frequency.

To force the electrons on a circular path as required in synchrotrons and storage rings, magnets are used. The force exerted on the moving electrons is the Lorentz force:

$$F_L = q \cdot \left(\vec{E} + \vec{v} \times \vec{B} \right) \tag{2.13}$$

with q the charge of the particle, $\vec{E}$ the electrical field, $\vec{v}$ the velocity of the particle, and $\vec{B}$ the magnetic field. An electron that moves through a magnetic field, experiences a force that is perpendicular to both, the direction of motion and the magnetic field. The force of the magnetic field needed to keep electrons on a circular path of a given radius (for example the radius of the storage ring) and for a given electron energy can be calculated, because the Lorentz force has to be equal the centripetal force. Here, only the magnetic field component of the Lorentz force is considered:

$$\frac{mv^2}{R} = q \cdot \left(\vec{v} \times \vec{B}\right)$$

(2.14)

relativistic particle: $m = \gamma m_0$ with $\gamma = \frac{1}{\sqrt{1-\beta^2}}$ and $q \cdot \left(\vec{v} \times \vec{B}\right) = qvB$

$$\Leftrightarrow \frac{\gamma m_0 v^2}{R} = qvB$$
$$\Leftrightarrow \frac{\gamma m_0 \cdot v}{R} = qB$$
$$\Leftrightarrow \frac{p}{R} = qB$$
$$\Leftrightarrow B = \frac{pq}{R}$$

(2.15)

Not all particles have the same orbit and the same momentum. So, there is a natural divergence in the electron beam. To avoid beam losses in the directions perpendicular to its motion, transverse focusing is necessary. Therefore, quadrupol magnets are used. These magnets focus the beam in one plane while defocusing it in the other plane. Alternating orientated quadrupol magnets assure an overall focusing. Furthermore, sextupol and sometimes even higher order magnets are inserted in the ring to guarantee the beam stability. As a result, a stable, well defined electron beam with a high lifetime is achieved.

From this exactly known electron beam in the storage ring, the properties of the synchrotron radiation are completely calculable and quantitatively known. This fact makes them an indispensable tool for example for calibration applications.

Properties of synchrotron radiation

The basis for synchrotron radiation is the generation of electromagnetic fields by moving charged particles. The potentials created by a moving charged are the so-called Liénard-

Wiechert potentials.

$$\Phi\left(\vec{x}, t\right) = \left[\frac{q}{\left(1 - \vec{n}\vec{\beta}\right) \cdot R}\right]_{ret} \tag{2.16a}$$

$$A\left(\vec{x}, t\right) = \left[\frac{q \cdot \vec{\beta}}{\left(1 - \vec{n}\vec{\beta}\right) \cdot R}\right]_{ret} \tag{2.16b}$$

q is the charge of the moving particle, $\vec{\beta}$ is its velocity divided by the velocity of light, $\vec{\beta} = \frac{\vec{v}}{c}$, R is the distance between the point where the potential is observed at time t, and the point, where the moving charge as origin of the potential has been at time $t_{ret} = t - R(t_{ret})/c$, and $\vec{n}$ is the unit vector pointing in the direction between moving charged particle and point of observation. The fields created by these potentials can be calculated according to

$$\vec{E}\left(\vec{x}, t\right) = -\frac{1}{c} \cdot \frac{\partial \vec{A}}{\partial t} - \vec{\nabla}\Phi$$

$$= q \cdot \left[\frac{\left(\vec{n} - \vec{\beta}\right) \cdot (1 - \beta^2)}{\left(1 - \vec{\beta}\vec{n}\right)^3 \cdot R^2}\right]_{ret} + q \cdot \left[\frac{\vec{n} \times \left(\left(\vec{n} - \vec{\beta}\right) \times \dot{\vec{\beta}}\right)}{c \cdot \left(1 - \vec{\beta}\vec{n}\right)^3 \cdot R}\right]_{ret} \tag{2.17a}$$

$$\vec{B}\left(\vec{x}, t\right) = \vec{\nabla} \times \vec{A}$$

$$= \left[\vec{n} \times \vec{E}\right]_{ret} \tag{2.17b}$$

Here, we can see that in the case of a particle in rest, the Liénard-Wiechert equation for the electrical field reduces to the Coulomb field of the charge. Furthermore, the formula indicates two parts of the electrical field. The so-called velocity field, that depends on $\vec{\beta}$, falls off with R^{-2} (left part), and the so called acceleration field, that depends on $\dot{\vec{\beta}}$, falls off with R^{-1}. So, the acceleration field dominates over the velocity field at large distances from the source.

Non-relativistic particle

If the velocity of the charged particle is small compared to the speed of light, $\beta \to 0$, and the acceleration field can be written as

$$E_{acc} = q \cdot \left[\frac{\vec{n} \times \left(\vec{n} \times \dot{\vec{\beta}}\right)}{cR}\right] \tag{2.18}$$

The Poynting vector describes the instantaneous flux of energy:

$$\vec{S} = \frac{c}{4\pi} \cdot \vec{E} \times \vec{B}$$
$$= \frac{c}{4\pi} \cdot \left|\vec{E}\right|^2 \cdot \vec{n} \tag{2.19}$$

From

$$t_{ret} = t - \frac{R(t_{ret}) \cdot \vec{n}}{c}$$

it follows that

$$\frac{dt}{dt_{ret}} = 1 + \frac{d(R(t_{ret}) \cdot \vec{n})}{dt_{ret}} \cdot \frac{1}{c} = 1 - \vec{\beta}\vec{n}$$
$$\left(\text{because } \frac{d(R(t_{ret}) \cdot \vec{n})}{dt_{ret}} = -\vec{v}\vec{n}\right)$$

and $1 - \vec{\beta}\vec{n} \approx 1$ for very small β. With this, the power per unit solid angle in a time interval is then

$$\frac{d^2 P}{d\Omega} = \left[\vec{S}\vec{n}\right] \cdot R^2 \cdot \frac{dt}{dt_{ret}}$$
$$= \frac{c}{4\pi} \cdot R^2 \cdot \left|\vec{E}\right|^2$$
$$= \frac{q^2}{4\pi c} \cdot \left|\vec{n} \times \left(\vec{n} \times \dot{\vec{\beta}}\right)\right|^2 \tag{2.20}$$

With the angle θ between the direction of acceleration and the vector $\vec{n}$ this expression leads to

$$\frac{d^2 P}{d\Omega} = \frac{q^2}{4\pi c} \cdot \left|\dot{\vec{v}}\right|^2 \cdot sin^2\theta \tag{2.21}$$

Integration over the solid angle yields the Larmor formula for a nonrelativistic accelerated charge.

$$P = \frac{2}{3} \cdot \frac{q^2}{c^3} \cdot \left|\dot{\vec{v}}\right|^2 \tag{2.22}$$

From equation 2.18 it can be deduced, that the radiation is polarized in the plane that contains the acceleration $\dot{\vec{\beta}}$ and the direction of observation $\vec{n}$.

Relativistic particle

If the charged particle moves with a velocity near the speed of light, instead of equation 2.18, the acceleration field is

$$E_{acc} = \frac{q}{c} \cdot \left[\frac{\vec{n} \times \left(\left(\vec{n} - \vec{\beta} \right) \times \dot{\vec{\beta}} \right)}{\left(1 - \vec{\beta}\vec{n} \right)^3 \cdot R} \right] \tag{2.23}$$

With this, the radiated power per solid angle in a time interval is, equivalent to equation 2.20,

$$\begin{aligned}
\frac{d^2 P}{d\Omega} &= \left[\vec{S}\vec{n} \right] \cdot R^2 \cdot \frac{dt}{dt_{ret}} \\
&= \frac{c}{4\pi} \cdot R^2 \cdot \left| \vec{E} \right|^2 \cdot \left(1 - \vec{\beta}\vec{n} \right) \\
&= \frac{c}{4\pi} \cdot R^2 \cdot \frac{q^2}{c^2} \cdot \left| \frac{\vec{n} \left(\left(\vec{n} - \vec{\beta} \right) \times \dot{\vec{\beta}} \right)}{R \cdot \left(1 - \vec{\beta}\vec{n} \right)^3} \right|^2 \cdot \left(1 - \vec{\beta}\vec{n} \right) \\
&= \frac{q^2}{4\pi c} \cdot \frac{\left| \vec{n} \left(\left(\vec{n} - \vec{\beta} \right) \times \dot{\vec{\beta}} \right) \right|^2}{\left| 1 - \vec{\beta}\vec{n} \right|^5}
\end{aligned} \tag{2.24}$$

In this formular, the dominating term is the denominator $\left| 1 - \vec{\beta}\vec{n} \right|^5$. For a charged particle on a circular orbit, it is useful to introduce a coordinate system with the charge in the origin and coordinate axes defined so that the direction of motion of the particle is in the x-direction and the acceleration in the z-direction, as depicted in Figure 2.12. The scalar product can then be written as $\vec{\beta} \cdot \vec{n} = |\vec{\beta}| \cdot |\vec{n}| \cdot cos\phi$. This indicates that for a particle moving with a velocity near the speed of light, the emitted radiation is collimated forward, as the fifth power of the cosine decreases rapidly for large angles. A sketch of the emission pattern for a moving electron is shown in Figure 2.11. For a charged particle moving on a circular orbit, the radiation is emitted tangential to the orbit in the orbital plane.

The Larmor formula can also be extended by the Lorentz transformation to relativistic particles, or by integration of equation 2.24 over 4π, resulting in a formula for the total radiated power:

$$P = \frac{2}{3} \cdot \frac{q^2}{c} \cdot \gamma^6 \left[\left(\dot{\vec{\beta}} \right)^2 - \left(\vec{\beta} \times \dot{\vec{\beta}} \right)^2 \right]. \tag{2.25}$$
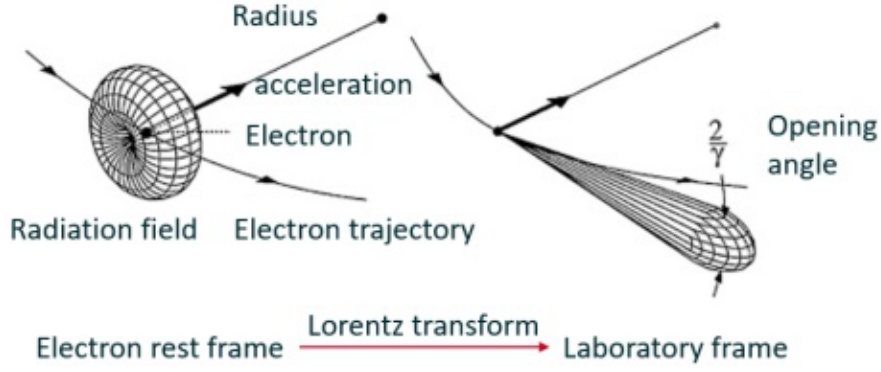
Figure 2.11: Emission pattern of a moving electron in its rest frame (left) and in the laboratory frame (right). The radiation is strongly collimated to the direction of the velocity. The opening angle can be directly calculated from the Lorentz factor. Adapted from [20].

For a particle that moves on a circle of radius ρ, $\vec{\beta}$ is perpendicular to $\dot{\vec{\beta}}$ and $\left(\vec{\beta} \times \dot{\vec{\beta}}\right)^2$ reduces to $\dot{\beta}^2 \cdot (1 - \beta^2) = \dot{\beta}^2/\gamma^2$. As the acceleration is centripetal, $\dot{\beta} = c \cdot \beta^2/\rho$, and with $\gamma = E/(m_0 c^2)$, equation 2.25 becomes

$$
\begin{aligned}
P &= \frac{2}{3} \cdot \frac{q^2 \gamma^4 c \beta^4}{\rho^2} \\
&= \frac{2}{3} \cdot \frac{q^2 c}{\rho^2} \cdot \left(\frac{E}{m_0 c^2}\right)^4 \cdot \beta^4
\end{aligned}
\tag{2.26}
$$

The radiation power emitted per cycle in a synchrotron is P multiplied with the time that the particle needs to move one time around the whole circle, $2\pi \cdot \rho/\beta c$:

$$
\Delta E = \frac{4\pi q^2 \beta^3}{3\rho} \cdot \left(\frac{E}{m_0 c^2}\right)^4
\tag{2.27}
$$

This shows that the radiated power is proportional to the fourth power of the energy. One consequence of this relation is, that the energy of particles in storage rings cannot be increased arbitrarily, because the energy loss grows too fast. The radiated power is the power that the electrons (or other particles) lose in the storage ring and that, therefore, must be resubstituted by the radio frequency system. As the radiated power depends on m_0^{-4}, higher radiation power at the same particle energy can be obtained for lighter particles. For example, comparing the the radiated power of protons and electrons, with

$$
m_e = 0.511 \, \text{MeV} \quad \text{and} \quad m_p = 938.3 \, \text{MeV}
\tag{2.28}
$$
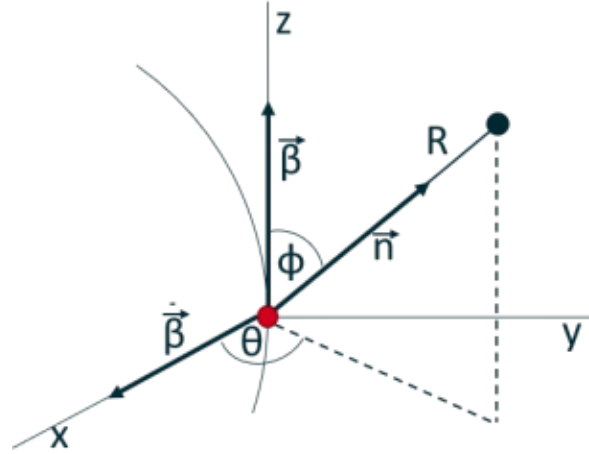
Figure 2.12: Coordinate system with a charge, moving on a circular orbit, in the origin. The observer is in a point at distance R in direction $\vec{n}$ from the moving charge. The moving direction is the tangent on the circle, the acceleration is purely centripetal and directed towards the center of the circle.

the quotient of the energy losses has a value of

$$\frac{P_e}{P_p} = 1.14 \cdot 10^{13}. \tag{2.29}$$

This shows that electrons are better suited for the production of synchrotron radiation than protons or even heavier particles.

Time structure

Let's consider an electron synchrotron. As shown in Figure 2.11, the radiation of a moving charged electron is collimated strongly in the forward direction, that is tangential to the trajectory of the electron. Therefore, an observer in a point P sees only a short flash of light. For an electron following a circular orbit, these are photons emitted at all the points for which the direction of observation lies inside the cone with opening angle $2 \cdot \theta = 2/\gamma$. The duration of the pulse can be calculated. With t_0 the time of emission of the photons in point A (see Figure 2.13), the first photons will arrive at the position P in a distance R at $t_A = R/c$. The distance, that the electron travels between point A and B is $2\theta\rho$, and the time it takes for this path is $t_{AB} = 2\theta\rho/(\beta c)$. Photons emitted at point B have a distance of $R - 2\rho \cdot sin(\theta)$ to the point P, so they will arrive at the observer at time $t_B = t_{AB} + (R - 2\rho \cdot sin(\theta))/c$. Hence, the duration of the pulse seen
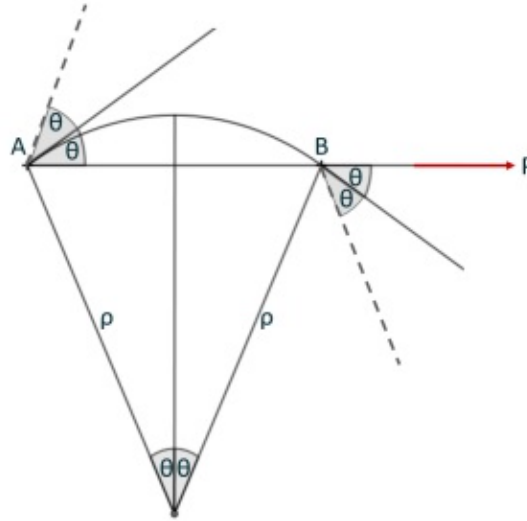
Figure 2.13: Calculation of the time structure of the photon pulse seen by the observer

by the observer is

$$
\begin{aligned}
\tau_{pulse} &= t_B - t_A \\
&= \frac{2\theta\rho - 2\rho sin(\theta)\beta}{\beta c}
\end{aligned}
\tag{2.30}
$$

With $sin(\theta) \approx \theta + \theta^3/3!$ for small θ and $\theta = 1/\gamma$, this becomes

$$
\begin{aligned}
\tau_{pulse} &= \frac{2\rho}{c} \cdot \left(\frac{1}{\gamma\beta} - \frac{1}{\gamma} + \frac{1}{6\gamma^3} \right) \\
&= \frac{4\rho}{3c\gamma^3} \text{ because} \frac{1}{\gamma\beta} = \frac{1}{\gamma \cdot \sqrt{1 - \frac{1}{y^2}}} \approx \frac{1}{\gamma} + \frac{1}{2\gamma^3} \text{ for } \gamma \to \infty
\end{aligned}
\tag{2.31}
$$

From here, the typical frequency can be directly derived as

$$
\omega_{typ} = \frac{2\pi}{\tau_{pulse}} = \frac{3\pi c\gamma^3}{2\rho}.
\tag{2.32}
$$

The critical frequency, that is defined as the frequency that divides the spectrum into two parts of equal integrated radiation power, is defined as

$$
\omega_c = \frac{\omega_{typ}}{\pi} = \frac{2\pi}{\tau_{pulse}} = \frac{3c\gamma^3}{2\rho} = \frac{3}{2} \cdot \gamma^3\omega_0
\tag{2.33}
$$

with the angular frequency from the rotation of the electron $\omega_0 = c/\rho$.

Usually, in a synchrotron facility the storage ring is filled with more than one electron.

The electrons travel in bunches, as described above, and hence the duration of the pulse as calculated in equation 2.30 is the time between the arrival of the photons emitted from the first electron in a bunch passing point A and the arrival of the photons emitted from the last electron in the same bunch passing point B. The width of the electron bunches plays an important role for the time structure of the synchrotron radiation.

Frequency distribution

The frequency distribution of synchrotron radiation can be exactly calculated, if the motion of the electron, *i.e.*, it's velocity and acceleration, and the direction of the observer are known. These calculations were first performed by Schwinger[15], and can be found in text books. Even for simple cases, such as the movement on a circle arc as in a bending magnet, they are generally quite lengthy.

The starting point is the radiation integral that describes the energy at the observers position per unit solid angle at the source.

$$\frac{d^2W}{d\Omega} = \int_{-\infty}^{\infty} \frac{d^2P}{d\Omega} dt \tag{2.34}$$

with $d^2P/d\Omega$ defined for a relativistic particle as in equation 2.24. A Fourier transform is used to move to the frequency space and the angular and frequency distribution of the radiation arriving at the observer (assuming that the source of radiation is far away and the velocity field can be neglected), becomes

$$\frac{d^3W}{d\Omega d\omega} = \frac{q^2}{4\pi^2 c} \cdot \left| \int_{-\infty}^{\infty} \frac{\vec{n} \times \left(\left(\vec{n} - \vec{\beta} \right) \times \dot{\vec{\beta}} \right)}{\left(1 - \vec{n}\vec{\beta} \right)^2} \cdot e^{i\omega(t - \vec{n}\vec{r}(t)/c)} dt \right|^2 . \tag{2.35}$$

For a bending magnet with the electron moving on an arc of a circle, with K_n a modified Bessel function of the second kind of order n, and $\xi = \frac{\rho\omega}{3c\gamma^3} \cdot (1 + \gamma^2\theta^2)^{3/2}$, this yields

$$\frac{d^3W}{d\Omega d\omega} = \frac{3q^2}{4\pi^2 c} \cdot \left(\frac{2\omega\rho}{3c\gamma^2} \right)^2 \cdot \left(1 + \gamma^2\theta^2 \right)^2 \cdot \left[K_{2/3}^2 (\xi) + \frac{\gamma^2\theta^2}{1 + \gamma^2\theta^2} \cdot K_{1/3}^2 (\xi) \right] \tag{2.36}$$

The modified Bessel function $K_{2/3}$ is associated to the radiation that is horizontally polarized, *i.e.*, in the orbital plane, whereas $K_{1/3}$ describes the radiation with a vertical polarization vector. For $\xi \gg 1$ the radiated power goes to zero. The frequency at which

$\xi = 1/2$ and $\theta = 0$ is defined as the critical frequency, ω_c:

$$\xi(\omega_c) = \frac{1}{2} = \frac{\rho\omega_c}{3c\gamma^3}$$

$$\Leftrightarrow \omega_c = \frac{3}{2} \cdot \frac{c\gamma^3}{\rho}. \tag{2.37}$$

The critical angle θ_c is defined as the angle

$$\theta_c \simeq \frac{1}{\gamma} \cdot \left(\frac{\omega}{2\omega_c}\right)^{-1/3} \tag{2.38}$$

For frequencies and angles much higher then the critical frequency and the critical angle the synchrotron radiation emission is negligible.

The frequency distribution can be calculated by integrating equation 2.36 over all angles:

$$\frac{dW}{d\omega} = \frac{\sqrt{3} \cdot q^2}{c} \cdot \gamma \cdot \frac{\omega}{\omega_c} \cdot \int_{\omega/\omega_c}^{\infty} K_{5/3}(x)dx \tag{2.39}$$

With the substitution

$$S(\omega/\omega_c) = \frac{9\sqrt{3} \cdot \epsilon_0}{2} \cdot \frac{\omega}{\omega_c} \cdot \int_{w/w_c}^{\infty} K_{5/3}(x)dx \tag{2.40}$$

and the normalization condition

$$\int_0^{\infty} S(\omega/\omega_c)d(\omega/\omega_c) = 1 \tag{2.41}$$

the normalized formula for the spectral distribution of synchrotron radiation becomes

$$\frac{dW}{d\omega} = \frac{2q^2\gamma}{9\epsilon_0 c} \cdot S(\omega/\omega_c). \tag{2.42}$$

This distribution is shown in Figure 2.14. The low- and high-frequency approximations are shown in the figure as red and blue line.

$$\frac{dW}{d\omega} \approx \frac{q^2}{c} \cdot \left(\frac{\omega\rho}{c}\right)^{1/3} \qquad\qquad \text{for } \omega \ll \omega_c \tag{2.43}$$

$$\frac{dW}{d\omega} \approx \sqrt{\frac{3\pi}{2}} \cdot \frac{q^2}{c} \cdot \gamma \cdot \left(\frac{\omega}{\omega_c}\right)^{1/2} \qquad\qquad \text{for } \omega \gg \omega_c \tag{2.44}$$

The green line at the critical frequency divides the area under the curve into two parts with equal radiated power.

26
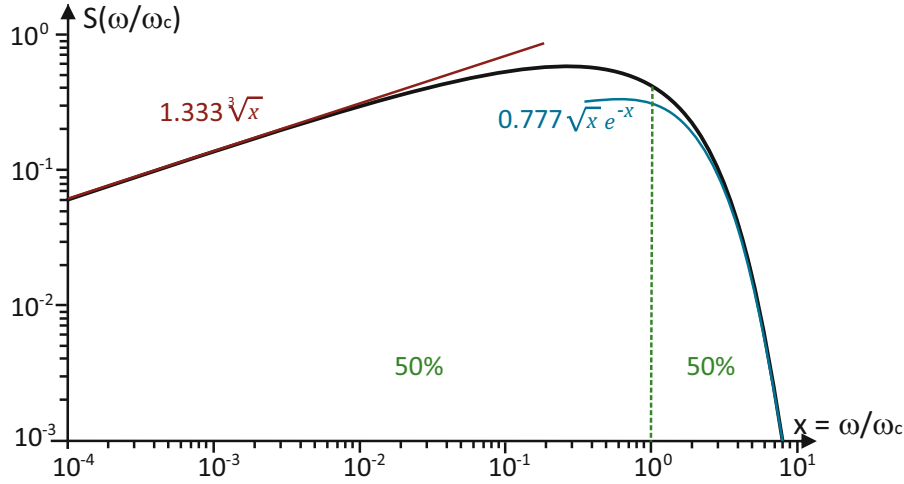
Figure 2.14: Normalized frequency distribution of radiated energy. Figure adapted from[21].

Characterization of synchrotron radiation

The critical frequency ω_c can be used to calculate the critical energy ε_c and critical wavelength λ_c. Using practical units for electrons,

$$m_0 c^2 = 0.511 \, \text{MeV} \Rightarrow \gamma = \frac{E}{m_0 \cdot c^2} = 1957 E[\text{GeV}],$$

this yields:

$$\varepsilon_c = \hbar \omega_c = \frac{3}{2} \cdot \frac{\hbar c \gamma^3}{\rho} \approx 2.218 \frac{E^3}{\rho} = 0.665 E^2 B \tag{2.45}$$

$$\lambda_c = \frac{2\pi c}{\omega_c} = \frac{4\pi}{3} \cdot \frac{\rho}{\gamma^3} \approx 5.59 \cdot \frac{\rho}{E^3} = 18.6 \frac{1}{E^2 B} \tag{2.46}$$

Here, ε_c is given in [keV], λ_c in [Å], ρ in [m], E in [GeV] and B in [T].

The radiated power per second and unit angle at the observers position can be calculated, when the radiated power of one electron (equation 2.36) is multiplied with the number of electrons, that is the average beam current I_b in [A] divided by the elemental charge e. In practical units this gives:

$$\frac{d^3 P}{d\Omega d\omega} = \frac{d^3 W}{d\Omega d\omega} \cdot \frac{I_b}{e}$$

$$= 2.124 \cdot 10^{-3} E^2 I_b \left(\frac{\varepsilon}{\varepsilon_c}\right)^2 \cdot \left(1 + \gamma^2 \theta^2\right) \cdot \left[K_{2/3}^2 \left(\xi\right) + \frac{\gamma^2 \theta^2}{1 + \gamma^2 \theta^2} \cdot K_{1/3}^2 \left(\xi\right)\right] \tag{2.47}$$

Another important quantity to describe synchrotron radiation is the brilliance, that is the flux of photons per unit area of the radiation source per unit solid angle of the

radiation cone and per unit spectral bandwidth.

$$\frac{d^5N}{dtd\Omega dSd\lambda/\lambda}[photons \cdot s^{-1} \cdot mm^{-2} \cdot mrad^{-2} \cdot (0.1\%bandwidth)^{-1}] \tag{2.48}$$

This quantity is also called spectral brightness, and it is generally agreed on to be the proper quantity to characterize and compare the radiation properties of third-generation sources[22]. The brightness is obtained by integrating equation 2.48 over the source area, and hence has the unit $[photons \cdot s^{-1} \cdot mrad^{-2} \cdot (0.1\%bandwidth)^{-1}]$, and the spectral flux is the brightness integrated over the solid angle, with unit $[photons \cdot s^{-1} \cdot (0.1\%bandwidth)^{-1}]$.

For an experiment, important quantities are the total flux of photons per time at the experiment, and the photon flux density, that is the photon flux per area.

Polarization of synchrotron radiation

One important property of synchrotron radiation is it's polarization. The horizontal (P_h) and vertical (P_v) polarized parts of the radiation correspond to the Bessel-functions in equation 2.36 for a bending magnet. The degree of linear polarization, P_l, can be written as:

$$P_l = \frac{P_h - P_v}{P_h + P_v} = \frac{K_{2/3}^1(\xi) - \frac{\gamma^2\theta^2}{1+\gamma^2\theta^2} \cdot K_{1/3}^2}{K_{2/3}^1(\xi) + \frac{\gamma^2\theta^2}{1+\gamma^2\theta^2} \cdot K_{1/3}^2} \tag{2.49}$$

It can be seen that radiation from a bending magnet is linearly polarized in the horizontal direction, when it is observed in the orbital plane, i.e., $\theta = 0$. Outside the orbital plane, the polarization is elliptical and can be decomposed in its horizontal and vertical components. The relative intensity of these components depends on θ and on the energy. Figure 2.15 shows the normalized relative intensities for four different energies.

Insertion Devices

In modern synchrotrons, the radiation is not generated by bending magnets but by insertion devices such as wavelength shifters, wigglers and undulators. These are magnetic structures that deflect the electrons' trajectory to produce well-defined synchrotron radiation that matches the requirements of the experiment. The insertion devices are located in the straight sections of a storage ring. Therefore, it is necessary that they do not affect the beam stability.

Wavelength shifters consist of three magnetic poles, one strong main pole to produce the synchrotron radiation, and two outside poles with a field opposite to this of
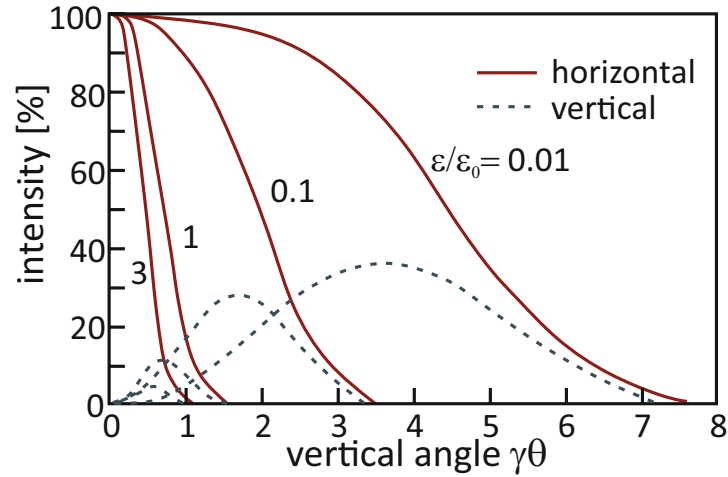
Figure 2.15: Normalized intensities of horizontal and vertical polarization components, as function of the vertical observation angle θ, for different photon energies. Figure adapted from[23].

the main pole, to compensate for the deflection of the electron beam trajectory. The scheme of a wavelength shifter is shown in the inset of Figure 2.16. Using high magnetic fields, *i.e.*, usually between 5 and $10\,\text{T}$[24], this leads to a smaller radius of the electron trajectory as in the case of a bending magnet. This in turn leads to a higher critical energy; the spectrum is shifted. A comparison of the spectra of a bending magnet and a wavelength shifter is shown in Figure 2.16.

Wigglers and **undulators** work after the same principle as wavelength shifters, but instead of three poles, N poles are arranged in a periodic magnet structure with alternating magnetic field, that forces the electrons on sinusoidal trajectories inside the device. The two outer poles are again used for the compensation of the deflection of the electron beam trajectory, all the poles in between are used for the production of synchrotron radiation. An example trajectory is shown in Figure 2.17. The ratio of the electron wiggling angle 2α and the photon emission cone $2/\gamma$ defines the dimensionless parameter K:

$$K = \frac{\alpha}{1/\gamma} = \frac{e}{2\pi m_0 c} \cdot \gamma_u B \tag{2.50}$$

In a **wiggler**, $K \gg 1$. This means that the wiggling angle of the electrons is much wider than the radiation cone. There is no interference between the emission from different poles. As a consequence, the spectrum is relatively broad and continuous, similar to the spectrum of a bending magnet or a wavelength shifter. However, the intensity, compared to a bending magnet, is enhanced by N. The critical energy is shifted as a function of the magnetic filed. The strength of the magnetic field in a wiggler can be changed: When
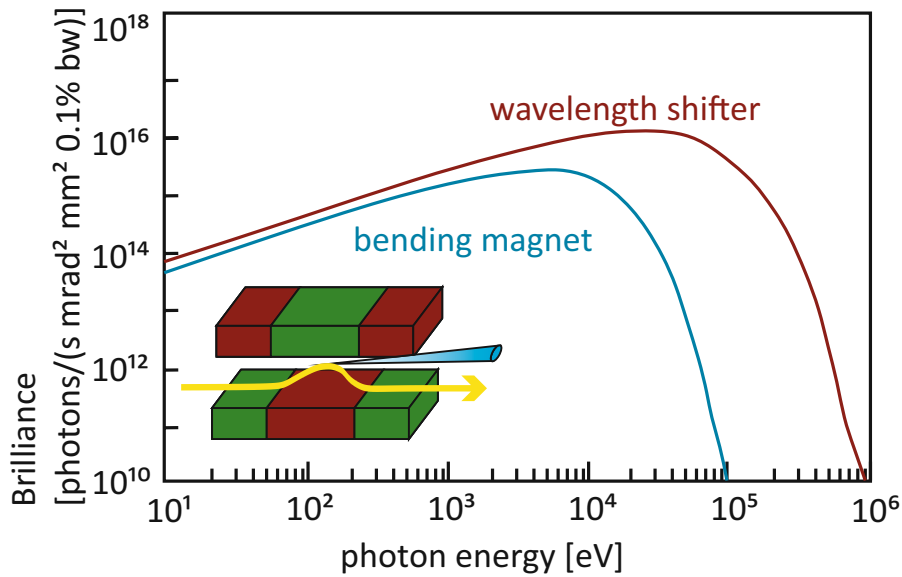
Figure 2.16: Comparison of the spectra of a bending magnet and a wavelength shifter. The electron trajectory in the wavelength shifter (see inset) has a smaller bending radius and the spectrum is shifted to higher energies.
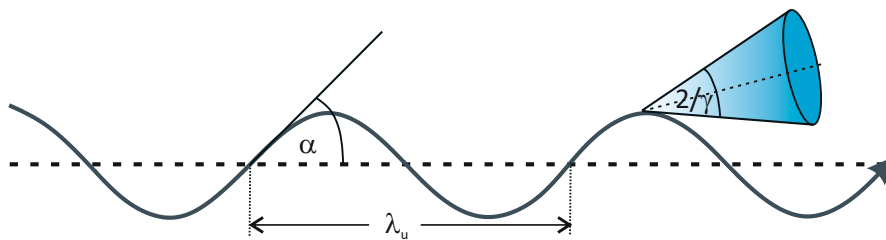
a) Trajectory of an electron in an alternating magnet structure. The alternating magnetic fields force the electrons on a sinusoidal trajectory. The angle α is the half of the electron wiggling angle, the opening angle of the radiation cone is $2/\gamma$. A period of the structure has the length λ_u.
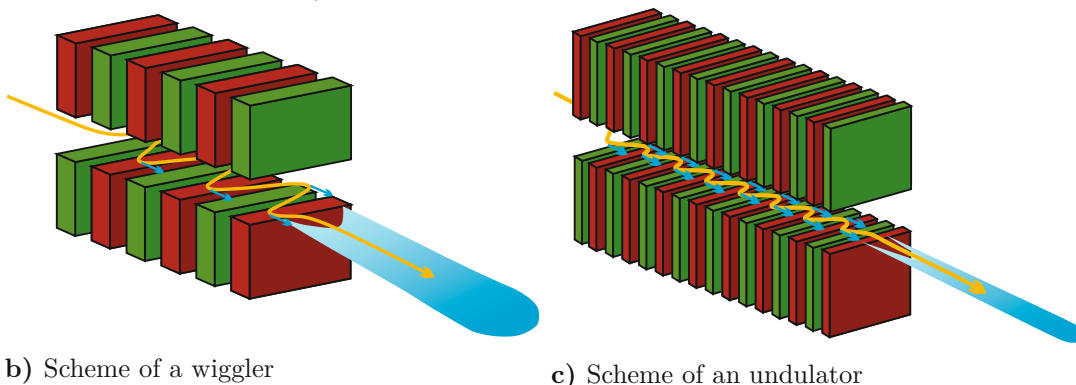
b) Scheme of a wiggler

c) Scheme of an undulator

Figure 2.17: Both, wigglers and undulators, consist of periodic magnetic structures. The difference is the ratio between wiggling angle and photon emission cone.

electromagnets are used, the applied voltage can be changed; when permanent magnets are used, the gap between the magnets can be changed, thus changing the magnetic field.
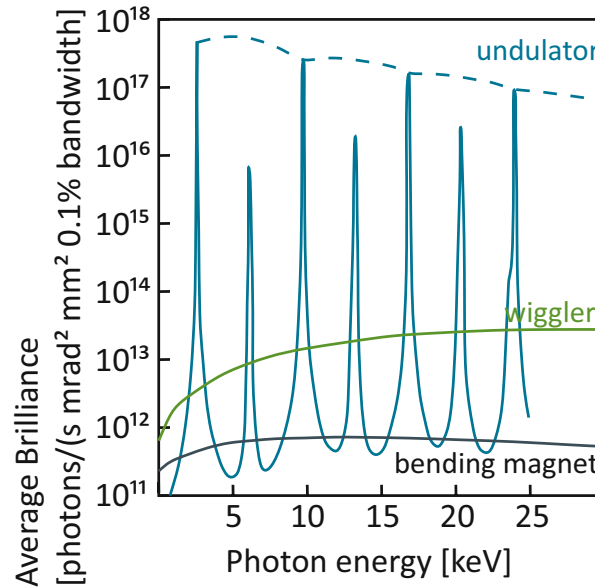
Figure 2.18: Qualitative comparison of spectra of different insertion devices. Figure adapted from [25].

For an **undulator**, $K \leq 1$. The deflections of the beam trajectory are smaller, and usually the period length λ_u is shorter than in a wiggler. This leads to overlapping radiation cones that interfere. The energy of the emitted photons is usually lower than in a wiggler, when the electron energy is the same, but the brightness is higher. The wavelength of the emitted photons can be calculated for wigglers and undulators according to the undulator equation:

$$\lambda = \frac{\lambda_u}{2\gamma^2} \cdot \left(1 + \frac{K^2}{2} + \theta^2 \gamma^2\right) \tag{2.51}$$

The undulator spectrum is not continuous, but consists of lines. These lines are more distinct, the smaller K is. Additionally, as can be seen in equation 2.51, the wavelength of the emitted photons depends on the angle θ between undulator axis and observation direction. The larger the angle, the longer the wavelength. The main part of the radiation is emitted in a cone of an opening angle of $2/\sqrt{N}\gamma$.

A qualitative comparison between the spectra of a bending magnet, a wiggler, and an undulator is shown in Figure 2.18. More spectra of radiation sources are shown in Figure 2.6.

2.3 BAM*line* at BESSY II

All experiments in this work have been performed at the BAM*line* at the synchrotron radiation facility Berliner Elektronenspeicherring-Gesellschaft für Synchrotronstrahlung BESSY II (Helmholtz Zentrum Berlin, HZB). Therefore, a brief overview over the BESSY II electron storage ring and the design and experimental possibilities of the BAM*line* will be given in this section.

2.3.1 BESSY II

BESSY II is a third generation electron storage ring that produces synchrotron radiation for research purposes. Electrons from an electron gun are pre-accelerated in a linear accelerator and a synchrotron and then injected in the electron storage ring. It has a circumference of 240 m and is equipped with a magnet structure consisting of 32 bending magnets to keep the electrons on their orbit. The energy of the electrons is 1.7 GeV, and the nominal beam current is 300 mA.

Since 2015 the top-up mode is provided at BESSY II. This means that the electrons are injected roughly every 90 to 120 seconds rather then every eight hours (decay mode) as before 2015. The advantage of the top-up mode is a near-constant beam current, which is especially important for long-time experiments, *e.g.*, some μCT measurements. Compared to the decay mode, the average photon flux is higher.

Different fill patterns of the ring are possible. The electrons travel around the ring (240 m) in 800 ns, which equals a frequency of 1.25 MHz. The standard fill pattern is a **multi bunch** hybrid pattern. Around 300 electron bunches with a length of 45 ps (or 0.0135 m) (FWHM) are filled in the ring, and in addition there is one longer (80 ns) and more intense bunch in the 200 ns wide so-called ion cleaning gap, and seven so-called slicing bunches of 80 ns width on top of the multibunch train, that can be used, *e.g.*, for time resolved measurements. In **single bunch** operation, only one bunch of electrons circulates in the ring. As can be calculated from the energy of the electrons and the circumference of the ring, this single bunch has a frequency of 1.25 MHz. This operation mode is especially suitable for time resolved measurements. The beam current in single bunch mode is only 13 mA. However, also other experiments where very high photon flux is not necessary, can be performed during single bunch operation, for example X-ray fluorescence measurements. Single bunch operation is offered during two weaks of a year. In the **low-alpha** mode the number of electrons in every bunch is decreased, allowing a narrower spatial distribution of the electrons in a bunch. As a consequence, the length of the electron bunches is decreased to 7 ps (mode A) or 16 ps (mode B), resulting in shorter photon pulse length of the synchrotron radiation and an increased coherence. Low alpha operation is offered during two weaks of a year. Not all beamlines can be

operated during low alpha operation.

At around 50 experimental stations different experiments can be performed, mainly in the soft X-ray range from below 1 keV to around 15 keV. Various methods are offered at the different experimental stations, including:

- X-ray absorption spectroscopy (XAS)

- (Angular resolved) X-ray photoelectron spectroscopy (XPS/ARPES)

- Ultraviolet photoelectron spectroscopy (UPS)

- (micro-) X-ray fluorescence spectroscopy ((μ-)XRF)

- X-ray tomography and topography

- Resonant Inelastic X-ray scattering (RIXS)

- X-ray magnetic linear/circular dichroism (XLCD/XMCD)

- Infrared spectroscopy

- X-ray diffraction (XRD)

- Small/wide angle X-ray scattering (SAXS/WAXS)

- Protein crystallography

- Photon metrology

2.3.2 BAM*line*

The BAM*line* is a hard X-ray beamline at BESSY II, that has been installed in 2000 in a cooperation of the Federal Institute for Materials Research and Testing (Bundesanstalt fuer Materialforschung und -pruefung, BAM) and the National Metrology Insitute of Germany (Physikalisch-Technische Bundesanstalt, PTB). The main elements, that are shortly described in the next sections, are the insertion device, a 7 T wavelength shifter, and two optical elements, a double-multilayer monochromator (DMM) and a double-crystal monochromator (DCM), in the optical hutch. Additionally, the beamline comprises a slit system, a filter system, a main beamshutter before the wall of the ring and a secondary beam shutter behind the optical elements. All optical elements are in a vacuum that reaches values less than 1×10^{-8} mbar, pumped continuously by ion getter pumps in diode and triode configuration. Figure 2.19 shows the optical layout of the beamline with all its components that are located in the optical hutch and their

respective distance to the source, *i.e.*, the wavelength shifter. An exit window with an additional horizontal and vertical slit pair is located at the end of the vacuum tube. The optical hutch is followed by the experimental hutch. The BAM*line* is used mostly for X-ray fluorescence, X-ray absorption, micro computed tomography, and X-ray refraction topography applications.
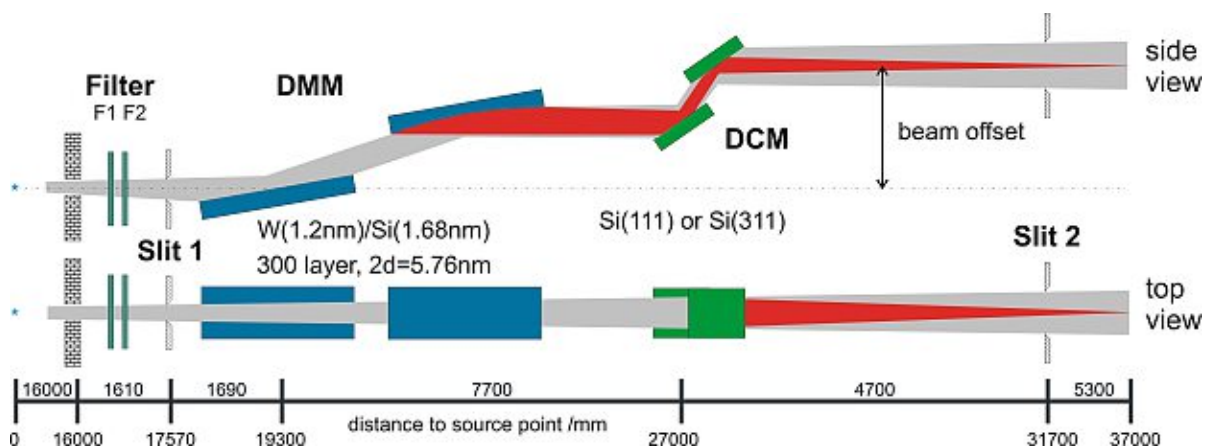
Figure 2.19: Optical layout of the BAM*line*. All the components shown here are located in the optical hutch. In the figure, the two monochromators, DMM and DCM, are in the beam. It is also possible to use them separately. The distances to the source, *i.e.*, the wavelength shifter, are indicated for every component, as well as the distances between two components. Upper part: side view; lower part: top view. Figure taken from internal documentation of BAM*line*.

Wavelength shifter

The insertion device is a superconducting 7 T wavelength shifter (WLS), that is located inside the storage ring in a straight section. It has been constructed and installed by the Budker Institute, Novosibirsk[24]. The main pole has a field strength of 7 T, the two side poles have a strength of 1.5 T. Additionally, to avoid deviations from the electron orbit, two steering magnets are placed as correctors at both sides of the WLS. The magnet field resulting from this arrangement of magnets is shown in Figure 2.20, together with the orbit of the electrons traveling through this structure. Usually, only the synchrotron radiation produced at the main pole is used for the experiment. The characteristic energy of the WLS is 13.5 keV for the BESSY II standard electron energy of 1.7 GeV. The regularly used energy range is 4 keV to 60 keV, but up to 100 keV the photon flux is considerably high. Figure 2.21 shows the photon flux density of the WLS compared to a 1.3 T bending magnet at the same ring current settings, *i.e.*, an electron energy of 1.7 GeV and a current of 300 mA, which are the standard values for BESSY II, calculated with the python software package xrt[26].
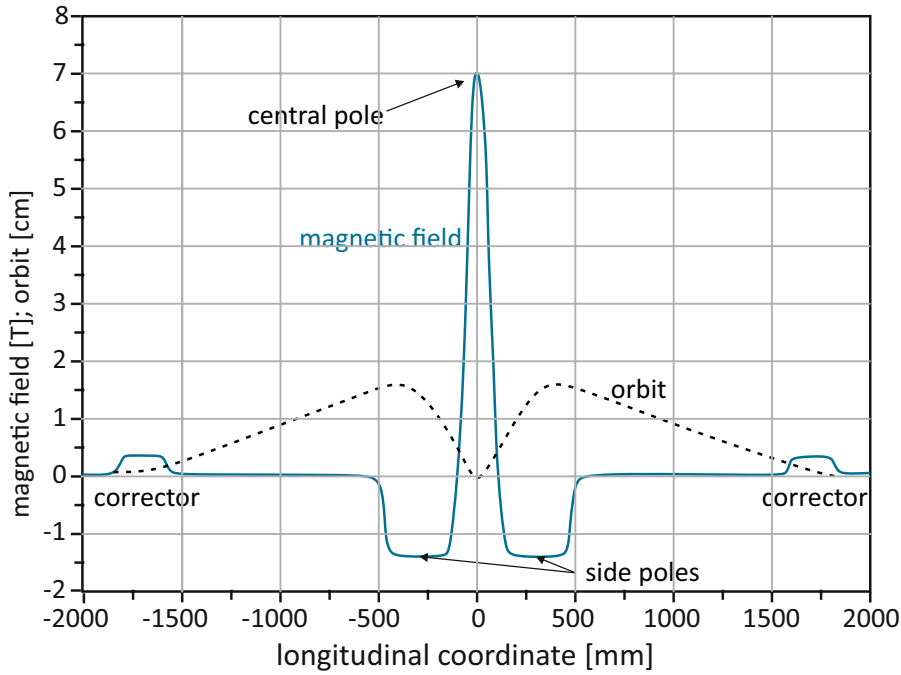
Figure 2.20: Magnet field (solid blue line) and electron orbit (dashed line) in the wavelength shifter. Figure adapted from[24].
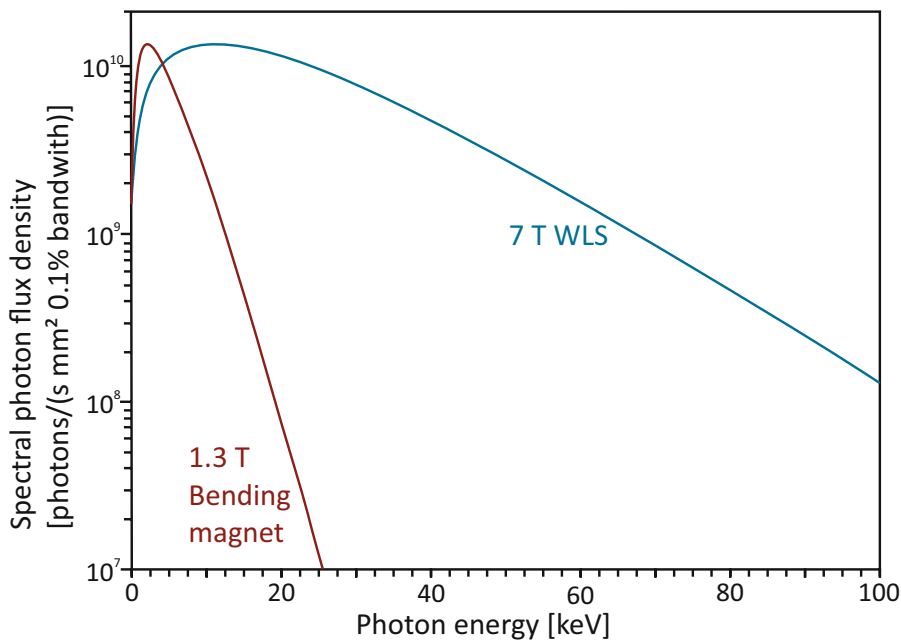
Figure 2.21: Calculated spectral photon flux density of the white beam in the orbital plane at the experimental position (37 m distance from the source) of the 7 T WLS and of a bending magnet, calculated for beam energy $E = 1.7$ GeV and beam current $I = 300$ mA. Figure provided by Michael Sintschuk (BAM), based on caclculations with the python software package xrt[26].

position	1	2	3	4	5
rack F1	0.6 mm Be	0.2 mm Cu	0.2 mm Al	1.0 mm Al	no filter
rack F2	0.2 mm Be	0.05 mm Cu	1.0 mm Cu	0.5 mm Al	0.06 mm Al

Table 2.1: Available filters at BAM*line*

Beam shutters

There are two beam shutters, one that separates the WLS from the optical hutch, and one after the DCM. The beam shutters consist of massive blocks of tungsten that absorb all radiation. The direction of the BAM*line* is the same as the straight section in the storage ring. That means that beside the synchrotron radiation also the Bremsstrahlung of the electrons that collide with residual gas atoms can be seen. The Bremsstrahlung can reach energies up to the energy of the electrons. The beamshutter is constructed such that this radiation can also be blocked. The hutches are provided with an interlock system that ensures that they can only be entered, when the beam shutters are closed. For the entering of the experimental hutch it is sufficient to close the secondary beam shutter. During an experiment, the primary beamshutter remains usually open. This provides a constant heat load on the optical elements. Otherwise it could come to geometrical instabilities due to temperature changes.

Filter and slit system

The white beam coming from the source has a large spectral range and a high photon flux density (see Figure 2.21) and thus a high power density. When the DMM is used, the transmitted energy consists of the adjusted DMM energy and the total reflected low energies, that can be filtered out. The exit window is very sensitive to low energies, and must be protected from beam damage. This is the main goal of the filter system. Different filter foils are mounted on the two movable, water cooled filter racks. They can be used in arbitrary combinations. The available filters are listed in Table 2.1.

The filters can also be used for example to reduce the heat load at the following optical components, or to avoid the scattering contribution of energies that are not necessary for the experiment, or just to reduce the photon flux at the experiment. This can be advantageous, *e.g.*, for the adjustment of new, sensitive detectors.

The slit system inside the optical hutch consists of slits 1 and 2. Each of the slits consists of four blades that can be moved independently, two in horizontal direction, two in vertical direction, to influence the horizontal and vertical size of the beam. The opening of slit 1 should not be too large, to avoid unwanted scattering contributions and heat load. It should be guaranteed that the beam is not larger than the irradiated

area on the first multilayer or crystal of the first monochromator in the beam path. The function of slit 2 corresponds to that of slit 1. Slit 2 is the last optically effective component inside the optics hutch. It is mostly used to reduce the scattering radiation caused by the optical elements, and to define the position of the outcoming beam.

Double-multilayer monochromator DMM

The DMM at the BAM*line* was redesigned in 2019. Most of the experiments in this work were conducted using the former multilayer, that will be described in the following. Until 2019, the DMM at the BAM*line* consisted of two multilayer mirrors, each of which built of 150 periods of alternating layers of tungsten with a thickness of 1.2 nm and silicon with a thickness of 1.68 nm (W/Si) on a smooth polished silicon substrate as required for X-ray mirrors, with a surface roughness of 0.3 nm. The usable area had a length of 300 mm and a width of 60 mm.

Each multilayer mirror is mounted on a rotation table, that means that the rotations of the single mirrors are decoupled from one another. The range of angles reaches from 0° to 3°. Additionally, the second mirror has translation stage in beam direction with a range of 1 m. This translation determines together with the multilayer angles the height difference (offset) between the incoming and the outgoing beam. For a fixed offset, a defined and limited usable energy range can be calculated.

The second multilayer can be bent in the meridional direction to a radius from 1.5 km to 10 km to focus or collimate the beam. The minimum reachable vertical focus size is 0.1 mm. The heat load on the first multilayer mirror makes a water cooling system necessary. Figure 2.22 shows the calculated photon flux density of the DMM at the experimental position. The changes in photon flux density around 10 keV are due to the tungsten L absorption edges.

The multilayer monochromator can be used under Bragg conditions or in total reflection ('mirror mode'). When used under Bragg conditions, the energy resolution of the former DMM was around $dE/E = 1.7\%$[27]. When operated in total reflection ('mirror') mode, the angles of the multilayer mirrors are about four times smaller. As a consequence, the usable horizontal beam width is smaller as under Bragg conditions, hence the reachable photon flux is reduced.

The DMM can be used in combination with the DCM as pre-monochromator to reduce the heat load on the first crystal of the DCM. When the DMM is used to collimate the beam, the energy resolution of the DCM can be improved because it depends on the angular divergence of the incoming beam. Additionally, the DMM can be used to suppress the higher harmonics very effectively.

After the redesign in 2019 there are three stripes, each 20 mm wide, one palladium
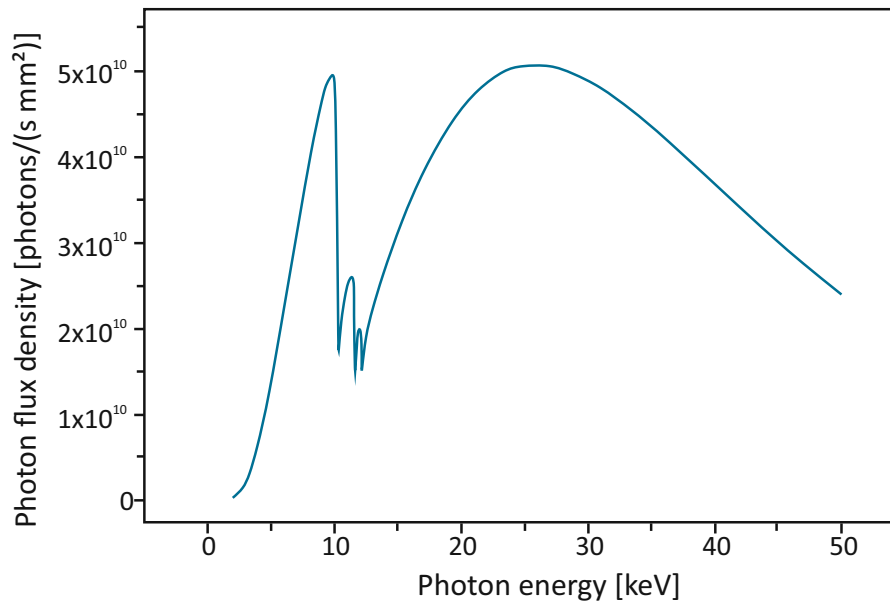
Figure 2.22: Calculated photon flux density for the orbital plane at the experimental position for a beam current of $I = 100\,\mathrm{mA}$ and electron energy $E = 1.7\,\mathrm{GeV}$. At around $10\,\mathrm{keV}$ the W L absorption edges cause the structure of the spectrum. Figure adapted from [27].

layer and two different multilayer on a silicon substrate. The coatings were applied by AXO GmbH (Dresden, Germany). The first multilayer stripe consists of 70 periods of tungsten and silicon (W/Si) and has between $5\,\mathrm{keV}$ and $50\,\mathrm{keV}$ an average energy resolution of $dE/E \approx 1.9\%$ (except for the range of the tungsten absorption lines); the second consists of 180 periods of molydenum and boron carbide (Mo/B$_4$C) and has an average energy resolution of $dE/E \approx 0.45\%$ (calculated with xrt[26]). This second multilayer is chosen such that it can be used in the energy range around $10\,\mathrm{keV}$, in the region of the tungsten absorption lines of the W/Si multilayer coating. The different stripes are selected by moving the whole multilayer with the supporting construction horizontally perpendicular to the beam direction. The mechanical parts of the DMM has not been changed during the reconstruction.

Double-crystal monochromator DCM

Both crystals of the DCM are mounted on the same rotation table. The surface of the first crystal is fixed to the axis of rotation, and the second crystal can be moved laterally and vertically, to ensure that the beam reflected by the first crystal hits the second crystal, and to allow to chose a specified offset. Both crystals are equipped with a motor to adjust the roll angle. Additionally, the second crystal is equipped with motors that allow a fine adjustment of the pitch and yaw angles. This is necessary to optimize the angle of the second crystal relative to the first. A detuning of the angles can lead to a

dramatic loss in photon flux, because the intrinsic bandwidth of the crystals is very low ($dE/E \approx 1.37 \cdot 10^{-4}$ for the Si(111) and $dE/E \approx 2.90 \cdot 10^{-5}$ for Si(311)[28]) and the Bragg condition must be fulfilled for both crystals. The second crystal can be bent sagittally to radii down to 1 m, thus allowing a horizontal focusing of down to 0.25 mm. The DCM can be equipped with two different pairs of crystals, either Si (111) or Si (311). The resolving power of the Si (311) is even higher than that of the Si (111), but has also a lower photon flux (see Figure 2.23). The smaller bandwidth compared to the DMM
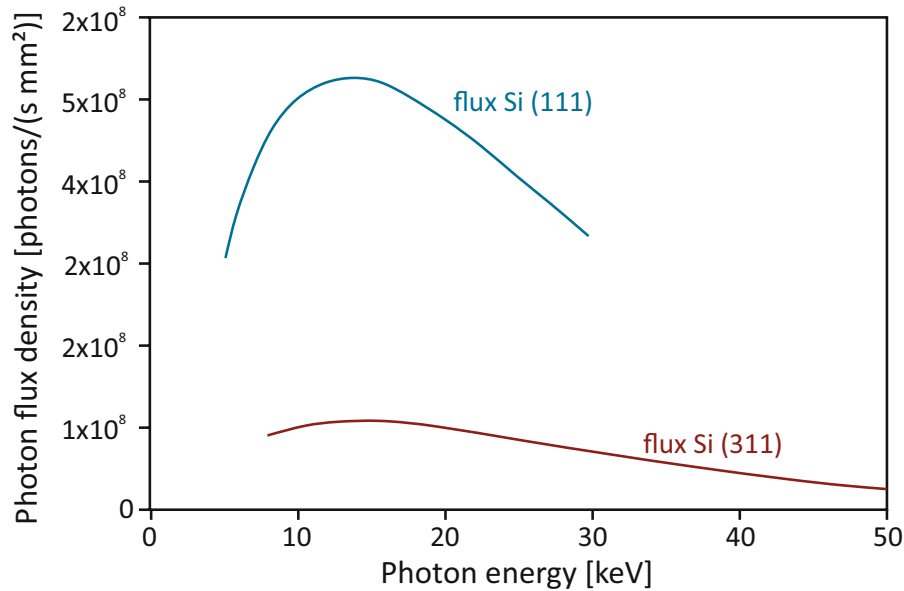
Figure 2.23: Calculated photon flux (solid lines) of the Si (111) (blue) and the Si (311) crystal at the experiment position for a ring current of 100 mA and electron energy of 1.7 GeV. Figure adapted from [29].

means an even higher heat load of the first crystal, as only a small part of the power that reaches the crystal is transmitted, and the rest is absorbed in the crystal. Therefore, the first crystal of the DCM is mounted on a water cooled Cu block.

When the beam is focused by the bending of the second mirror of the DMM and the second crystal of the DCM, it is possible to reach a beam size of about 0.25 mm in horizontal and 0.1 mm in vertical directions. In the center of the focused beam the photon flux density is about two orders of magnitude higher than for the unfocused beam.

Experimental hutch

The experimental hutch follows the optical hutch. It can only be entered when the secondary beam shutter is closed. Inside the hutch is the experimental station. The BAM*line* is a very versatile beamline and has no fixed end station. Instead, a large

range of possible experiments is available. Various X-ray spectroscopic methods can be used, mostly for non-destructive material characterization. These methods comprise micro computed tomography, X-ray refraction topography, radiometry (PTB), X-ray fluorescence analysis, and X-ray absorption spectroscopy.

2.4 X-ray based spectroscopic methods

The interactions of X-rays with matter are already described in section 2.1. The fact that X-rays are attenuated when passing through matter is the basis for X-ray spectroscopic methods. In the following, the principles of X-ray absorption fine structure spectroscopy (XAFS spectroscopy) and X-ray fluorescence spectroscopy (XRF spectroscopy) are shortly described. Both methods allow non-destructive investigation and characterization of different samples.

2.4.1 X-ray absorption fine structure spectroscopy

XAFS spectroscopy deals with the characteristics of attenuation of X-rays of energies near the absorption edges of the element to be investigated. XAFS spectroscopy is element specific; the measurements can usually be performed straightforward, and the sample can be crystalline or amorphous, solid powder, or liquid. Additionally, it is non-destructive. This makes XAFS spectroscopy to a widely used method for material characterization, in many different areas of research, including biology, catalysts research, and material sciences. XAFS spectroscopy delivers chemical and structural information about the sample. This method entails both XANES (X-ray absorption near edge structure) and EXAFS (extended X-ray absorption fine structure) spectroscopy (see Figure 2.24).

The two parts of a XAFS experiment can be measured in the same experiment, but they provide different information. XANES implies the transmission of the core electron to unfilled bound states, nearly bound states and the continuum, with a low kinetic energy of the photoelectron. XANES can give valuable information about the coordination geometry (*e.g.*, tetrahedral or octahedral), the oxidation state and unfilled or partially filled states. EXAFS includes only transitions to the continuum, and the resulting photoelectron has a high kinetic energy. It can be used to determine the local environment of the atom to be probed, such as nearest neighbor distances, coordination numbers and the atomic species of the neighbors.

The attenuation of X-rays in matter is element specific, as the energy levels and differences between the energy levels in an atom are also element specific. In the case of one isolated atom, the X-ray absorption is decreasing with increasing photon energy,
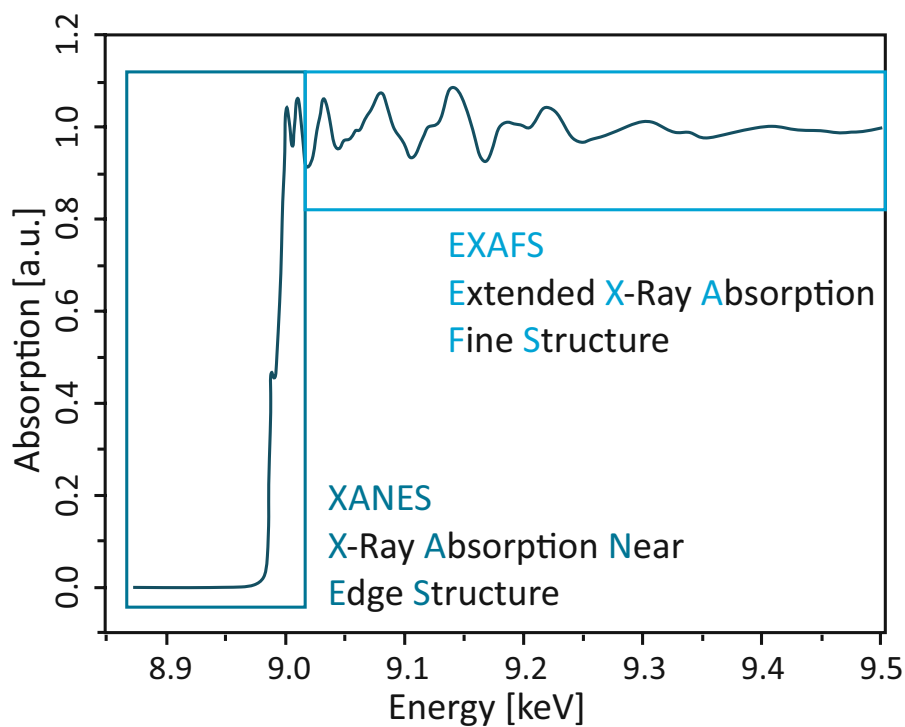
Figure 2.24: Example for a XAFS spectrum. The region before and up to $\approx 50\,\text{eV}$ above the edge is called the XANES region, the EXAFS includes the region from $\approx 50\,\text{eV}$ to $\approx 1000\,\text{eV}$ above the edge.

with sharp jumps at the so-called absorption edges. These edges occur at energies, where the incoming photon can release an electron of a shell of the atom; this increases the absorption probability.

A XAFS experiment can be performed in two ways: either in transmission or in fluorescence (see Figure 2.25). In both modes, the spectrum is obtained by varying the
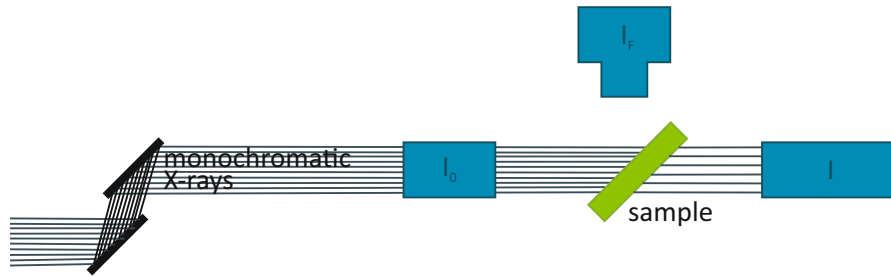
Figure 2.25: Simple scheme of a XAFS experiment. The sample absorbs a part of the incoming, monochromatic X-rays. The ratio of the intensities before and after the sample is a measure for the absorption. As fluorescence is a direct consequence of the absorption, the fluorescence radiation can also be used to determine the absorption. The spectrum is obtained by scanning the energy.

energy of the incoming X-rays and measuring the absorption coefficient as a function of the energy. This requires a tunable X-ray source with a good energy resolution and high flux. Synchrotron radiation is ideal for XAFS experiments. Important features are the stability and accuracy of the used monochromator.

In a transmission experiment, the absorption is obtained by measuring the attenuation of the X-rays passing through the sample. The intensities are usually measured with ionization chambers before (I_0) and after (I) the sample. Considering the Lambert-Beer law (Equation 2.6), the absorption coefficient is obtained by taking the logarithm of the ratio of the incoming and transmitted intensities.

$$\mu\left(E\right)x = -ln\left(\frac{I}{I_0}\right) \tag{2.52}$$

To obtain a decent absorption profile, some attention must be drawn on the sample. It should be homogeneous and free of pinholes. The sample thickness must be chosen carefully. Usually, the aim is to have an edge step $\Delta\mu(E_0) \cdot x$ of ~ 1. The required thicknesses range from less than $10\,\mu$m, for example for pure iron, up to several millimeters for dilute solutions. For low concentrations it can be necessary to measure in fluorescence mode because the absorption in the sample is not high enough.

The XAFS can also be measured in fluorescence mode. As the fluorescence radiation

is a direct consequence of the absorption, it is proportional to the absorption coefficient.

$$\mu\left(E\right) \propto \frac{I_F}{I_0} \tag{2.53}$$

Fluorescence measurements are often performed when the sample is thick or has a very low concentration. The incoming X-rays produce fluorescence but are also scattered. The scatter peak can be greatly suppressed by placing the detector at 90° to the incoming beam in the horizontal plane, because synchrotron radiation is usually polarized and hence the scattering distribution is not isotropic (see section 2.2). Commonly, energy-dispersive semiconductor detectors are used for fluorescence measurements. These can be Ge or Si(Li) detectors or silicon drift detectors (SDDs). With these detectors, the fluorescence spectrum of the sample is recorded, that can be used for the determination of the elemental composition. The intensity of the fluorescence radiation is determined by considering the area under the fluorescence peak of interest. It is proportional to the attenuation coefficient. Hence, by plotting the fluorescence intensity as a function of the incoming energy an absorption spectrum can be obtained. An important effect that must be considered when measuring XAFS in fluorescence is the self absorption in the sample. For example, for thick, concentrated samples, almost all incoming X-rays are absorbed by the element of interest. At energies with a lower attenuation coefficient μ the penetration depth is larger, and more fluorescence radiation is produced than at energies with a higher attenuation coefficient. As the fluorescence radiation escape depth is normally longer than the penetration depth, almost all fluorescence photons can escape. As a consequence, more fluorescence photons are detected at energies with lower μ, and less at energies with higher μ. This damps the XAFS oscillations. The effect can be neglected in the case of very thin or thick, dilute samples. Otherwise, the spectra must be corrected for self absorption effects, or a suitable measurement geometry, *e.g.*, the grazing exit or total reflection geometry, must be used in the experiment to avoid this effect.

For the understanding of the structure of an X-ray absorption spectrum, it is necessary to have in mind the basics of electron configuration in atoms. In the atomic physics model, the electrons in an atom are arranged in shells. The principal quantum number, n, of an electron indicates the corresponding shell. The first shells are the K- ($n = 1$), L- ($n = 2$) and M- ($n = 3$) shell. The electrons in a shell are grouped in subshells with the same azimuthal quantum number, l, where $l = [0, 1, ..., n - 1]$. The subshells are labeled $s, p, d, f, ...$ corresponding to $l = 0, 1, 2, 3, ...$ To complete the set of the four quantum numbers, there are the magnetic quantum number, m_l, ranging from $-l$ to l, and the spin quantum number, s, that can take the values $1/2$ and $-1/2$ for an electron.

The edge with the highest energy is the K-edge, if the incoming photon releases an

electron of the K-shell with principal quantum number $n = 1$. The two electrons, that can be located in this shell, have the same azimuthal quantum number $l = 0$ and the same total angular momentum quantum number $j = 1/2$. Thus, they have the same binding energy, and there is only one edge. The next edges are the L-edges, where an electron of the L-shell with principal quantum number $n = 2$ is released. Electrons in the L-shell have different binding energies, corresponding to electrons with $l = 0$, that are the $2s$ electrons ($j = 1/2$), and $l = 1$, these are the $2p$ electrons with ($j = 1/2$) and ($j = 3/2$). Therefore, there are three L-edges. Equivalently, there are five M-edges, and so on. Figure 2.5 shows the mass attenuation coefficient for lead, with a general decrease for increasing energies, and the absorption edges.

In EXAFS spectroscopy, the fine structure can be observed when there are neighboring atoms. The released electron, the photoelectron, has an energy that depends on the energy of the incoming photon (see Equation 2.4). Following the particle-wave-dualism, the electron can also be considered as outgoing wave with a wavelength corresponding to its energy, according to Equation 2.2. This wave is scattered by neighboring atoms, and the outgoing and backscattered photoelectron wave can interfere, either constructively or destructively, depending on the wavelength and the distances between the absorbing atom and its neighbors, this is shown in Figure 2.26. This interference directly affects the absorption probability. EXAFS can be described theoretically. In the 1970's, Lytle, Say-
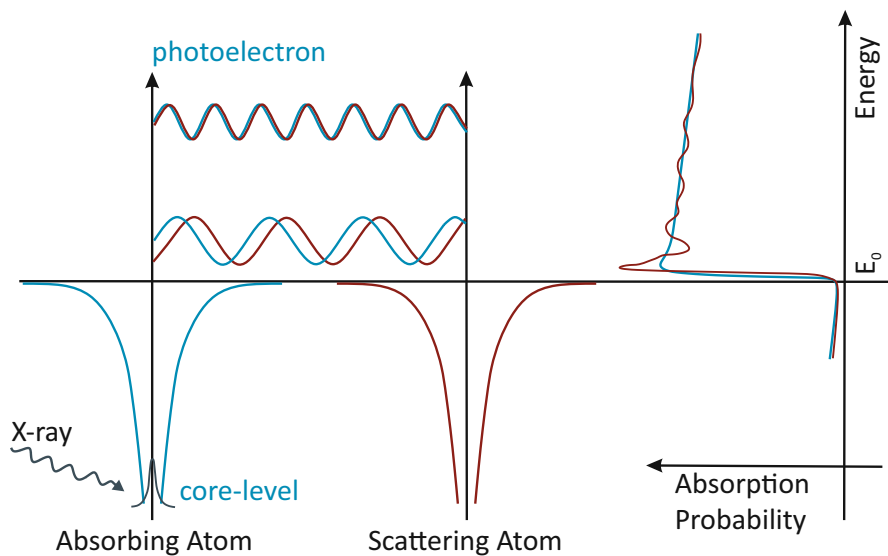
Figure 2.26: Origin of the fine structure of the absorption spectrum. The outgoing photoelectron can be seen as wave that is scattered by neighboring atoms. This influences the absorption probability. Figure adapted from[30].

ers and Stern contributed considerably to the understanding of the theory, but they also described the experimental practice and the determination of the physical parameters

from the experiment[31–33]. The theory is based on scattering theory and the transition probability between an initial state (photon, no photoelectron, no electron vacancy in the absorbing atom) and a final state (no photon, photoelectron, electron vacancy in the absorbing atom). For EXAFS, the electric dipole approximation is appropriate for the transition. This leads to the dipole selection rules between initial and final state:

$$\Delta l = \pm 1; \Delta s = 0; \Delta j = \pm 1, 0; \Delta m = 0 \tag{2.54}$$

In practice, for one-electron transitions, $\Delta l = \pm 1$ means that if the initial state implies a $s-$electron ($l = 0$, for example K and L_I edges), the final state has $p-$symmetry, $e.g.$, $l = 1$, and the other way round: if the initial state has $p-$symmetry ($l = 1$, for example L_{II} and L_{III} edges), the final state can have either $s-$ ($l = 0$) or $d-$symmetry ($l = 2$). However, quadrupol- and higher order transitions can also contribute to the EXAFS or the pre-edge structure, but dipole-forbidden transitions have a significantly lower probability to occur.

As the final state depends on the neighboring atoms, $i.e.$, the scatter amplitude f and phase shift δ (that depend on the atomic number Z), the coordination number N, the distance to the absorbing atom R, and the (mean-square) disorder of the interatomic distances σ^2, it is possible to model the EXAFS with the EXAFS equation:

$$\chi(k) = S_0^2 \sum_j N_j \frac{f_j(k)}{kR_j^2} \cdot e^{\frac{-2R_j}{\lambda(k)}} \cdot e^{-2k^2\sigma_j^2} \cdot sin\left[2kR_j + \delta_j(k)\right] \tag{2.55}$$

The factor S_0^2 is the amplitude reduction factor, that is related to the contribution of the 'passive' atoms, these are all but the absorbing atom. The sum goes over the so-called shells, these are all atoms of the same species that are located at the same distance to the absorbing atom. λ is the mean free path of the photoelectron. k is the wave number that is related to the energy of the incoming photon E and the edge energy E_0 by:

$$k = \sqrt{\frac{2m_e(E - E_0)}{\hbar^2}} \tag{2.56}$$

If f and δ are known, it is possible to determine the number, distance, mean-square disorder of the neighbor distance, and the species of the neighboring atom from an EXAFS experiment. This means that EXAFS is a probe of the local structure of the investigated atom in the sample.

The data treatment has to be performed carefully. The following steps are illustrated with transmission XAFS data from FeO taken from[30].

- Extract the $\mu(E)$ from the measured intensities

- Subtract a pre-edge function

- Identify the edge position E_0

- Normalize to $\Delta\mu(E) \approx 1$

- Substract the μ_0

- Extract the $\chi(k)$

- k-weight the oscillations and transform into R-space

The EXAFS signal is related to the measured absorption:

$$\chi(E) = \frac{\mu(E) - \mu_0(E)}{\Delta\mu_0(E_0)} \tag{2.57}$$

This equation indicates how to process the measured spectrum to extract the EXAFS signal $\chi(E)$. A pre-edge and post-edge function must be subtracted (see Figure 2.27). For the identification of the edge energy E_0, often the maximum of the derivative of μ
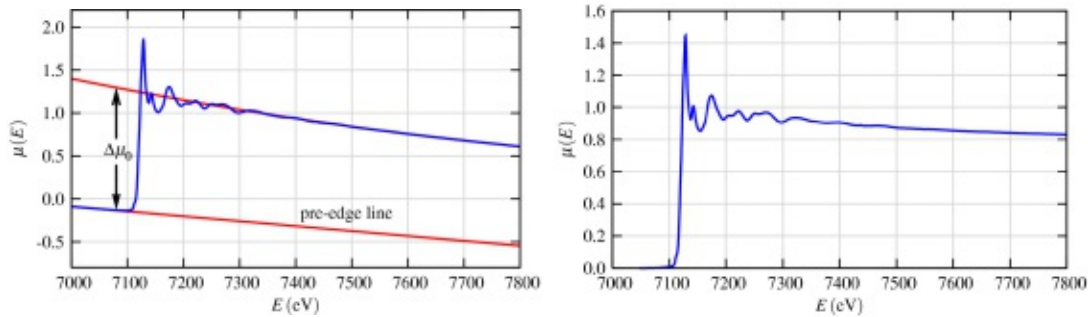
a) Measured absorption profile with pre-edge and post-edge line and edge jump

b) Measured absorption profile after subtraction of the pre-edge line, and normalized to edge step 1

Figure 2.27: Pre-edge and post-edge line and edge jump

(see Figure 2.28) is used. Once the edge position determined, the EXAFS oscillations are normalized to one absorption event by dividing the spectrum by the edge step $\Delta\mu_0(E_0)$ (see Figure 2.27). To get only the XAFS oscillations, the 'bare atom' background, μ_0, is subtracted (see Figure 2.29). As μ_0 is not known, it must be fitted with an appropriate function. At this point, the XAFS can be displayed as a function of the wavenumber k (see Equation 2.56), or a power of k (see Figure 2.30). This $k-$weighting ensures that the amplitude of the XAFS signal is amplified at higher wave numbers. The oscillations can best be analyzed in the $R-$space, so the data is Fourier-transformed. In this step, the choice of the window is of great importance for the quality of the results. The real
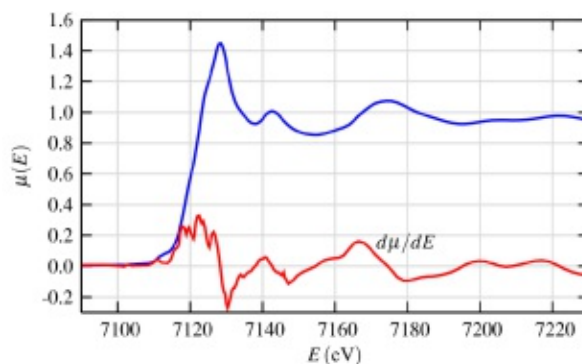
Figure 2.28: The position of the maximum of the derivative $d\mu/dE$ is often chosen as edge position E_0
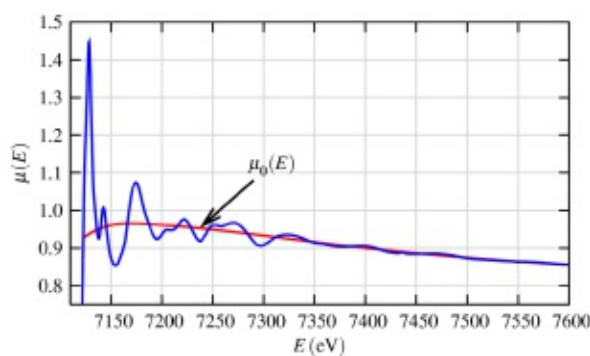
Figure 2.29: Subtraction of the 'bare atom' background μ_0
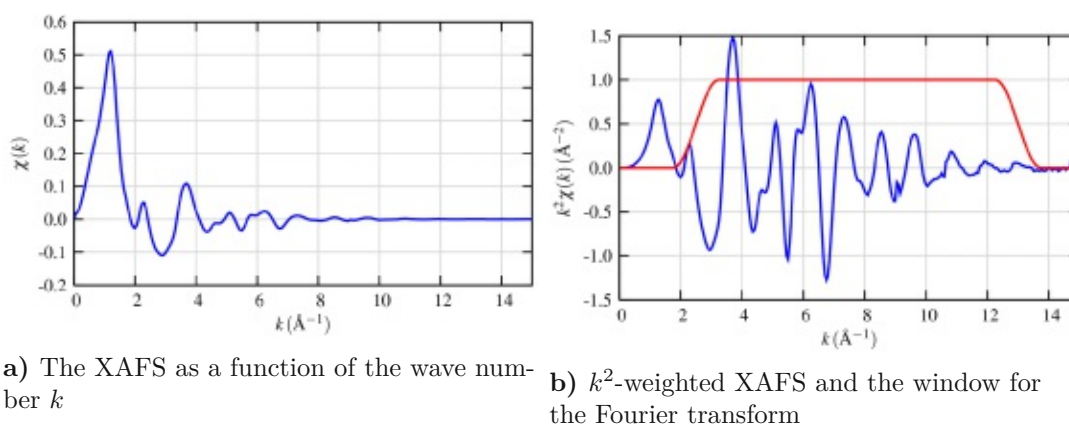
a) The XAFS as a function of the wave number k

b) k^2-weighted XAFS and the window for the Fourier transform

Figure 2.30: XAFS as a function of k. To amplify the oscillations at higher wave numbers, usually the XAFS function is weighted with a power of k, here k^2.

part of the data in the R-space gives a radial distribution of the photoelectron scattering profile, *i.e.*, the positions of the neighboring atoms (see Figure 2.31).
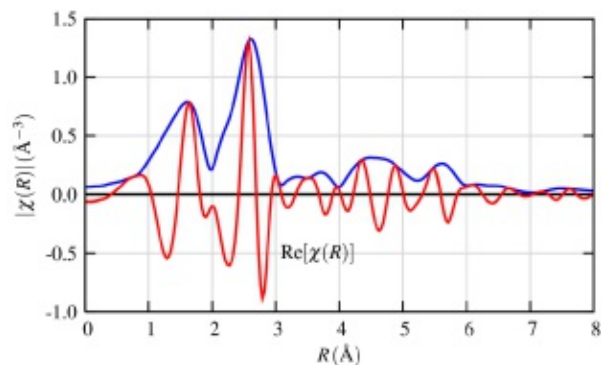
Figure 2.31: The real part $\mathrm{Re}(\chi(R))$ (red) and the magnitude $|\chi(R)|$ (blue) of XAFS in the R-space.

For more complex samples, it is necessary to decompose the spectrum according to the contributions of the different types of neighbors and the bonding configuration. The scattering amplitude f and the phase shift δ depend on the atomic number. They can be calculated with different programs, for example FEFF[34–36] or FDMNES[37]. These functions are used for EXAFS modeling, and the calculations for structures close to the expected structure, in turn, can help in the analysis of EXAFS data, *i.e.*, improve the fit to get better structural parameters. For the data treatment, an appropriate software, such as Athena[38], can be used. The EXAFS signal can also contain contributions from scattering paths that involve more than two atoms. Hence, it is also possible to retrieve n-body information about the investigated sample from an EXAFS spectrum.

The XANES part of the absorption spectrum can not be processed in the same way as the EXAFS part. The EXAFS equation (see Equation 2.55) breaks down for low k, and there is no XANES equation. As the photoelectrons in the XANES region have a low kinetic energy, they have a large mean free path λ. As a consequence, scatterer at longer distances from the absorbing atom contribute to the XANES. This means also, that multiple scattering becomes more important in XANES than in EXAFS. All these facts make theoretical approaches to XANES difficult. Nevertheless, the XANES region contains important information about the sample. First of all, the XANES spectrum can be used as a fingerprint. Reference spectra can be used to determine unknowns. Next, the XANES is sensitive to the oxidation state. The position of the edge shifts to higher energies for higher oxidation states (shown for example in[39]). A simple explanation for this phenomenon is the reduced number of electrons in higher oxidation states, so the core charge is less shielded and the binding energy of the remaining electrons increases. Features before the edge, the pre-edge features, provide information on transitions to

bound states. This implies the dipole allowed transitions with $\Delta l = \pm 1$, *e.g.*, for the K-edge $1s \to np$, but also dipole forbidden transitions, which give raise to a weaker feature. The intensity of dipole allowed transitions gives information about the available $p-$states. Dipole forbidden transitions can arise when $p-$ and $d-$ orbitals are mixed. This, in turn, can give information about the coordination geometry, as the probability of the mixing increases with increasing distortion from centrosymmetry, *i.e.*, is lower for octahedral than for tetrahedral symmetry. The so-called white line is a high peak just above the edge. It can be observed for example in $4d$ transition metals, and is here a direct probe of the number of unoccupied $4d$-states. As the multiple scattering has more contributions in XANES than in EXAFS, it is in principle possible to reconstruct the 3D local environment of the absorbing atom. The calculation of XANES spectra has improved over the last decades[35]and allows to get information out off the measured data by fitting with predicted spectra. With the raise in available computing power, also machine learning methods are used to predict XANES spectra[40].

2.4.2 X-ray fluorescence spectroscopy

In X-ray fluorescence (XRF) spectroscopy, the characteristic fluorescence radiation is detected. This technique is widely used for elemental and chemical analysis, as it is fast, non-destructive, and easy to use. The applications are widespread, and include, *e.g.*, the investigation of biological tissue, minerals, new materials, archaeological and art objects. XRF can be used as a sensitive quantification tool in research, for the process control in the metal or other industries. Portable hand-held XRF instruments can be used in the field, for example for the determination of contamination, in buildings or generally for samples that cannot be transported to a laboratory. Depending on the geometry of the experimental setup, the source and the beam size, XRF spectroscopy can be further specified:

- XRF (with X-ray tubes)

- synchrotron radiation XRF (SR XRF)

- wavelength-dispersive XRF (WDXRF)

- energy-dispersive XRF (EDXRF)

- micro / nano (μ/n XRF)

- total reflection XRF (TXRF)

- glancing incident XRF (GIXRF)

- 2D scanning XRF

- 3D confocal μXRF

Here, only the main principle of XRF spectroscopy will be presented. The annual atomic spectrometry update - advances in XRF spectrometry (*e.g.*[41]) contains information about the state of the art and advances in different XRF techniques.

XRF can be used to determine the elemental composition of a sample. A quantification is also possible. Scanning methods can be used to generate element distribution maps.

The fluorescence radiation can be detected in two ways: With a wavelength-dispersive detector system or with an energy-dispersive detector.

In WDXRF the fluorescence radiation is collimated and then an analyzer crystal is used to detect a selected wavelength. This method provides an excellent energy resolution and enables high count rates and a low spectral background, as only a single selected energy is detected at a time. This, in turn, allows a precise quantification of the element concentration. A flexible setup uses a goniometer to rotate the crystal and the detector to fulfill the Bragg condition for the desired wavelength. This requires a high precision and the readjustment of the geometry between the measurements. The simultaneous measurement of more than one element is possible, when more detectors at fixed angles are used. However, this setup is less flexible. The used detectors can be flow proportional counter for low energies, or scintillators for higher energy radiation.

For EDXRF, an energy-dispersive detector is necessary, for example a Si(Li) solid state semiconductor or a silicon drift detector (SDD). The energy-dispersive detector allows the simultaneous acquisition of a whole fluorescence spectrum. Figure 2.32 shows an example spectrum. The energy-dispersive measurement has the advantage that multiple elements can be detected at once. It is more flexible than the WDXRF setup and can be used in different geometries, such as TXRF or GIXRF. However, the spectral background is higher and the energy resolution worse. In addition, the detector can become saturated fast by the fluorescence radiation of major elements. To perform a successful XRF experiment an get the most out of the data, different strategies can be used. To avoid the detection of scattered radiation, polarized X-rays, *e.g.*, from a synchrotron can be used, and the detector can be placed at an angle of 90° relative to the incoming beam in the horizontal plane. If a matrix element with an atomic number higher than the element of interest is present, the energy of the excitation radiation can be chosen to be below the absorption edge energy of this matrix element. Filters can be used to filter out low-energy excitation radiation that is not in the range of the absorption edge energies of the elements under investigation. For low concentration samples, a TXRF setup can be considered. In this geometry, the self absorption is reduced, and the elements in the sample are excited two times, by the incoming and reflected X-rays. In addition, the
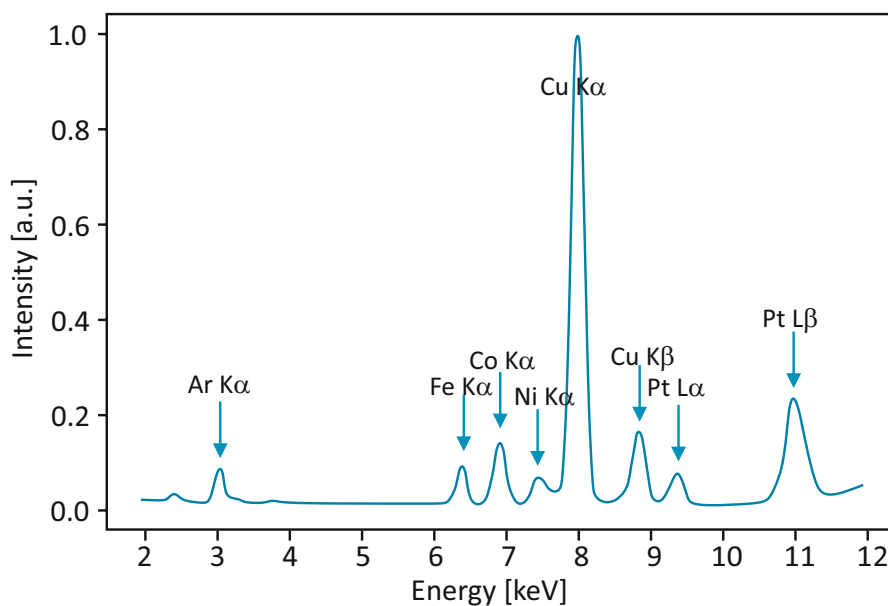
Figure 2.32: Example XRF spectrum. This spectrum was recorded with a pnCCD detector (see section 4.3.3). With the exception of copper, the K_β emission lines are not visible as they have a too low intensity. The K_{alpha_1} and K_{alpha_2} lines can not be resolved with the used detector.

detector can be close to the sample, allowing a large solid angle. Furthermore, when an internal standard is used, the quantification is straightforward. In general, the basis for the quantification is the net area under the peak of interest. If peaks are overlapping, a peak deconvolution must be performed to resolve the different peaks.

3 Dispersive X-ray Absorption Fine Structure Spectroscopy

3.1 Introduction

The principle of X-ray absorption fine structure spectroscopy (XAFS) has already been described in section 2.4. The main advantages of this spectroscopic method are that it is element specific, non-destructive and can deliver information about the local environment, bond length, electronic states and orbitals of various samples, including amorphous samples. These benefits can also be used for time-resolved in-situ/in-operando experiments, *e.g.*, in the investigation of catalyst processing, for phase transformation, or thin-film deposition. For this type of experiments it is necessary that the time to record one spectrum is significantly shorter than the timescale of the investigated reactions/processes.

In the next sections, an overview over the possibilities of time-resolved XAFS spectroscopy is provided in section 3.1.1. The aims of the development of a new setup for time-resolved XAFS spectroscopy and its principle are described in section 3.1.2. Preliminary work for the characterization of the properties of the developed setup are presented in sections 3.1.3 and 3.1.4. In section 3.2, a detailed description of the experiments conducted at the BAM*line* is given, followed by the discussion of the results in section 3.3.

3.1.1 Time-resolved X-ray absorption fine structure spectroscopy

There are two possibilities to perform time-resolved XAFS spectroscopy, the quick scanning EXAFS (QEXAFS) and dispersive XAFS (DXAFS).

The QEXAFS mode that was first proposed by R. Frahm in 1988[42]. Instead of measuring the XAFS spectrum point-by-point, the monochromator is moved (quasi) continuously and very fast so that the acquisition time for one spectrum can be reduced significantly. In the last decades there have been considerable progresses and the QEXAFS method is meanwhile well-established[43]. Whole spectra can be recorded in the millisecond range. At different synchrotron facilities exist dedicated QEXAFS

beamlines. For example, at the new beamline P64 (PETRA III, Hamburg), fully operating since April 2017, a time resolution in the 20 ms to 100 ms range is achieved[44]. Another example is the Super-XAS beamline at the Swiss Light Source (SLS) at the Paul Scherrer Institute. XANES spectra can be measured in 10 ms and EXAFS spectra in 17 ms based on an optimized setup (new monochromator, ionization chambers and data acquisition system) installed in 2015[45]. The beam is focused onto the sample with a width of typically 100 µm x 100 µm and a lateral precision of 50 µm due to the moving of the monochromator during the scan. Another example for QEXAFS is the BM23 beamline at ESRF where QEXAFS on the second timescale and a spot size of 4 µm x 4 µm is achieved[46]. These are impressive examples of very elaborated experiments at dedicated beamlines. The limiting factor for the time resolution of QEXAFS is the monochromator speed, and the reproducibility of the monochromator positions and the beam stability at this high speed. Additionally, a high photon flux is required to get enough statistics and collect high quality spectra even in a short measurement time.

Another approach for time-resolved XAFS spectroscopy is dispersive XAFS (DXAFS) spectroscopy. In this method a polychromatic beam with the desired bandwith is diffracted by a dispersive element, usually a cylindrically bent crystal. Every energy is reflected under a different angle, according to Bragg's law. The diffracted beam is focused on the sample and afterwards recorded by an area sensitve detector, *e.g.*, a CCD-based system. This setup was first presented by Matsushita and Phizackerley in 1981[47]. A simplified scheme of the setup is shown in Figure 3.1. The advantages are the absence of moving components during the experiment and hence a high intrinsic beam stability and the recording of the whole spectrum in a single shot allowing fast measurements. Since the first presentation of this method the performance of DXAFS experiments has been investigated in detail and continuously improved[48–50] but the principle has remained the same. Today dispersive XAFS spectroscopy is in operation at the ID24 beamline at ESRF[51,52], at the ODE beamline at SOLEIL synchrotron[53], and at the I20-EDE beamline at Diamond Light Source[54]. ESRF has developed a Fast Readout Low Noise (FReLoN) CCD camera, which enables 20 frames per second. Nowadays, a beam size of 5 µm x 5 µm with a time resolution of about 60 ms can be achieved[52]. As only one dimension of the beam is used for the energy resolution the second beam dimension can in principle be used for lateral resolution. The use of the DXAFS method for simultaneous time- and lateral-resolved measurements has been reported by Katayama *et al.*[55]. They use a flat beam that is diffracted in one direction and has a line shape at the sample position. In the line direction a lateral resolved investigation of the sample is possible. The limiting factor for the time resolution in DXAFS spectroscopy is the readout speed of the detector. Generally, spectroscopic CCD-based detectors have a readout time of tens of milliseconds. As in the QEXAFS method, another limiting
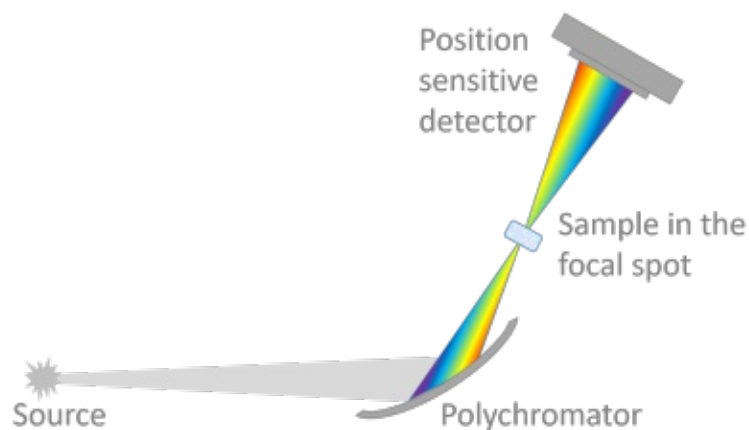
Figure 3.1: Simplified scheme of the dispersive XAFS spectroscopy setup. The beam of the desired energy bandwidth is diffracted by a so called polychromator, usually a cylindrically bent crystal. After passing the sample in the focal spot the beam is detected by an area sensitive detector.

factor is the photon flux of the source.

Both methods introduced above are well-established and widely used but they can only be performed at dedicated beamlines with highly specialized instrumentation. However, for many applications there is no need for such high temporal resolutions and it would be advantageous to have a stable, easy to implement and flexible possibility for time-resolved XAFS spectroscopy with a time resolution in the second range.

In the course of this work, such a solution has been developed and first tests and measurements have been performed at the BAM*line* at BESSY II (HZB Berlin). This new setup works with a bent convexly curved crystal as dispersive element that is placed behind the sample so that the transmitted beam is diffracted and unwanted scattering is prevented. The crystal can be flexibly bent allowing to adapt the setup to different energies and energy ranges.

3.1.2 A setup for time- and spatial resolved X-ray absorption fine structure spectroscopy

The aim of the project was to develop a setup for time- and lateral-resolved XAFS spectroscopy that is stable, flexible and easy to implement and use. The targeted time-resolution is in the second range. In summary, a beam with the desired energy bandwidth passes through the sample and is afterwards dispersed by a convexly bent Si(111) crystal. This means that the different energies are reflected under different angles and hence spatially separated. The dispersed beam is then detected by an area sensitive CCD camera. The scheme of the setup is shown in Figure 3.2.
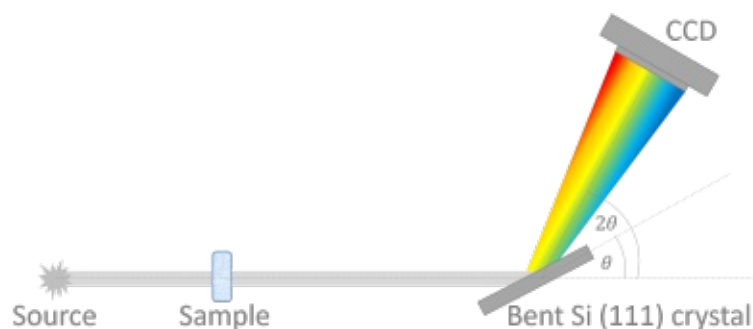
Figure 3.2: Scheme of the new dispersive XAFS spectroscopy setup. The beam of the desired bandwidth passes through the sample and is diffracted afterwards by a dispersive element, a bent Si (111) crystal. The different energies are reflected under different angles and hence spatially separated. They are recorded by an area sensitive CCD detector.

One important difference to the established DXAFS setup is the placement of the sample before the dispersive element. The Si(111) crytal is placed under an angle of θ relative to the incoming beam. This requires the detector to be placed at an angle of 2θ relative to the incoming beam. This $\theta - 2\theta$ geometry prevents other effects from being detected, such as scattering. It ensures that only the transmitted X-rays are reflected, and no slit system is necessary. A wafer bender allows the flexible and reproducible bending of the crystal to adapt the setup easily to different experimental needs. There are less geometrical requirements for the different elements compared to the classical DXAFS setup. As the sample is placed before the dispersive element, it doesn't need to be placed in the focal spot, there is no need to place the dispersive element or the detector on a Rowland circle, and the adjustment of the slit positions is omitted as there are no slits. The sample has to be homogeneous in the dimension of the dispersion. Inhomogeneities or different thicknesses would lead to different absorption at different positions, and consequently distort the absorption profile.

3.1.3 Preliminary considerations

The central component of the setup is a bent Si(111) crystal (wafer). It is used as dispersive element meaning that the incident polychromatic beam is reflected at different points on its surface depending on the energy. This is a direct result of Bragg's law that describes the reflection of X-rays on crystals by the following formula:

$$n \cdot \lambda = 2 \cdot d \cdot sin(\theta) \tag{3.1}$$

λ is the wavelength of the incoming beam, d is the lattice plane spacing of the reflecting material, in this case (Si(111)) $d = 3.1356\,\text{Å}$, and θ is the angle of incidence. With

$$E = h \cdot \nu$$

$$\text{and} \quad \nu \cdot \lambda = c$$

$$\Leftrightarrow \nu = \frac{c}{\lambda}$$

$$\Rightarrow E = \frac{h \cdot c}{\lambda} \tag{3.2}$$

it is possible to calculate the energy of radiation of each wavelength. Thus a spatial separation of photons of different energies is possible, enabling to detect a spectrum with an area sensitive CCD camera in a single shot. It is crucial to know the properties of the bent wafer to adjust the setup and adapt it to the different experimental requirements. Therefore, some experiments with simple means have been performed as well as simulations of the bending depending on the applied forces . The obtained bending line is the basis of the program for the simulation of the beam path, described in section 3.1.4. Moreover, a mechanism had to be developed that is easy to handle and allows a quick, stable and reproducible bending of the wafer. This wafer bender has been improved continuously until good results in synchrotron experiments were obtained.

Geometrical considerations on the bending of the wafer

The aim of the first measurements on the surface of the bent wafer was to quantify the bending behavior and use the results for the preparation of different experiments at the synchrotron. Therefore, a simple distance laser was used as light source and the reflection of the laser beam at different points on the wafer surface was investigated for different applied bending forces.

The base for the experiment is the reflection law: the angle of incidence of a beam hitting a mirror, or in this case a crystal, is equal to the reflection angle. Therefore the beam path is easy to calculate, if one knows the geometrical arrangement of the elements source, crystal and screen.

For the planar crystal, all incoming parallel beams are reflected under the same angle. In the experiment, the source is at a fix position, the crystal is placed perpendicular to the wall that acts as screen at an arbitrary but known distance, and moved parallel to the wall. Every displacement of the crystal causes a defined displacement of the reflected beam. For the experimental arrangement it holds that (see Figure 3.3)

$$tan\,(\theta) = \frac{dy_1}{dx} = \frac{h_1}{d} = \frac{dy_2 + h_2}{d + dx}. \tag{3.3}$$
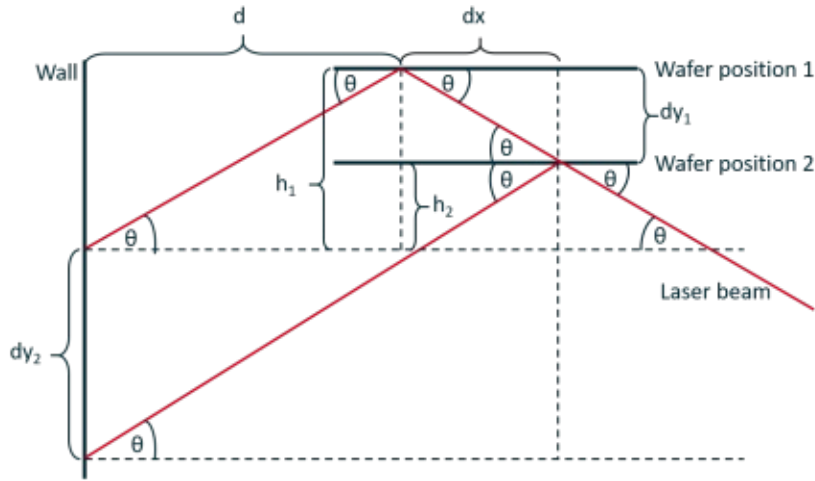
Figure 3.3: Geometrical arrangement of crystal and wall with incoming and reflected beam at different crystal positions

The displacement of the reflected beam on the screen is dy_2:

$$\frac{h_1}{d} = \frac{dy_2 + h_2}{d + dx}$$

$$\Leftrightarrow dy_2 = \frac{h_1}{d} \cdot (d + dx) - h_2$$

$$= h_1 + \frac{dx}{d} \cdot h_1 - h_2$$

$$= h_1 + \frac{dy_1}{h_1} \cdot h_1 - h_2 \quad \left(\text{from } \frac{dy_1}{dx} = \frac{h_1}{d} \right)$$

$$= h_1 + \frac{dy_1}{h_1} \cdot h_1 - h_2 \frac{dy_2 + h_2}{d + dx}$$

$$= h_1 - h_2 + dy_1$$

$$= 2 \cdot dy_1 \tag{3.4}$$

dy_2 is directly proportional to the displacement of the crystal. For a fixed source the reflection point depends on the position of the crystal, hence every point of impact of the beam on the screen can be assigned to a distinct and defined point on the crystal surface.

If the crystal is bent, the direct proportionality between displacement of the crystal and position of the beam on the wall is not given, but the point of impact of the beam on the screen is completely determined by the point of reflection (and thus by the position of the crystal) and the angle between incident beam and crystal surface in this point. The bending can be either constant (*e.g.*, circle line), described by a function (*e.g.*, a

square) or unknown. The angles on the crystal surface, given as the slope of a tangent on the crystal surface in the point of interest, can be used to describe the bending. They can be calculated from the difference ΔP_N between the positions P_{N_p} and P_{N_b} of the beam on the screen reflected by the planar and the bent crystal, respectively, in the same point N, when the distance between the reflection point on the crystal and the screen, L_N, is known (see Figure 3.4 (a)). The angles on the crystal surface (see Figure 3.4 (b))
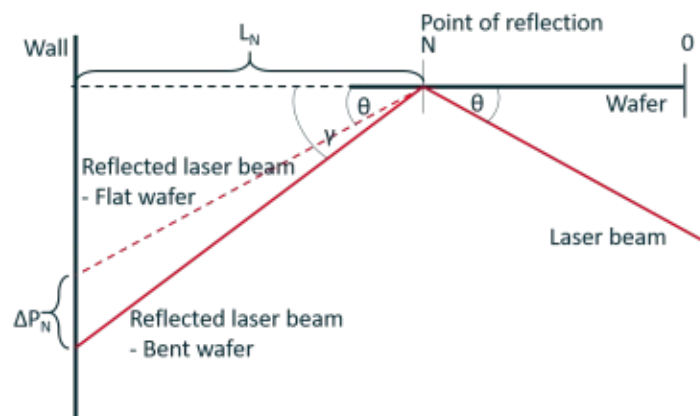
a) Different points of impact on the wall depending on the bending of the wafer
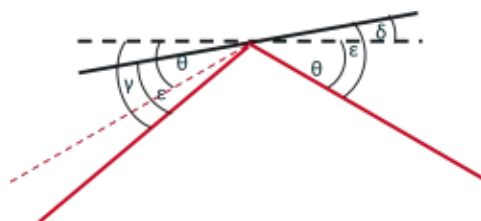
b) Angles at the surface of the bent wafer (solid line) and the planar wafer (dashed line)

Figure 3.4: Calculation of the angles on the wafer surface

are:

θ : angle of incidence and angle of reflection on the planar mirror

ϵ : angle of incidence and angle of reflection on the bent mirror

δ : angle difference between planar and bent mirror

γ : angle between the planar crystal and the reflected beam from the bent crystal

δ is the angle between the planar and the bent crystal and therefore the angle of interest.

$$\delta = \gamma - \epsilon \quad \text{and}$$
$$\epsilon = \theta + \delta$$
$$\Rightarrow \delta = \gamma - (\theta + \delta)$$
$$\Leftrightarrow \delta = \frac{1}{2}(\gamma - \theta) \tag{3.5}$$

θ is the angle of the incoming laser and is determined by the experimental setup. γ can be calculated from the distances between the points of impact of the laser reflected by the planar and the bent wafer as follows:

$$tan(\gamma) = tan(\theta) + \frac{\Delta P}{L_N}$$
$$\Rightarrow \gamma = arctan\left(tan(\theta) + \frac{\Delta P}{L_N}\right) \tag{3.6}$$

δ can be calculated for every point on the surface yielding the slope in every point of the crystal. From these angles a bending line can be derived iteratively (see Figure 3.5). Beginning at a point $(x_0|y_0)$ the next point is $(x_1|y_1) = (x_0 + dx|y_0 + dy_1)$ with a given dx, depending on the points on the crystal that have been investigated, and $dy_1 = dy \cdot tan(\delta_1)$.
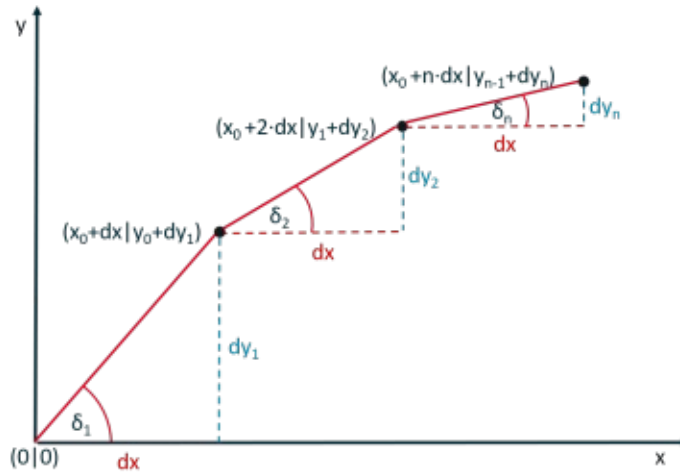
Figure 3.5: Derivation of the bending line

The wafer bender

The first wafer bender that was developed at BAM is shown in Figure 3.6 (a). The wafer was placed onto a vertical rod on a small support. One side of the wafer was fixed, the other side could be moved by means of a micrometer screw to cause a bending of the wafer.

On the base of experiments with this wafer bender, the mechanism was further developed. To obtain a symmetrical, well-defined and reproducible bending, the crystal is placed onto a vertical polished rod. It is held by two steel rods on the left and on the right side with slits to host the crystal. They are joined by an aluminum bar that is fixed on a linear stage with a maximum travel distance of 10 mm. The setup is equipped with a stepper motor and a position recorder to allow symmetrical and reproducible bending of the crystal (see Figure 3.6(b)).

Experimental investigation of the wafer bending

The crystal that was used as dispersive element in the DXAFS spectroscopy setup is a commercially available Si(111) wafer (Siegert Wafer GmbH, Aachen, Germany) with a diameter of 100 mm and a thickness of 525 µm. For the first experiments, the simple
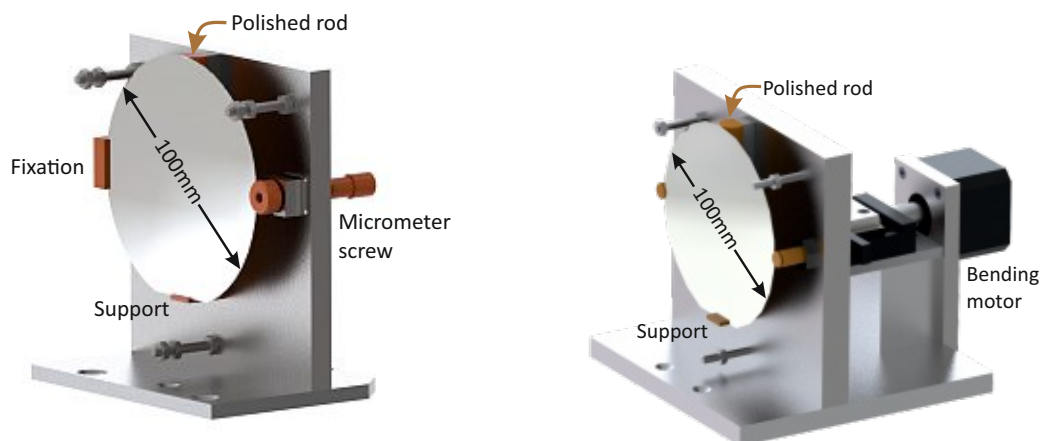
a) Wafer bender mechanism that was used in the experiments for the characterization of the bending properties of the crystal.

b) Wafer bender mechanism that was used in the BAM*line* experiments

Figure 3.6: Two versions of the wafer bender. In both cases the wafer is placed on a support and in the middle on a vertical rod. In the old version (a) it is fixed on the left side, on the right side a force can be applied via the micrometer screw, and this causes the bending of the wafer. In the new version (b) the two sides of the wafer are held by two steel rods. These are joined by an aluminum bar that is fixed on a linear stage. This enables a symmetrical, exact and reproducible bending of the wafer.

version of the wafer bender was used (see Figure 3.6 (a)). The wafer bender with the

wafer was placed on a linear table allowing a precise displacement of the wafer parallel to a wall. The distance d_0 between the middle of the wafer and the wall was measured with a laser rangefinder (Bosch PLR 15). This laser was then used as light source for the experiment. It was placed on a scissor lift table at an angle $\theta \approx 20°$ relative to the displacement direction of the wafer (see Figure 3.7). This angle was checked from the difference of the positions of the beam on the wafer surface for two known positions of the wafer. A paper attached to the wall acted as screen. The first measurements were performed with no applied force, *i. e.*, the planar wafer. The point of impact on the wall of the beam reflected at the fixed edge of the wafer was chosen as origin. The origin was marked. Then the wafer was moved in steps of 1 mm, corresponding to 25000 motor steps, controlled by the position control unit PS10 from OWIS GmbH (Staufen, Germany) with the appurtenant software OWISoft, and every laser point on the wall was marked. Some motor positions were noted on the paper for reference. For different applied forces (*i. e.*, different positions of the micrometer screw) the same procedure was repeated:
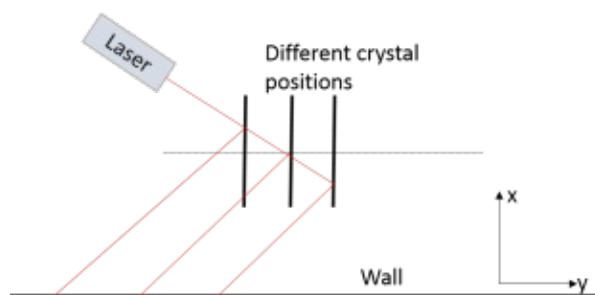
Figure 3.7: Geometrical setup of the experiment for the characterization of the bending behavior.

- Adjust the position 'zero' (origin), always the same position of the linear table. Therefore, the wafer was released to be planar, then the motor was driven to the position where the laser hit the wall in the origin. Afterwards the bending was adjusted with the micrometer screw.

- Move the wafer in steps of 1 mm.

- For every step: mark the point where the reflected laser beam hits the wall. For some steps: note the motor position beside the mark.

- Return to some motor positions at random to check the reproducibility.

The investigated positions of the micrometer screw were 0.4 mm, 0.8 mm, 1.2 mm, 1.6 mm and 2.0 mm. These measurements were repeated for different heights on the wafer surface: directly above the mount, directly below the mount and 1.5 cm below the mount.

The obtained results consist of lines on a paper, which can be attributed to a motor position and therefore to a displacement dy_1 of the wafer, which again corresponds to a defined point of reflection on the surface with the x-coordinate

$$x = dy_1 \cdot tan\left(\theta\right),\tag{3.7}$$

where $x = 0$ is the fixed edge of the wafer.

The coordinate of the point of impact on the wall relative to the origin was measured with a ruler. Thus, pairs of values $\left(x_{N_{wafer}}\middle|y_{N_{wall}}\right)$ can be derived for every considered screw position as well as for the planar wafer. This leads to

$$\Delta P_N = P_{N_p} - P_{N_b}\tag{3.8}$$

where P_{N_p} and P_{N_b} are the y-coordinates of the beam on the wall reflected by the planar and the bent wafer respectively in the same point N. The distance L_N between $x_{N_{wafer}}$ and the wall is

$$L_N = d_0 + \left(x_{middle} - x_N\right).\tag{3.9}$$

The angle δ can now be calculated according to Equation 3.5. If the angle in the middle of the wafer shall be 0, a constant angle correction τ, depending on the screw position, has to be introduced because of the asymmetrical bending which contributes to the shift ΔP_N and is approximately (see Figure 3.8)

$$\tau \approx \frac{d_{wafer}}{screw\ position}.\tag{3.10}$$

The calculations were performed for three different heights on the wafer surface and

Figure 3.8: Angle correction due to the asymmetrical bending of the wafer.

every investigated screw position. Bending lines were constructed as shown in Figure 3.5. Some exemplary results are shown in Figure 3.9.

The angles for different screw positions measured directly above the mount are depicted in Figure 3.9 (a). The results correspond to the expectations. The angles on the wafer surface increase with increasing applied force. In the middle of the wafer, where it is placed on the rod, the angle equals 0 for all screw positions. The fixation on one side (at positions near to 0 mm) and the screw on the other side (at positions near to

100 mm) of the wafer are leading to small discontinuities in the increase of the absolute angle value.

The angles in different heights at a screw position of 2.0 mm are shown in Figure 3.9 (b). Small differences can be observed especially where the wafer is fixed. This means that the wafer is twisted, *i.e.* there is not the same bending line in all heights. This effect should be investigated in more detail and has to be considered when planning experiments with the wafer bender where lateral resolution is needed.

The obtained bending lines for a screw position of 2.0 mm in different heights of the wafer are shown in figure 3.9 (c). As the lines are calculated iteratively, they can only be considered as a qualitative result with increasing errors with raising distance from the origin.

Simulations of the bending behavior

Beside the experiments simulations has been performed with Abaqus software from SIMULIA16 by Cetin Haftaoglu (BAM division Experimental and Model Based Mechanical Behavior of Materials). For this purpose a net of points on the wafer surface was defined. For different applied forces the displacements of these points in x-, y- and z-direction were simulated. The force was simulated as a displacement on one (asymmetrical bending) or on both (symmetrical bending) sides of the of the wafer and perpendicular to its surface. For the asymmetrical bending the boundary conditions are such that at a position of $x =0.10$ m the wafer is fixed. In the middle, where it is placed on the rod, the y-position is set to a shift of 0 mm. The force is applied on the edge of the wafer, in one point at position $x = 0$ mm. For the boundary conditions for the symmetrical bending it is assumed that the wafer is fixed only in the middle and the force is applied in two points at positions $x =0.10$ m and $x =0.00$ m. In both cases the boundary conditions are idealized. In reality the fixation in the experiments consists of a slit to host the wafer which can always sparsely move, and the force is not applied in a single point. Therefore the results of the simulation are not comparable with the experiment on the edges of the wafer. Furthermore, the different heights in the experiment don't correspond to the different heights in the simulation as in the experiment the measurements were performed below and above the fixation and not in the middle of the wafer, so that a direct comparison cannot be drawn. However, the simulations are suitable to check the experimentally obtained results for the qualitative behavior of the wafer. The results of the simulations are shown in Figure 3.10.

The shift in y-direction (Figure 3.10 (a) and (b)) corresponds to the bending line in the corresponding height. The maximum bending is in the point(s) where the force is applied. As the wafer is fixed on the rod, the displacement is equal to 0 in the middle.
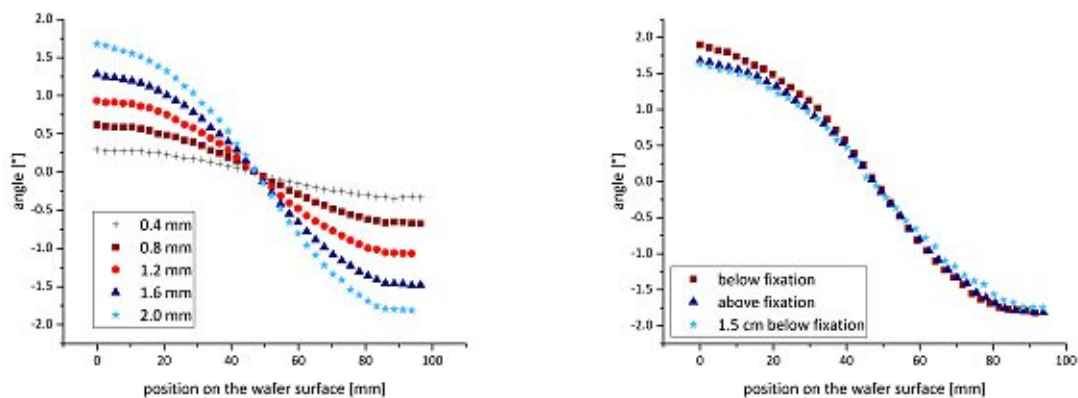
a) Angles on the wafer surface for different screw positions

b) Angles on the wafer surface for different heights
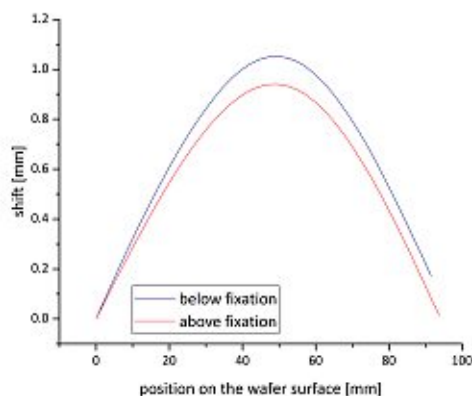
c) Bending line in different heights

Figure 3.9: Results of the experiments on the wafer surface. The angles on the surface are dependent on the applied force i. e. the screw position (a). For the same screw position there are different angles in different heights of the wafer (b), leading to different bending lines (c).
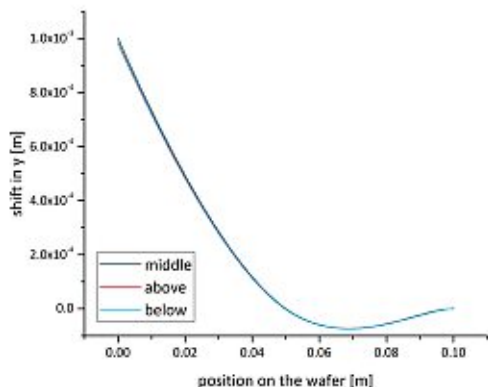
a) Displacement in y-direction, asymmetrically bent
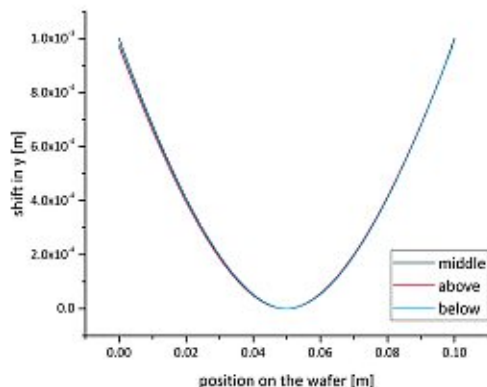
b) Displacement in y-direction, symmetrically bent
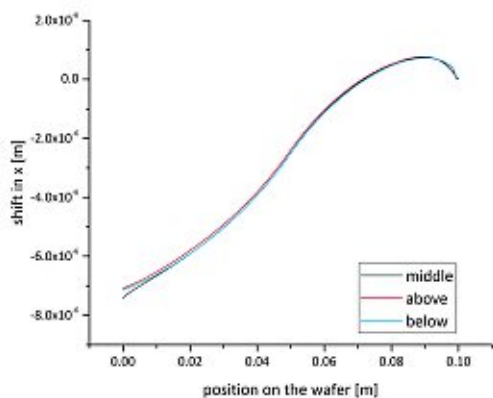
c) Displacement in x-direction, asymmetrically bent
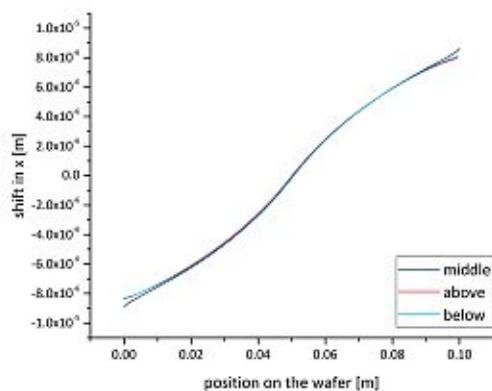
d) Displacement in x-direction, symmetrically bent
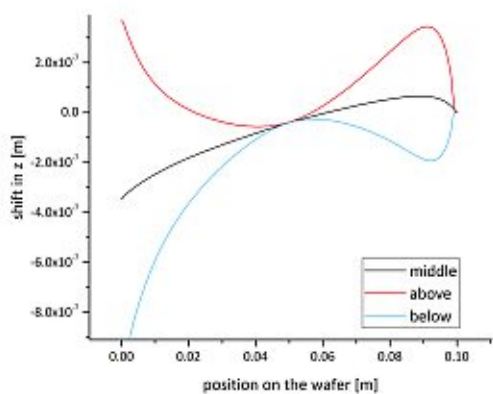
e) Displacement in z-direction, asymmetrically bent
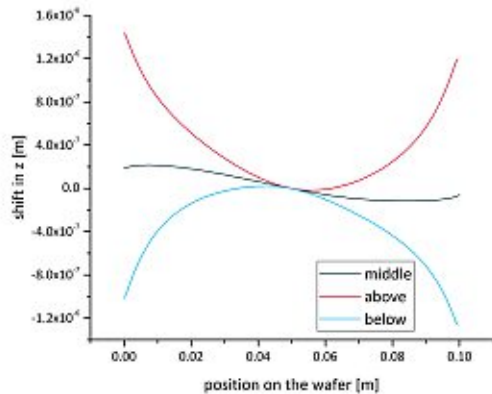
f) Displacement in z-direction, symmetrically bent

Figure 3.10: Results of the simulations with asymmetrical and symmetrical bending of 1 mm. The displacement in x- and z-direction is three orders of magnitude less than the displacement in y-direction.

66

For the asymmetrical bending there is a little negative displacement between $0.05\,\mathrm{m}$ and $0.10\,\mathrm{m}$ and an inflection point near to the edge that is due to the fixed edge and that should not be this distinct in the experiments. There is only a slight difference between the three simulated lines. In the region of about $1\,\mathrm{cm}$ around the middle of the wafer there seem to be less or no differences in the bending line. The visualization of the shift in y-direction for the whole wafer is shown in Figure 3.11. It shows that at greater distances from the vertical middle line, the bending line changes slightly. Simulations with different applied forces show that the y-shifts are proportional to the applied force, *i.e.*, the simulated stresses are in the elastic region of the wafer. The shifts in x-direction are similar for all simulated heights (see Figure 3.10 (c) and (d)). The shifts in z-direction differ depending on the heights (see Figure 3.10 (e) and (f)). Points below the middle are shifted down whereas points above the middle are shifted up. The points in the middle are also slightly shifted and this effect is more pronounced in the asymmetrically bent case. However these displacements in x- and z-direction are rather small (three orders of magnitude less than the displacement in y-direction, *i.e.*, in the μm range) and will not be considered in the further discussion.
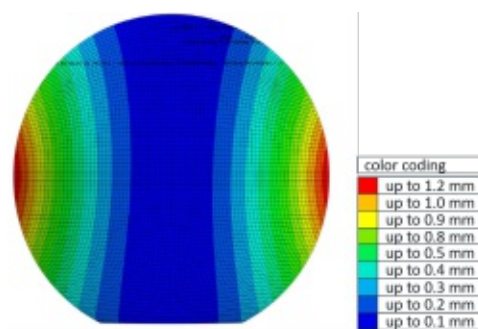
Figure 3.11: y-shift for the whole wafer for a symmetrically applied force. The boundary conditions include fix y-positions in the vertical middle of the wafer (y = 0 mm) and at both edges of the wafer (y = 1.2 mm).

The simulated bending line can be used as base for ray tracing simulations that are described in section 3.1.4. As the bending is directly proportional to the applied force, the bending for all applied forces can be calculated from the simulation of only one applied force.

3.1.4 Calculation of experimental parameters and simulation of the beam path

In the experiments at the BAM*line* the used detector consists of a CCD camera with a defined sensitive area. The point of impact of a beam reflected on the bent wafer on this

detector depends on different variables: The (horizontal) size of the beam, the bending radius, the energy of the photon, and the distance between wafer and detector. The size of the beam, the minimum and maximum energies and the sensitive area of the detector are given in the experiment. The bending of the wafer and the distance between wafer and detector can be adapted. For the experimental setup at the synchrotron it is crucial to know these parameters to make sure that all energies of interest are recorded in the sensitive area of the detector. The beam path is schematically shown in Figure 3.12.
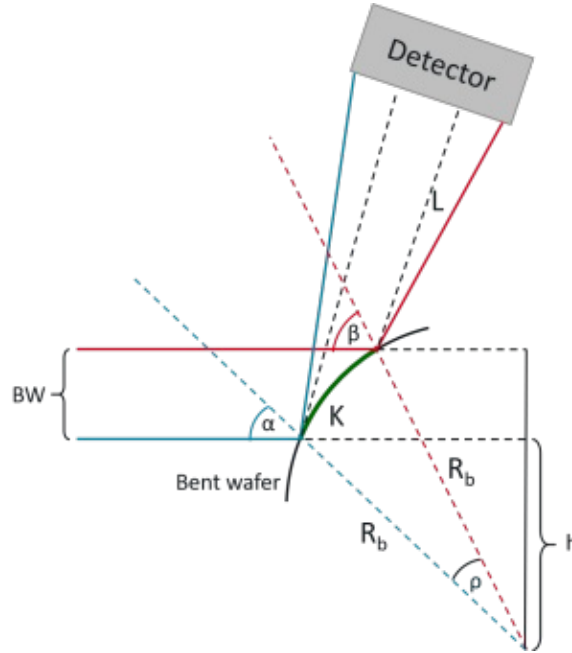
Figure 3.12: Schematic beam path, top view. The incoming parallel beam of width BW, coming from the left, is reflected on the wafer, illuminating the section K on the wafer surface. The reflection angle depends on the position in the beam, it is largest for the blue and smallest for the red ray. The dashed colored lines are perpendicular to the wafer surface.

The variable notations are summarized in table 3.1. In a first approximation it is assumed that the bending of the wafer follows a circle line with a constant bending radius R_b. From geometrical considerations it follows:

$$sin(\alpha) = \frac{h}{R_b}$$
$$sin(\beta) = \frac{h + BW}{R_b}$$
$$\Leftrightarrow sin(\beta) = sin(\alpha) + \frac{BW}{R_b}$$
$$\Rightarrow R_b = \frac{BW}{sin(\beta) - sin(\alpha)} \tag{3.11}$$

BW	beam width (given)
E_{min}, E_{max}	minimum and maximum energy (given)
$\theta_1 = \theta_{min}$	can be calculated from E_{max}
$\theta_2 = \theta_{max}$	can be calculated from E_{min}
$\theta_{av} = \frac{\theta_1 + \theta_2}{2}$	average angle between wafer and incoming beam
K	width of illuminated section of the wafer
L_0	smallest distance between illuminated area on the wafer and detector
F_{CCD}	width of the illuminated area on the detector (given)
R_b	bending radius of the wafer

Table 3.1: Names of the variables used in the calculation of the beam path

As $\alpha = 90° - \theta_2$ and $\beta = 90° - \theta_1$ the bending radius can be calculated from the beam width and E_{min} and E_{max}, *i.e.*, the desired energy bandwidth. The width of the illuminated area on the wafer is in the case of no bending:

$$K_p = \frac{BW}{sin(\theta_{av})} \tag{3.12}$$

In the case of the bent wafer K_b is:

$$K_b = R_b \cdot \rho$$
$$sin\left(\frac{\rho}{2}\right) = \frac{K_p}{2 \cdot R_b}$$
$$\Leftrightarrow \rho = 2 \cdot arcsin\left(\frac{\frac{BW}{sin(\theta_{av})}}{2 \cdot R_b}\right)$$
$$\Rightarrow K_b = R_b \cdot 2 \cdot arcsin\left(\frac{\frac{BW}{sin(\theta_{av})}}{2 \cdot R_b}\right) \tag{3.13}$$

For large bending radii with $BW/sin(\theta_{av}) \gg R_b$ it holds that $K_b \approx K_p$. The illuminated area on the CCD, F_{CCD}, is in the case of the flat wafer equal to the beam width. In the

case of the bent wafer, it is enlarged by $\Delta_1 + \Delta_2$ (see Figure 3.13):

$$
\begin{aligned}
F_{CCD} &= BW + \Delta_1 + \Delta_2 \\
&= BW + \left(L_0 + \frac{BW}{2 \cdot tan(\theta_{av})} \right) \cdot tan(\delta) + \left(L_0 - \frac{BW}{2 \cdot tan(\theta_{av})} \right) \cdot tan(\delta) \\
&= BW + 2 \cdot L_0 \cdot tan(\delta)
\end{aligned}
$$

$$
\text{with } \delta = \frac{\theta_2 - \theta_1}{2}
$$

$$
\Leftrightarrow L_0 = \frac{F_{CCD} - BW}{2 \cdot tan(\delta)} \tag{3.14}
$$

With equation 3.14 it is possible to determine the distance L_0 between the middle of the wafer and detector for a given beam width and energy range. For an experiment at the synchrotron it is necessary to first define the energy range of interest. This defines the angles θ_1 and θ_2, which can be used to calculate the angles θ_{av}, α, β, and δ. Then the beam width and the bending radius can be set according to equation 3.11 under consideration of the experimental possibilities concerning the beam width, and equation 3.12. As the wafer has a radius of 50 mm the illuminated area on the wafer can not be larger than 95 mm. From the sensitive area on the CCD the distance between wafer and crystal can be determined according to equation 3.14, taking into account the experimental possibilities. Exemplary values are shown in table 3.2. They can be used to prepare an experiment. It is possible to measure the same energy range using the whole width of the detector with different geometrical parameters, allowing to adapt the experiment to the actual requirements.

The goal is to predict the energy calibration, *i.e.*, the position on the detector for each reflected energy. Therefore, it is necessary to know the point on the wafer surface where this energy is reflected and the distance between this point and the detector. The situation is sketched in Figure 3.13. The position on the wafer is denoted as x ranging from 0 to K. The circle line (shown in Figure 3.14) is parameterized as:

$$
f(x) = y = \sqrt{R_b^2 - \left(\frac{K}{2} \right)} + \sqrt{R_b^2 - \left(x - \frac{K}{2} \right)^2} \tag{3.15}
$$

The angle in every point x on the wafer surface is given by the slope in this point, this is the first derivative:

$$
f'(x) = \frac{x - \frac{K}{2}}{\sqrt{R_b^2 - \left(\frac{K}{2} - x \right)}} = tan(\delta) \tag{3.16}
$$

	element: Fe K-edge (7112 eV)					
	XANES			**EXAFS**		
$E_{min}(eV)$	7100			7100		
$E_{max}(eV)$	7300			7800		
$\theta_{min}(°)$	15.714			14.683		
$\theta_{max}(°)$	16.168			16.138		
$\theta_{av}(°)$	15.941			15.426		
$F_{CCD}(mm)$	20					
$BW(mm)$	5	10	15	5	10	15
$K(mm)$	18.21	36.41	54.62	18.80	37.60	56.40
$R_b(mm)$	2295	4589	6883	725	1450	2175
$L_0(mm)$	1891	1260	630	579	386	193

Table 3.2: Exemplary values for experimental parameters. These are the values calculated as described in section 3.1.4. In the experiment, distances L are limited to approximately $1\,m$, the illuminated area on the wafer can not be larger than $K = 95\,mm$ and the minimum bending radius that was tried so far is approximately $625\,mm$.
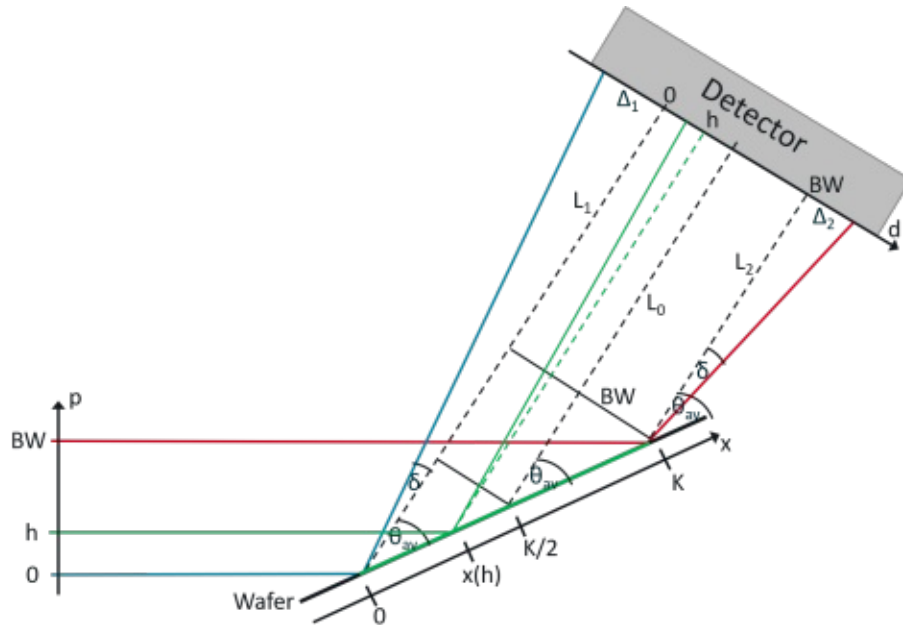
Figure 3.13: Position in the beam. A photon in the beam at position h hits the wafer at position $x(h)$. The angle at this position is defined from the bending of the wafer and the angle θ_{av}. If the angle corresponds to the Bragg angle of the photon, it is reflected and hits the detector in a defined point (see equation 3.21). In the case of a flat wafer, this position is h (dashed green line).

From equation 3.16 it is possible to calculate the position x on the wafer, where the angle (due to the bending) is equal to δ. In this point, the reflection angle for an incoming beam is equal to $\theta = \theta_{av} - \delta$.

$$tan(\delta) = \frac{x - \frac{K}{2}}{\sqrt{R_b^2 - \left(\frac{K}{2} - x\right)^2}}$$

$$\Leftrightarrow tan(\delta) \cdot \sqrt{R_b^2 - \left(\frac{K}{2} - x\right)^2} = x - \frac{K}{2}$$

$$\Rightarrow tan^2(\delta) \cdot \left(R_b^2 - \left(\frac{K}{2} - x\right)^2\right) = \left(x - \frac{K}{2}\right)^2$$

$$\Rightarrow \frac{R_b^2 \cdot tan^2(\delta)}{1 + tan^2(\delta)} = \left(x - \frac{K}{2}\right)^2$$

$$\Rightarrow R_b \cdot sin(\delta) = x - \frac{K}{2}$$

$$\Leftrightarrow x = R_b \cdot sin(\delta) + \frac{K}{2} \tag{3.17}$$

The position in the beam is denoted as p, ranging from 0 to BW. The relation between
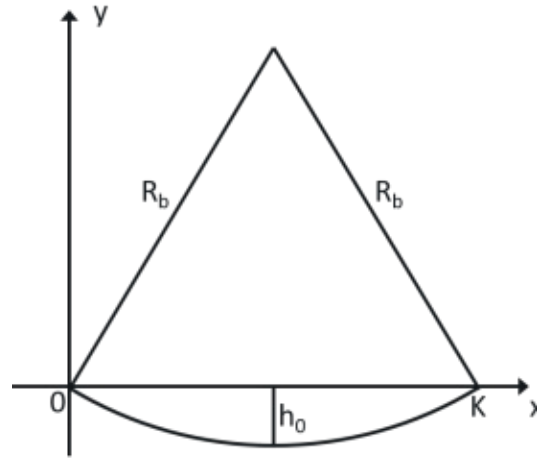
Figure 3.14: Circle line

x and p is:

$$p(x) = x \cdot sin(\theta_{av}) \tag{3.18}$$

Combining equations 3.17 and 3.18 yields for the position in the beam of a ray that is

reflected under an angle $\theta = \theta_{av} - \delta$:

$$p(\theta) = R_b \cdot sin(\theta_{av} - \theta) \cdot sin(\theta_{av}) + \frac{K}{2} \cdot sin(\theta_{av}) \qquad (3.19)$$

The position on the detector is denoted as d, ranging from $-\Delta_1$ to $BW + \Delta_2$. A ray at position $p = h$ in the beam reflected in point $x(h)$ on the planar wafer would hit the detector in the point $d = h$. For the bent wafer the position on the detector of a ray reflected in the point $x(h)$ is $d = h + L(h) \cdot tan(2\delta)$ with

$$L(h) = L_0 + K \cdot cos(\theta_{av}) - \frac{h}{tan(\theta_{av})} \qquad (3.20)$$

Putting all together:

$$d(\theta) = h + \left(L_0 + K \cdot cos\left(\theta_{av}\right) - \frac{h}{tan(\theta_{av})} \right) \cdot tan\left(2 \cdot (\theta_{av} - \theta) \right) \qquad (3.21)$$

Note that h is energy dependent since only photons with an energy corresponding to the Bragg angle in the point $x(h)$ can be reflected in this point. This equation contains only values that are given by the experiment or can be derived directly from given values. It allows to calculate the position of every energy on the detector for a given bending radius, beam width, average angle and distance between wafer and detector. All the above calculations were performed under the assumption of a circular bending line, but in principle it is possible to use other functions describing a bending line, such as a parabola or an approximated circle line. Therefore, equation 3.15 can be replaced by the mathematical representation of a parabola through the points $(0|0), (\frac{K}{2}| - h_0)$ and $(K|0)$ (see Figure 3.14):

$$f(x) = y = \frac{4 \cdot \left(R_b - \sqrt{R_b^2 - \left(\frac{K}{2}\right)^2} \right)}{K^2} \cdot \left(x^2 - Kx \right) \qquad (3.22)$$

or an approximated circle:

$$f(x) = y = \frac{1}{2R_b} \cdot \left(x^2 - Kx \right) \qquad (3.23)$$

The principle of the following calculations remains the same. Comparisons of the results for the position on the CCD between these three different models for a beam width of 6 mm, an illuminated area on the CCD of 25 mm for some different energy ranges (from 5900 eV to 6600 eV, from 7100 eV to 7800 eV, and from 8900 eV to 9600 eV) show that the difference is in the range of one µm or less and hence approximately 10 times smaller

than the pixel size of the detector.

Simulations of the beam path, *i.e.*, a simulated energy calibration, have been performed with a self-written program that is based on the above calculations. For the first simulations a circle line was assumed. The wafer with a defined bending at a defined position, the distance between wafer and detector, the beam width and the angles between beam, wafer and detector are given. Here, the bending is defined by a bending position h_0 (see Figure 3.14) that corresponds to the position of the bending motor and that can be calculated according to:

$$h_0 = R_b \cdot \left(1 - cos \left(\frac{100 \, \text{mm}}{2R_b} \right) \right) \tag{3.24}$$

The result of the simulation is the position of different energies on the CCD screen for the given parameters. A proof of consistence is that all desired energies hit the detector, when the distance between wafer and detector is calculated according to equation 3.14. Instead of using the circle line or another function for the bending, the values can also be taken from the simulation of the bending line described in section 3.1.3. A program based on these values yields slightly different results for the same input parameters, as shown in Figure 3.15. The energy range reflected by the wafer with the simulated

a) Circular bending line   **b)** Simulated bending line
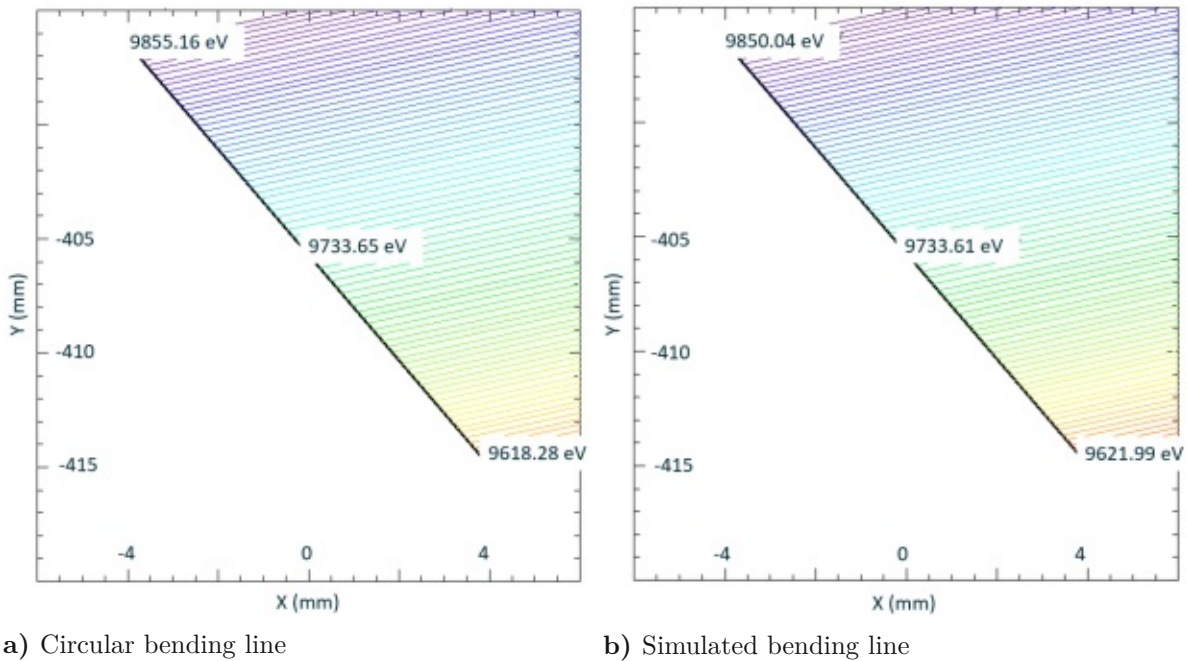
Figure 3.15: Simulated position on the CCD for different assumed bending lines but the same input parameters, corresponding to a Zn K-edge measurement.

bending line is smaller than the one simulated with the circle bending line and the same bending position h_0. This corresponds to a larger angle range in the illuminated area of

the wafer and is due to the deviation of the realistic bending line from a circle line. It shows the error that is made by assuming a circular bending in the calculation of h_0 (see equation 3.24). For further calculations and simulations this issue could be addressed by calculating the bending position directly from the angles θ_{min} and θ_{max} and the simulated bending line. Let us consider the following example: XANES measurements at the Fe-K edge with an energy range from $E_1 = 7.050\,\text{keV}$ to $E_2 = 7.200\,\text{keV}$. The corresponding angles are $\theta_1 = 16.286°$ and $\theta_2 = 15.938°$. These angles should represent the limits of the illuminated area on the crystal. For the bending position h_{s1}, which is the bending position $1\,\text{mm}$, the angles at points of the crystal surface near to the edges of the illuminated area are known from the simulation, and they are denoted as θ_{1s1} and θ_{2s1}. Since the applied force and bending of the crystal are proportional, the required bending position for the desired angles is:

$$h = \frac{\theta_1}{\theta_{1s1} \cdot h_{s1}} \quad \text{or} \quad h = \frac{\theta_2}{\theta_{2s1} \cdot h_{s1}} \tag{3.25}$$

As the wafer is symmetrically bent and the differences between the average angle and θ_1 and θ_2 is the same, there is no difference in determining h by taking the minimum or the maximum angle.

3.2 Experiments at the BAM*line*

All measurements were carried out at the BAM*line* at BESSY II, Helmholtz-Zentrum Berlin.

3.2.1 Beam source

There are two possibilities to generate the beam with the desired bandwidth. For XANES measurements the intrinsic bandwidth of the DMM is sufficient. The full width at half (FWHM) maximum for the multilayer reflex is calculated to be $dE/E \approx 1.7\%$. The energy range with intensity higher than 35% of the maximum intensity is a reasonable measure for the usable energy range. For example, in the case of measurements at the Fe-K edge ($7.112\,\text{keV}$) the FWHM is approximately $120\,\text{eV}$ and the usable energy range is approximately $150\,\text{eV}$ around the edge. This is a reasonable energy range for XANES measurements. This mode has the advantage that the photon flux is high, as the usable height of the beam is relatively large, due to the large angles of reflection, that are around four times larger than in the DMM total reflection mode. In addition, the flatfield is more homogeneous than in total reflection mode, because the reflexes of the multiple layers overlap.

The second possibility applied for EXAFS measurements is to use the DMM in total reflection ('mirror') mode in combination with a filter to obtain a bandpass. In this case, the beam is reflected under a much smaller angle and only in a thin layer of a few nm. The photon flux is reduced compared to the multilayer reflex and the flatfield is less homogeneous. The energy bandwith depends on the DMM angle and the chosen filter. Energy ranges for EXAFS measurements at K-lines of several transition metals as well as at L-lines of platinum group metals and rare earth elements are feasible in this way. Figure 3.16 shows an example calculation for such a bandpass. In this work measure-

centering
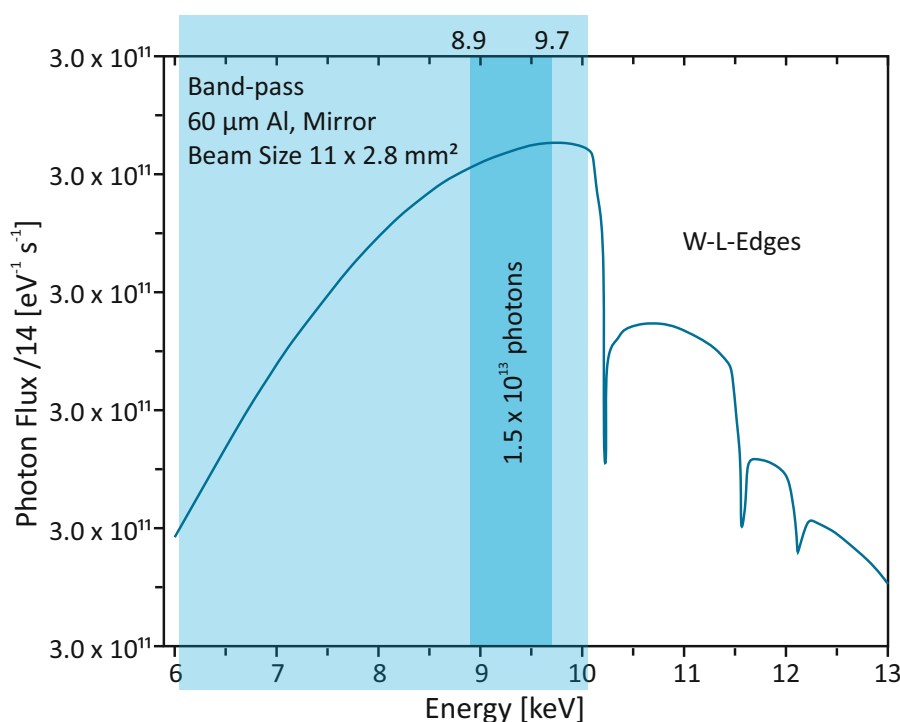
Figure 3.16: Calculated photon flux for a bandbass consisting of a combination of the DMM in mirror mode and a 60 μm Al filter.

ments at the Fe-K edge (7.112 keV), Cu-K edge (8.979 keV) and Zn-edge (9.669 keV) are shown. The experimental settings of the DMM for these examples are summarized in Table 3.3. The settings of the DMM for the bandpass were adopted from the standard XAFS measurements, where the DMM is set in total reflection mode at the required energy level to reject the higher harmonics. For every bandpass in this experiment the lower energy limit is due to the used filters and the upper one is due to the W-L lines from the material of the DMM.

Mode	Element	Parameters	Energy range
EXAFS (bandpass)	Cu	DMM@50 keV + 60 μm Al	7 - 10 keV
XANES (DMM@E_{edge})	Fe	DMM@7.112 keV	150 eV around the edge
	Cu	DMM@8.979 keV	190 eV around the edge
	Zn	DMM@9.7 keV	200 eV around the edge

Table 3.3: Summary of the DMM settings for the experiments shown in this work

3.2.2 Detector

The used detector consists of a CCD camera, pco.4000 manufactured by PCO AG (Kehlheim, Germany), a visible light optics system and a converter screen. The camera has 4008 x 2672 pixels with a size of 9 µm x 9 µm. The minimum exposure time is 5 µs. In combination with a Rodenstock objective (Qioptiq Photonic GmbH & Co. KG, Feldkirchen, Germany) with a focal distance of 100 mm, and a Nikon objective (Nikon Instruments Europe B.V., Amsterdam, Netherlands) with a focal distance of 180 mm, the pixel size of the recorded images corresponds to 4.8 µm × 4.8 µm. This allows a usable sensitive area of 19.46 mm × 12.83 mm. This setup has a high numerical aperture, and the pixel size can be adapted by exchanging the objectives. To convert the X-ray radiation into visible light, to which the camera is sensitive, a fluorescent screen (P43) from ProxiVision GmbH (Bensheim, Germany) is implemented in front of the first objective in a distance of approx. 5 mm. The bit depth n is 14 for the pco.4000 meaning that the camera records values between 0 and $2^{14}(= 16348)$ for the intensity pattern. This intensity pattern, corrected by a flatfield, is a direct measure of the absorption profile of the sample. For camera control, image acquisition and archiving of images, the software Camware is used. Images are saved in .tif format and processed with ImageJ software or with a self-written IDL® program.

3.2.3 Geometry of the setup

The wafer bender is placed on a rotating table DMT65-DM4-HSM and a linear table MTM60-10-HiSM, both from OWISGmbH (Staufen, Germany), to adjust the angle between the incoming beam and the crystal and the position in the beam. The adjustment is done remotely during operation. All this, depicted in Figure 3.17, is mounted on a frame, together with the detector at an adjustable distance, which in turn is fixed on another rotating table (Art312XM-HMC) from Aerotech GmbH (Fürth, Germany) allowing the $\theta - 2\theta$ geometry.
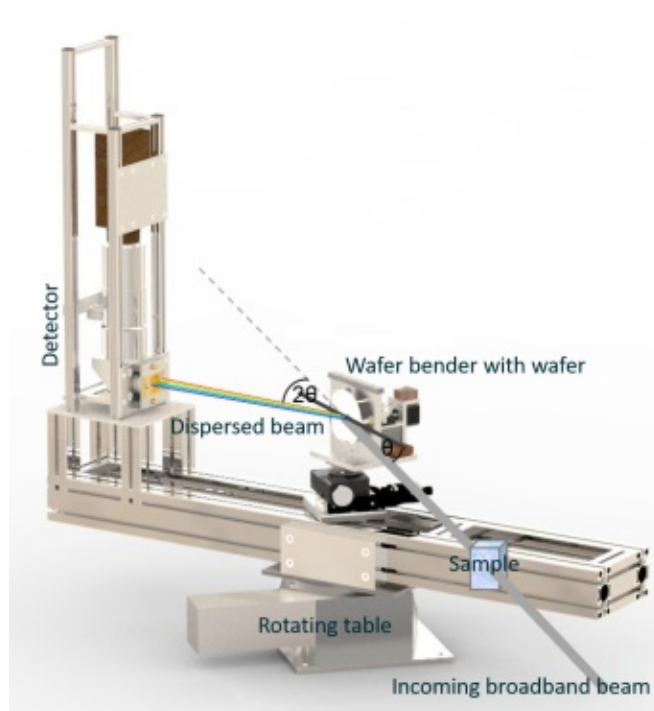
Figure 3.17: The new DXAFS setup

3.2.4 Data treatment

The measured data consists of grayscale images. Figure 3.18 (a) shows original data from the measurement of a Cu reference foil with an exposure time of 6 s. The vertical size (y-direction) of the illuminated stripe is determined by the vertical size of the incoming beam. Above and below the stripe, the detector image is cut because no relevant data is contained in this area, and to save memory space. The horizontal size (x-direction) corresponds to the size of the detector. As the bent wafer disperses the transmitted beam in the horizontal direction, the left side of the detector image corresponds to lower energy photons, and the right side of the detector image corresponds to higher energy photons. Bright areas mean high intensity of the transmitted beam as a consequence of low absorption in the sample, dark areas mean higher absorption. The stripy structure is caused by the multilayer structure. For every sample measurement a flatfield is also recorded with the same experimental parameters beam size, bending of the wafer bender, and DMM parameters. Figure 3.18 (b) shows a recorded flatfield. The flatfield image, or, if several flatfields are recorded, the average of the flatfield records, is divided by the sample image. The resulting image corresponds to the incoming intensity divided by the transmitted intensity, I_0/I. Afterwards, a region of interest is chosen, where the flatfield has a reasonable intensity over the whole width of the detector. This procedure is either performed manually in ImageJ or with a self-written IDL program, where the cutting
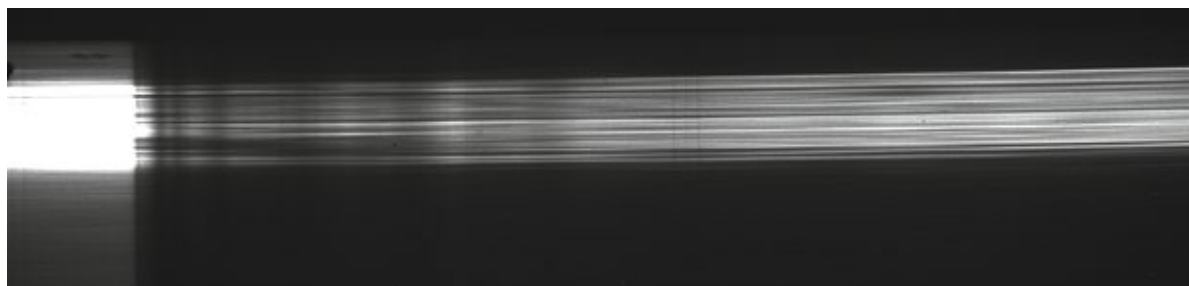
a) Absorption profile of a 12.5 μm thick Cu foil with an exposure time of 6 s.
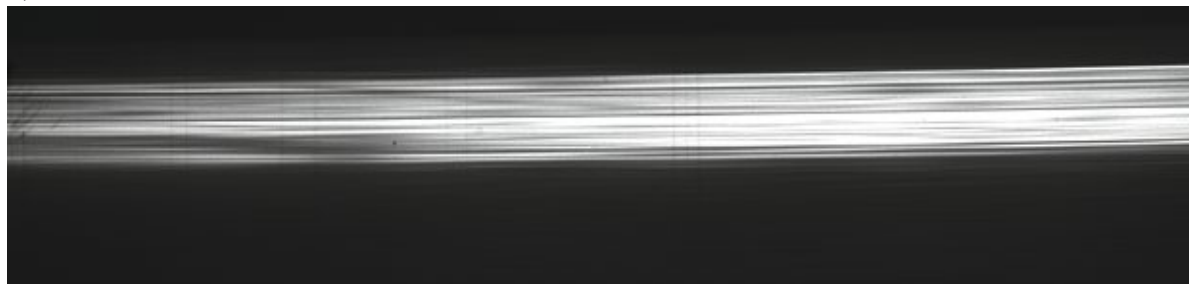
b) Flatfield measured with the same experimental parameters as the Cu foil.

Figure 3.18: Original DXAFS data. Top: 6 s measurement of a Cu reference foil. The whole width of the CCD is shown, but in the vertical dimension only a part of the recorded detector image is shown. Bottom: A picture of a flatfield measurement with the same experimental parameters as the Cu foil measurement.

region is chosen automatically from the intensity values of the flatfield. Therefore, the intensity values of the flatfield are summed up linewise (see plot on the right side of Figure 3.19), and all lines with a value above a predefined limit are considered for the further image processing. In Figure 3.19 this region of interest is marked with a red rectangle. In this region, a profile plot is performed for the flatfield corrected absorption
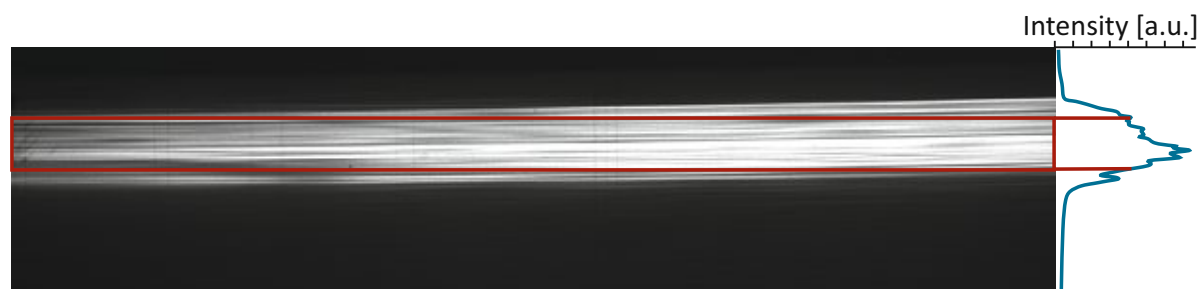
Figure 3.19: Choice of the region of interest. The plot on the right side shows the sums of the lines of the recorded flatfield image. The red rectangle marks the region of interest.

image. Therefore, all pixels of a column are summed up and this is done for the whole width of the image. In this manner, the sum of all intensity values at the same x-position in the region of interest is assigned to this x-position, that in turn corresponds to a well-

defined energy. This evaluation method is suitable only for homogeneous samples, as it sums up the absorption over the whole vertical sample cross section. Figure 3.20 shows the flatfield corrected and cropped image together with the profile plot. The next step is the transformation of the pixel values to energies. The energy calibration is described in more detail in section 3.3.

The further data processing is done in the XAFS spectroscopy data processing software Athena or in Origin.
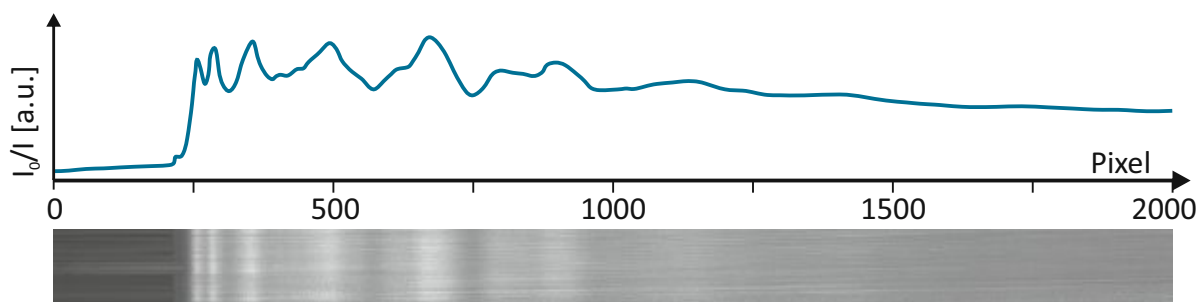
Figure 3.20: Cropped area of the recorded absorption of the Cu foil divided by the corresponding flatfield. The plot on top of the shown image shows the summed intensity values for every pixel in x-direction.

3.3 Results and discussion

3.3.1 Energy calibration

After the measurements, energy calibration is required. This is performed with the same experimental adjustments as the measurements. For this purpose, monochromatic X-rays are needed, and therefore the DMM is removed and the DCM is placed in the optical part of the beamline. Pictures are taken every 10 eV scanned by the DCM. Every energy is reflected only under the corresponding Bragg angle on the surface of the bent wafer, and hence the pictures of the monochromatic beams consist of lines on the CCD screen. As an example some of the recorded lines for the Fe-K XANES energy calibration are shown in Figure 3.21.

The inclination of the lines is due to the divergence of the incoming beam. The differences between the upper and lower end of the line are between 53 and 77 pixels or 3.7 eV and 4.8 eV (calculated after the calibration from the pixel difference). Taking the middle of every line, it is possible to assign a pixel in x direction to every energy and plot a calibration curve. This curve can be compared with a calibration curve obtained from the simulation (Figure 3.22 (c)) by calculating the intersections of the reflected beam of each energy with the screen of the detector. Both energy calibrations, the experimental

a) E = 7.08 keV

b) E = 7.10 keV

c) E = 7.12 keV

d) E = 7.14 keV

Figure 3.21: Monochromatic beams result in single lines on the CCD screen. For the energy calibration, several different energies are recorded.

and the one obtained from the simulation, are shown in Figure 3.22 (b). Simulation and experiment are in good agreement.

3.3.2 Energy resolution

The experimental calibration curve can be approximated by a straight line to get an idea of the limit of energy resolution due to the detector pixel size. For the shown calibration (Figure 3.22) the functional equation of the fit is:

$$E(px) = 7.17 \times 10^{-2}\,\mathrm{eV}/px + 7059.8\,\mathrm{eV} \tag{3.26}$$

The point spread function was investigated to determine the experimentally reachable resolution of the detector. Therefore, the beam was directly directed on the fluorescence screen with an energy of 10.23 keV and a 100 µm thick copper plate was placed directly in front of the fluorescence screen, so that half of the screen was covered. The image, recorded with an exposure time of 2 s, shows a sharp edge. The intensity of this image is plotted together with its derivative and a Gaussian fit in Figure 3.23. The standard deviation of the Gaussian fit is $\sigma = 2.29$ pixel, and the full width at half maximum (FWHM)
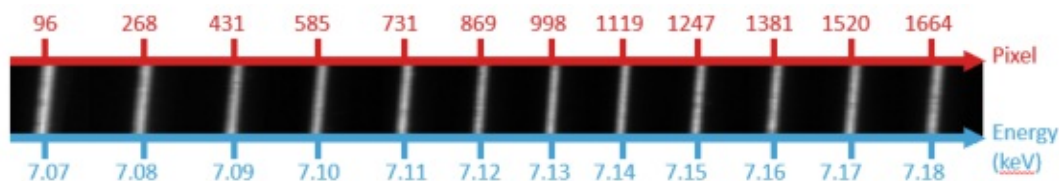
a) Experimental energy calibration
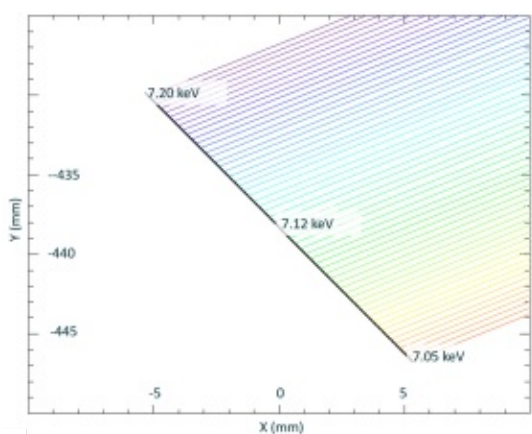
b) Simulated energy calibration
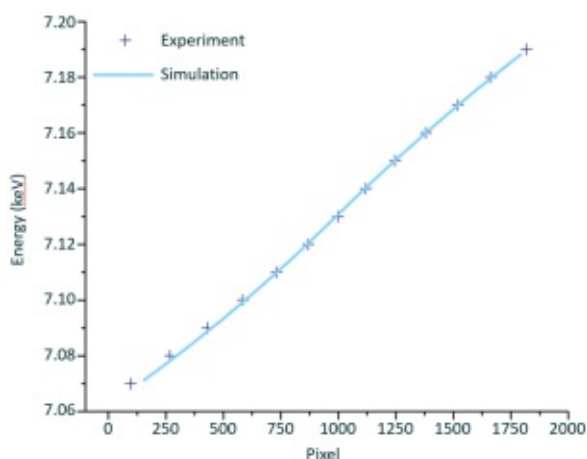
c) Experimental and simulated values

Figure 3.22: Energy calibration Fe-K edge XANES. (a) All images of the energy calibration taken together in one image. (b) Simulation of the beam path with the experimental parameters that were used for the measurement as described in section 3.1.4. (c) Calibration curve from the experiment and the simulation.
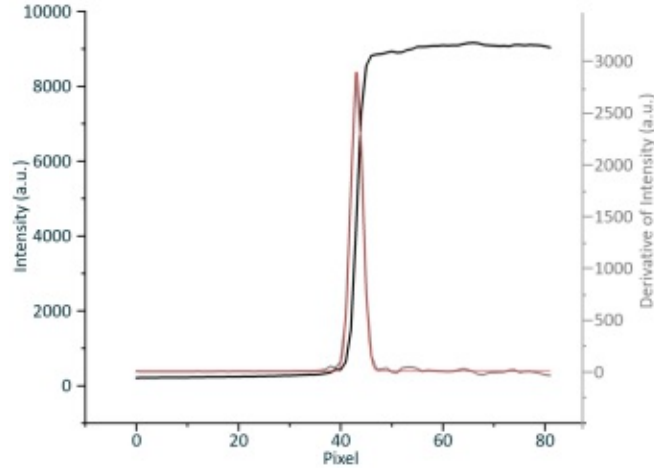
Figure 3.23: Point spread function. The intensity of the image of a sharp edge and its derivative is plotted. The derivative is fitted with a Gaussian function.

can be calculated as follows.

$$FWHM = 2\sqrt{2 \cdot ln2} \cdot \sigma = 5.4 \quad \text{pixel} \tag{3.27}$$

With this value the energy resolution r_E is

$$r_E = 5.4\text{pixel} \cdot 7.17 \times 10^{-2} \, \text{eV}/px \approx 0.4 \, \text{eV} \tag{3.28}$$

3.3.3 Reference foils

The first XANES measurements were performed on a Fe reference foil with a thickness of 10 µm and an exposure time of 10 s and a Cu reference foil with a thickness of 12.5 µm and an exposure time of 1 s. The foils are both from Goodfellow Cambridge Limited (Huntingdon, England). The experimental parameters for the wafer bender linear stage, the distance between detector screen and wafer, the average angle between wafer and beam as well as the energy adjustment of the DMM and the beam size are summarized in table 3.4. The results of the measurements together with the corresponding flatfield and conventionally measured spectra are shown in Figures 3.24 and 3.25.

The flatfields for the XANES measurements have approximately the form of a Gaussian, corresponding to the intrinsic bandwidth of the DMM. The flatfields have been chosen corresponding to their maximum being approximately at the position of the K edge. This leads to a good visibility of the post-edge features as the energy intensity of the flatfield is sufficient for this region. The setup allows the angle between incoming
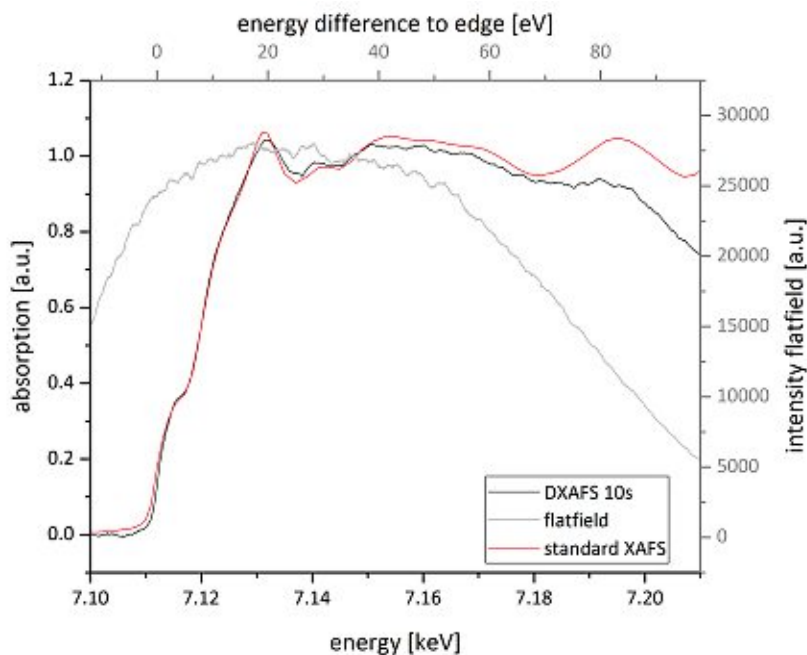
Figure 3.24: XANES measurement of 10 μm Fe foil with an exposure time of 10 s for the whole spectrum (DXAFS) and a total of 20 minutes acquisition time for standard XANES. The flatfield (gray line) is the limiting factor for the detectable energy range.
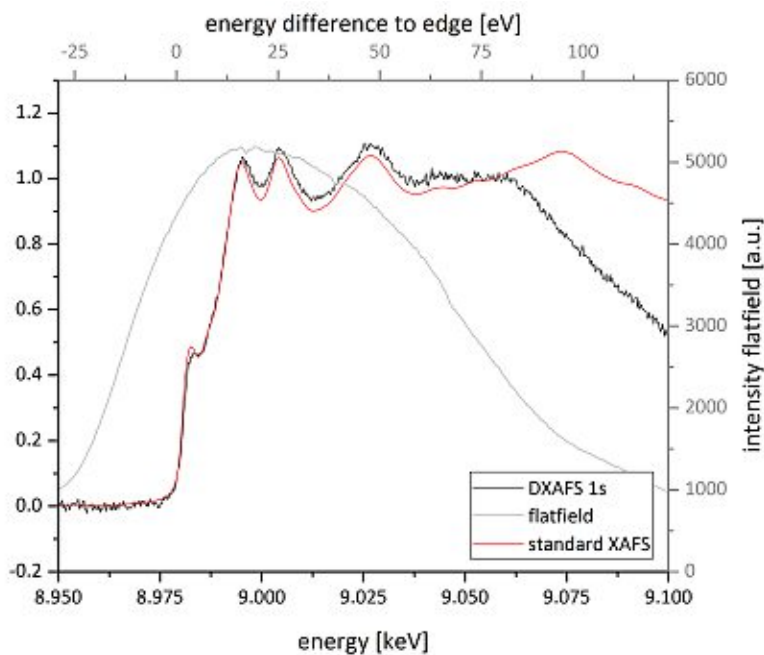
Figure 3.25: XANES measurement of 12.5 μm Cu foil with an exposure time of 1 s for the whole spectrum (DXAFS) compared to a standard XANES spectrum acquired in around 20 minutes. The gray line shows the flatfield.

measurement	h_0(mm)	L_0(mm)	$\theta_{av}(°)$	Energy	beam size (mm^2) vertical x horizontal
Fe foil XANES	0.12	≈ 200	15.77	DMM @ 7.15 keV	5 x 15
Cu foil XANES	0.5	≈ 640	13.26	DMM @ 9.039 keV	3 x 20
Cu foil EXAFS	1.25	≈ 520	12.07	DMM mirror @ 50 keV +60 µm Al	3 x 6
in situ Zn XANES	0.12	≈ 520	11.18	DMM @ 9.7 keV +60 µm Al	4 x 12

Table 3.4: Experimental parameters.

beam and wafer or detector to be adjusted independently from each other, and thus enables to optimize the image on the detector.

The experimental parameters for EXAFS measurements on Cu foil are listed in table 3.4. The chosen bending of the wafer in combination with the beam size leads to a broader reflected energy range than needed for the measurements. Therefore, there were more possibilities to optimize the image on the CCD screen by means of the two adjustable angles and the distance between wafer and camera. The best image was obtained at an angle $\theta_{av} = 12.07°$ and a camera angle of 24.8°. In Figure 3.26 (a) the EXAFS spectrum obtained in 6 s by DXAFS is shown, together with a conventionally measured EXAFS spectrum of the same foil (40 minutes for the whole spectrum). The wave functions in the k space and the Fourier-transformed data in the R space are depicted in Figures 3.26 (b) and (c).

3.3.4 Case study: early stages of ZIF-8 crystallization

As already stated, DXAFS spectroscopy allows to follow in situ reactions that take place on the second timescale. First tests of time-resolved measurements were performed to observe changes in the coordination of metal ions in solution as it is experienced during typical ZIF-8 synthesis. Therefore, Zn^{2+} in aqueous solution was mixed with aqueous 2-methylimidazole solution, leading to subsequent coordination of 2-methylimidazole to zinc ions, which occurs within seconds. During the whole reaction, a picture was taken every two seconds. The experimental parameters are listed in table 3.4. Again, the angle between incoming beam and camera deviated slightly from $2\theta_{av}$, the best images on the detector were obtained at a camera angle of 23.7°. The obtained spectra are shown in Figure 3.27. Zinc chloride shows a typical single peak spectrum that can be observed in this case in the beginning of the experiment. This has been associated with zinc ions that
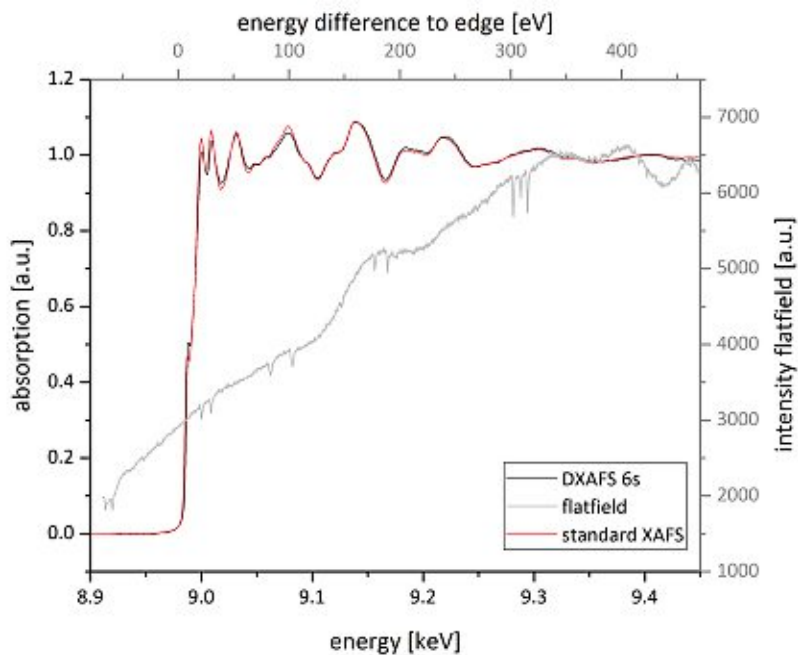
a) Cu EXAFS measurement
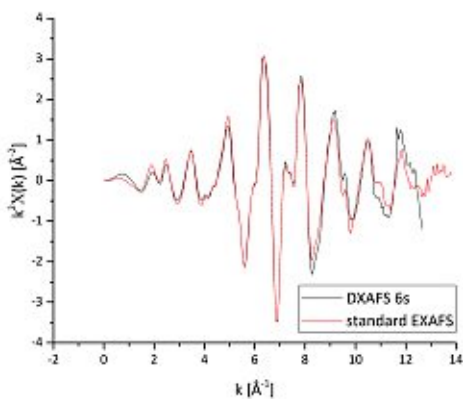
b) k space
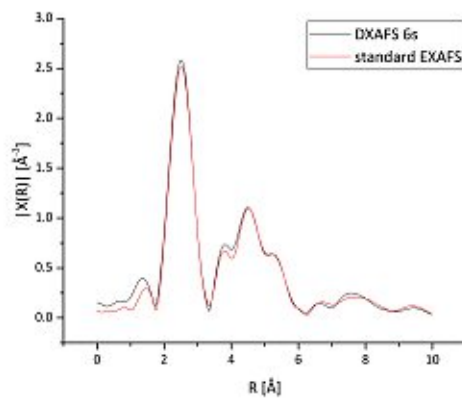
c) R space

Figure 3.26: EXAFS measurement of 12.5 µm Cu foil with an exposure time of 6 s by DX-AFS. (a) The spectrum is compared to a conventionally obtained one in 40 minutes. (b) Wave functions in the k space and (c) Fourier-transformed data in the R space.
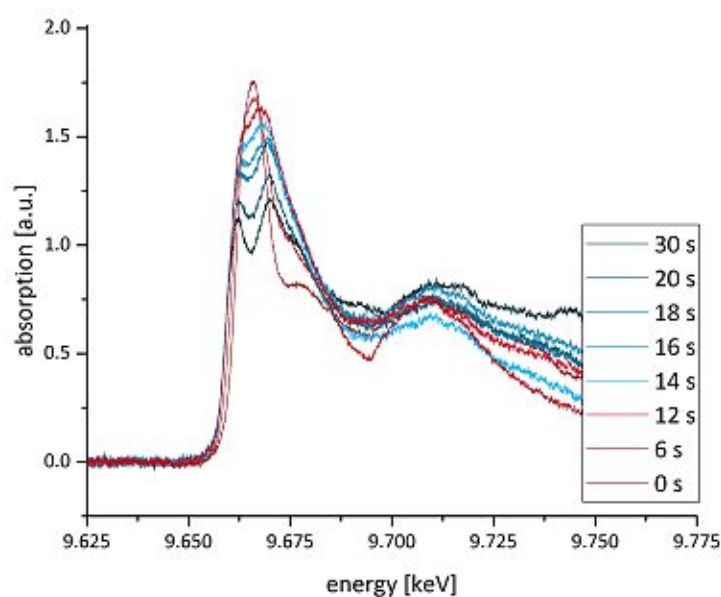
Figure 3.27: XANES measurement of aqueous $ZnCl_2$ solution that is mixed with aqueous 2-methylimidazole solution. Pictures are taken every 2 seconds.

are octahedrally coordinated by 6 water molecules within the first coordination sphere and two chloride anions within the second coordination sphere. Within 6 s, the spectrum changes and bears a resemblance to the spectrum of tetrakis(1-methylimidazole) $zinc^{2+}$ ions. The spectrum in the presented kinetic measurement further converts to tetrahedrally coordinated zinc(II)2-methylimidazolate (ZIF-8). The observed formation of an intermediate compound that resembles the spectra of tetrakis(1-methylimidazole)$zinc^{2+}$ ions and likely is tetrakis(2-methylimidazole)$^{2+}$ is in line with recently published pair distribution function (PDF) based results. More importantly, the presented measurements indicate that tetrakis(1-methylimidazole)$zinc^{2+}$ is a stable and chemically very similar surrogate to tetrakis(2-methylimidazole)$^{2+}$ which only forms transiently during early stages of ZIF-8 crystallization.

3.4 Conclusions

A new setup for reproducible time-resolved XANES and EXAFS measurements has been tested and implemented successfully. With the newly developed bent wafer setup it is possible to record a whole XANES or EXAFS spectrum in a single shot, in a scanning-less way. The beam path has been calculated theoretically and has been simulated for different sets of parameters. The experimentally found energy calibration is in good

agreement with the simulations. First tests with metal foils have been performed. The Si wafer as a dispersive element enables a completely scanning-free measurement of the spectra which are recorded by a CCD camera. The wafer bender mechanism and the rotating tables allow a simple and reproducible adjustment of the bending radius and the reflecting angles for different energy ranges. The parameters for different probing elements can be optimized and adapted to address questions in materials science such as in studies that address early crystallization stages of ZIF-8. Here, the combination of DXAFS- and classical XAFS spectroscopy has revealed the chemical similarity between stable tetrakis(1-methylimidazole)zinc^{2+} and tetrakis(2-methylimidazole)$^{2+}$ that only forms as an elusive intermediate during ZIF-8 synthesis. This finding provides further opportunities for studying the coordination chemistry of ZIF-8 during its formation.

The vertical width of the beam can be used for the spatial resolution, *e.g.*, for layered samples. Simulations of the wafer bending have shown that the bending curve is directly proportional to the applied force and in vertical direction quasi homogeneous in an area of around half a centimeter above and below the middle. This allows the theoretical calculation of the bending curve of the wafer for arbitrary applied forces from a single simulation. The results from these simulations can be used to calculate the experimental parameters. A simulation of the beam path can help to optimize these parameters and to adapt them to the actual experiment.

One aim for the future is to get the energy calibration curve directly from the simulation instead of measuring it for every single adjustment. The first comparisons between simulation and experiment show promising results. Future applications will be XANES and/or EXAFS measurements during chemical reactions for in situ monitoring of structural changes as demonstrated here for prototypical metal organic framework ZIF-8. This also includes the use of lateral resolution using the vertical width of the beam, *e.g.*, to track gradients of oxidation states, *e.g.*, in catalyst materials.

4 X-ray Fluorescence Imaging with Coded Apertures

X-ray imaging methods are used in many fields of research, as they allow a non-destructive investigation of the elemental content of various samples. As for every imaging method, for X-ray imaging the optics are of crucial importance. However, these optics can be very expensive and laborious to build, as the requirements on surface roughness and precision are extremely high. Angles of reflection and refraction are often in the range of a few mrad, making a compact design hard to achieve. One simpler and less expensive possibility of imaging high energy radiation is coded aperture imaging (CAI), a technique well established in astrophysics and also used in nuclear medicine or radiation detection, *e.g.*, for nuclear decommissioning. This method can be adapted to full field X-ray fluorescence imaging. In CAI, an object is projected through a known mask, the coded aperture, onto an area sensitive detector. The resulting image consists of overlapping projections of the object, and a reconstruction step is necessary to obtain the information from the recorded image.

In this chapter, theoretical considerations and preliminary simulations of image formation through a coded aperture are presented, and four different reconstruction methods are proposed. Different masks are tested in simulations. It turned out that the most commonly used reconstruction method, which is based on the convolution of the detected image with a decoding mask, does not produce satisfactory results in all cases, especially for small distances between object, mask and detector. Hence, other reconstruction methods were developed, one based on an iterative algebraic optimization, one based on an evolutionary algorithm and another one based on a neural network. All of them show good performance even in those cases where the convolution method fails.

For the experiments fluorescence images of different samples are recorded with an energy-dispersive 2D detector (pnCCD) and reconstructed with different reconstruction methods. With a small coded aperture with 12 holes the count rate could be significantly increased compared to measurements with a straight polycapillary optic. These results demonstrate that X-ray fluorescence imaging with coded apertures has the potential to deliver good results without scanning and with an improved count rate, so that measurement times can be shortened compared to established methods.

4.1 Introduction

4.1.1 Coded aperture imaging

X-ray imaging is a powerful tool for the characterization of materials; this includes spatial resolved elemental distributions, chemical states, and textural properties[56]. Fields of application are astrophysics[57], medical physics[58], characterization of biological[59] and environmental samples[56] or catalyst materials[60].

There are two possibilities to obtain 2D X-ray fluorescence images, scanning or full field methods.

In scanning methods, a micro X-ray beam is used to excite the fluorescence in the sample and the spectrum can be recorded with an energy dispersive detector. To get a 2D image, the sample is moved and the measurement repeated for every point in the area of interest. Depending on the required statistics, resolution and size of the sample area to be investigated, this kind of measurement can take several hours. For example, if a picture of 264 x 264 pixel is acquired with a measurement time of 1 s for every pixel (including movement of the sample and signal processing), this would take more than 19 hours.

In full field methods, the whole sample area to be measured is illuminated with a sheet beam. The produced fluorescence is detected by a 2D detector. If this detector is energy dispersive, the distribution of the characteristic radiation of different elements can be found in a single measurement. Otherwise, the excitation energy can be increased stepwise to excite one element after the other. In any case, suitable optics are needed to obtain an image.

In the case of X-rays these optics have to fulfill high requirements in terms of precision and roughness of the surface, and can be very expensive[61–63]. Probably the simplest way to image X-rays is the projection through a pinhole that acts as a so called *camera obscura*. The object is projected through a pinhole and an inversed projection can be recorded by a 2D detector. The magnification, field of view (FOV) and resolution depends on the distances between object, pinhole and detector. Furthermore, the resolution gets worse the larger the pinhole is. The drawback of this method is its low photon throughput. When using larger pinholes the throughput can be augmented, but this would worsen the resolution in turn. To overcome this issue, in the 1960s Dicke[64] and Ables[65] proposed to use a multi pinhole camera for astronomical applications. The principle is very simple: Many pinholes arranged in a known pattern act as coded aperture. Each hole allows the projection of the investigated object onto a position sensitive detector. These projections overlap on the detector screen. But as the pinhole pattern is known the original object can be reconstructed. As in the single pinhole case, the

resolution is defined by the size of the pinhole, the size of the detector pixels and the distances between object and aperture, d_1, and aperture and detector d_2. Since the 1960s, progress have been made concerning the development of mask patterns, computing power and detector technology, causing growing interest in CAI in X- and gamma-ray applications, for example in astrophysics[66], medical physics[58], neutron imaging[67], and X-ray fluorescence imaging[68,69]. Another possibility to make use of the advantages of coded apertures is X-ray projection imaging, where the internal microstructure of polycapillary optics can be used as the coded aperture, and it has been described that the resolution can be further enhanced by using a periodic grid placed on the output surface of the polycapillary optic[70,71].

The advantages of the CAI are its simplicity and the possibility of high angular acceptance of X-rays, depending on the experimental arrangement. Furthermore, coded aperture optics are achromatic and an arbitrary magnification can be obtained by choosing the ratio of d_1 and d_2. In contrary, other X-ray optics like polycapillary optics have a fix magnification and the transmittance is energy dependent. As already mentioned, compared to scanning methods the measurement time can be reduced considerably.

The principle of the X-ray fluorescence imaging with coded apertures has already been described in[68,69]. The sample is irradiated with X-rays of an energy that depends on the elements that shall be investigated. The sample fluoresces and the fluorescent X-rays pass through the mask onto the detector (see Figure 4.1 b).

However, as the detected image consists of overlapping projections of the object, a reconstruction step is necessary. Different reconstruction algorithms have been proposed and discussed[72]. One common method of image reconstruction is the convolution with an antimask, also called deconvolution method, that can be calculated from the coding mask. Furthermore, the reconstruction with iterative, algebraic or evolutionary algorithms or with neural networks is also possible. These techniques are often used in the field of computed tomography (CT)[73–76]. They are also applicable to X-ray fluorescence imaging with coded apertures, but up to now these possibilities have not been sufficiently investigated.

In the experiments, an energy dispersive pnCCD[77] (see section 3.2.2) was used. In every pixel of the pnCCD a whole spectrum is recorded. Hence, the element to investigate can be chosen by evaluating only the corresponding energy range in the spectrum. This allows mapping the elemental distribution of the sample in a single measurement for all excited elements. Normally, the pnCCD is operated with a polycapillary optic (Figure 4.2 a)), which enables a spatial resolution of a few µm, using the subpixel feature and magnifying optics[78]. However, the solid angle of the detector is limited by this arrangement, and hence also the count rate. With a coded aperture with N holes the transmission of photons can be significantly increased (Figure 4.2 b)), to get a better
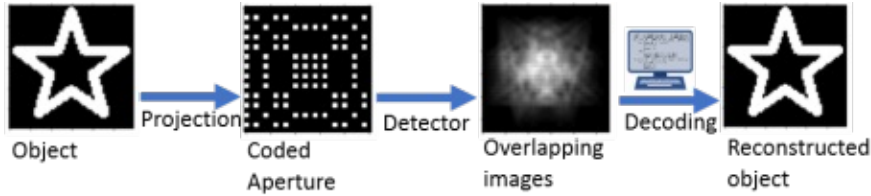
a) The principle of coded aperture imaging. An object is projected through a coded aperture with a known arrangement of holes. This yields many overlapping pictures on a position sensitive detector. The object can be reconstructed with a decoding procedure.
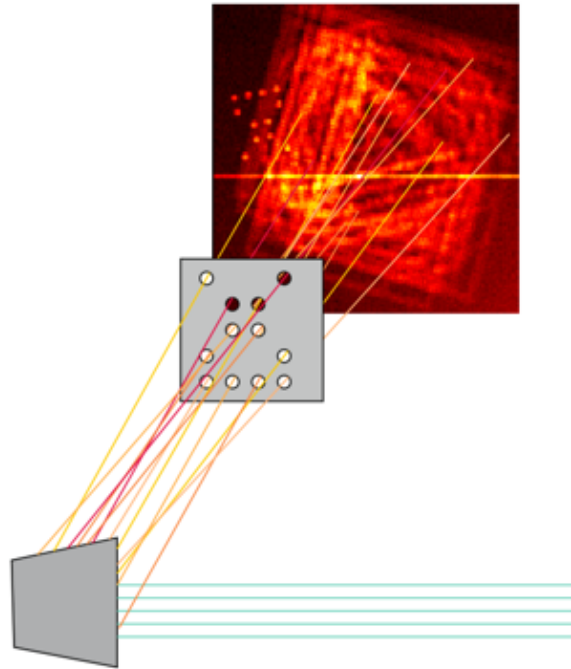
b) In the case of fluorescence imaging, the object is the irradiated sample and the fluorescent X-rays pass through the mask.

Figure 4.1: Principle of X-ray fluorescence imaging with coded apertures.

illumination to fully exploit the possibilities of the pnCCD and to get a better signal to noise ratio. In the next sections, some theoretical considerations and simulations that

a) Straight polycapillary optic

b) Coded aperture
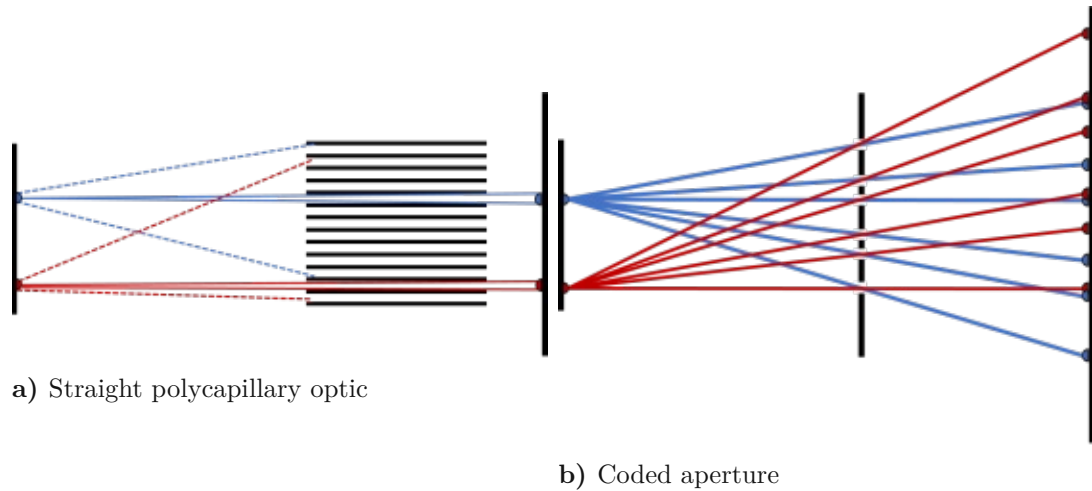
Figure 4.2: Principle of different optics for full field imaging. a) A straight polycapillary optic. The angular acceptance of every single capillary is rather small. This limits the throughput of photons. b) A multiple pinhole mask. The photon throughput is multiplied with the number of holes compared to a single pinhole.

have been performed to prepare the experimental applications of CAI with fluorescent X-rays are presented. The choice of a mask pattern, and a new method to construct an antimask for decoding with the deconvolution method in the case of near field imaging are described, as well as three new adapted reconstruction methods that do not involve an antimask. This is the basis for the development of a scanless X-ray fluorescence imaging method with the pnCCD detector. First measurements with the coded aperture and the reconstruction of different test objects with different reconstruction methods are presented.

4.1.2 Geometrical considerations

Field of view

The field of view (FOV) of an experimental setup with coded apertures can be calculated from the size of the mask, M, the size of the detector, D, and the distances d_1 and d_2 between object and mask and mask and detector respectively (see Figure 4.5).

$$pcFOV = \frac{D \cdot d_1 - M \cdot (d_1 + d_2)}{d_2} \tag{4.1}$$
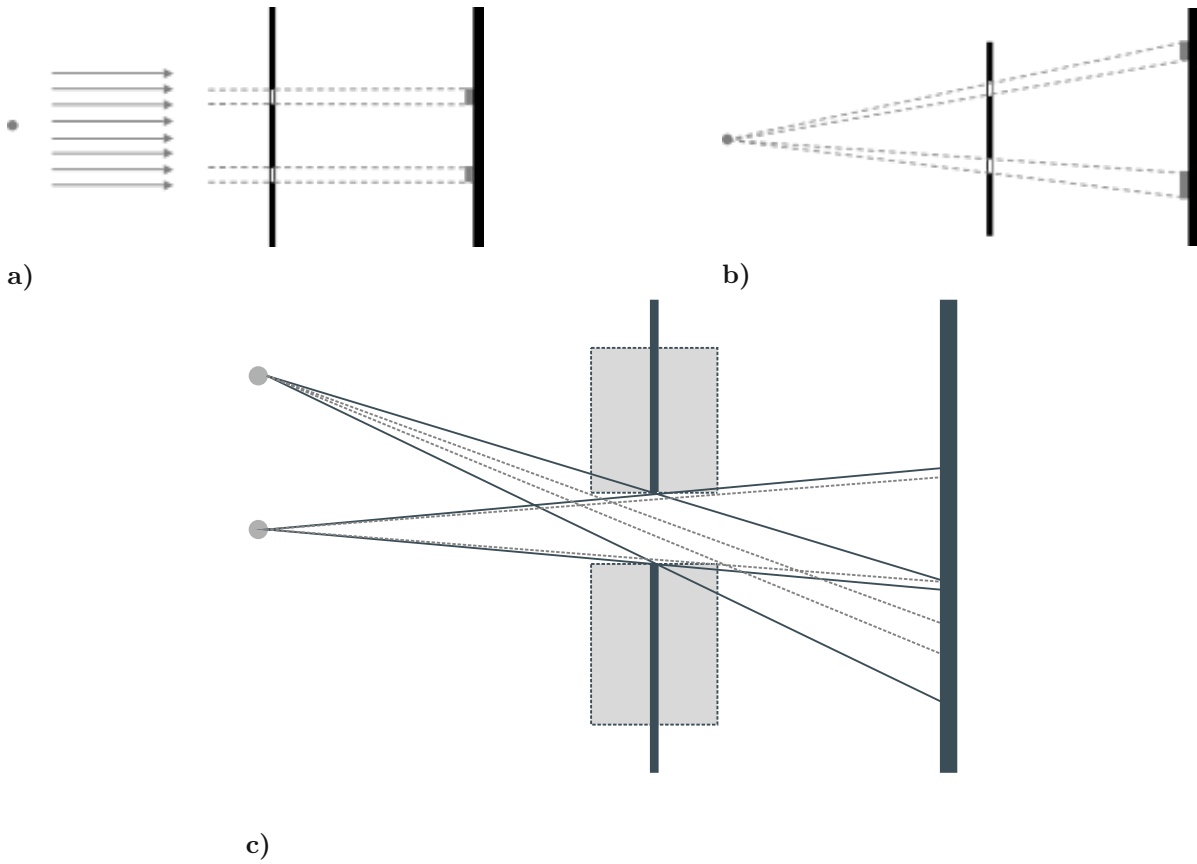
Figure 4.3: a) In the case of far field imaging (like in astrophysics), light coming from a distant point source can be assumed to be parallel and casts a shadow of the mask onto the detector. b) In the near field, this assumption holds no longer. One must consider the scaling. c) When the distances between object, mask and detector are small, the mask thickness plays an important role, because it comes to collimation effects. Sources that are located off the optical axis (point above) are detected much weaker (or not at all) through a thick mask (gray mask and dashed lines) than through a thin mask (black mask and solid lines).
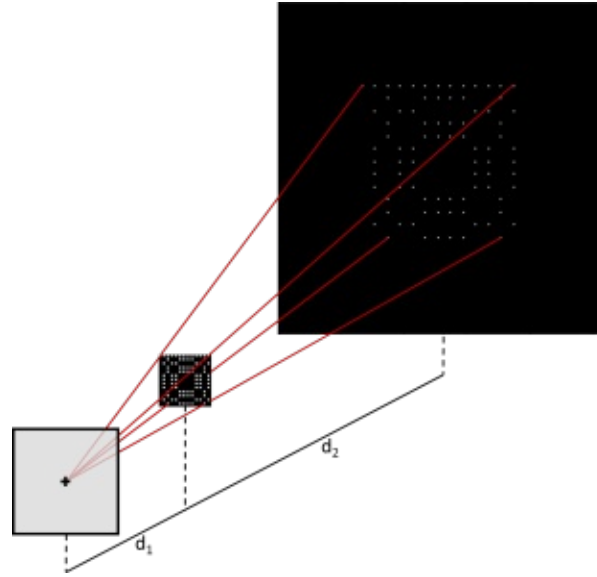
Figure 4.4: The scaling of the mask. A point in the middle of the object plane is raytraced through the middle of each hole of the mask onto the detector. The shape or size of the holes is irrelevant. The scaled mask is used to construct the antimask.

$$fcFOV = \frac{D \cdot d_1 + M \cdot (d_1 + d_2)}{d_2} \tag{4.2}$$

The fully coded (fc) and partially coded (pc) FOV must be distinguished. The pcFOV
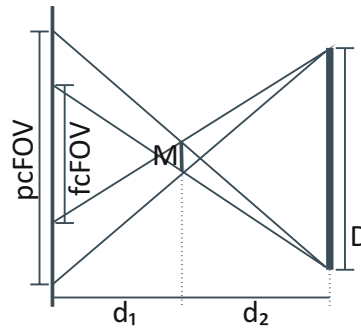
Figure 4.5: Field of view. For given distances d_1 and d_2 and given mask (M) and detector (D) sizes, the field of view (FOV) can be calculated. The partially coded (pc) FOV is the region from which photons can reach the detector. The fully coded (fc) FOV is the region from which all photons falling through the mask hit the detector.

is the entire region in the object plane from which photons can fall through the mask onto the detector, but not necessarily through all holes of the mask. The fcFOV is the region from which outgoing photons will fall onto the detector through all holes of the mask, projecting a full mask pattern onto the detector. For our case, where detector and mask are square, Equations 4.1 and 4.2 hold for the length and the height of the

FOV. In case the detector and the mask dimensions are not square, one has to calculate the length and height of the FOV separately. The above equations are the maximum pcFOV and minimum fcFOV for a mask of size M, in the case that all of the mask area contains holes. To get the actual FOV the maximum distance between two holes in the dimension under consideration must be used.

This means that in the pcFOV simulations the object tends to be calculated as too large, *i.e.*, the edge pixels of the object do not contribute to the projection function. This has to be considered in the reconstruction. In fcFOV simulations the object size tends to be underestimated, but in any case all photons from this area that fall through the mask will also hit the detector.

Resolution

The resolution of the system depends mostly on the distances d_1 and d_2 and the size of the holes in the mask. From geometrical considerations (see Figure 4.6) it follows that the size of one point in the object plane that is projected through a hole of diameter h has the size H_D in the detector plane:

$$H_D = h \cdot \frac{d_1 + d_2}{d_1} \tag{4.3}$$

Since it is not the projected image but the reconstructed object that is the result of the measurement, the entire system's resolution is described by the backprojection of H_D to the object plane:

$$H_O = 2 \cdot h \cdot \frac{d_1 + d_2}{d_2} \tag{4.4}$$

Equation 4.4 is the theoretical resolution of a system with one hole. Here, the size of
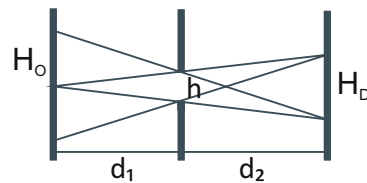
Figure 4.6: Considerations to the resolution of the coded aperture imaging system

the detector pixels is not considered. The pixel size of the used pnCCD camera is $48\,\mu\text{m}$, and in principle a subpixel algorithm can be used to refine the pixel size down to below $10\,\mu\text{m}$ [79]. As the minimum mask hole size used for this work is $50\,\mu\text{m}$ this will be the limiting factor in the resolution.

Using more than one pinhole can enhance the resolution through the method of multiframe super-resolution, described for example by Buchriegler et al.[80]. This method is based on the addition of a number of images shifted by a fraction of the detector pixel size. Depending on the geometrical arrangement and the distance between the holes in the mask, one point in the object plane is projected onto the detector at different positions, and the shifts are usually non-integer multiples with different values ranging from 0 to 1 of the detector pixel size. Thus the influence of the detector pixel size can be further reduced in the case of CAI and the resolution is mostly determined by the mask hole size.

In comparison, when the pnCCD is operated with a straight polycapillary optics, the spatial resolution is determined by the detector pixel size if the channel diameter is not larger than this size. The divergence of the beam can be kept very small, when the distances between sample, optics and detector are kept small. Ideally, the spot size from individual channels of the polycapillary on the detector approximately equals the pixel size of 48 µm. This resolution could be reached with a coded aperture with holes with a diameter of 12 µm when the distances d_1 and d_2 are equal.

4.1.3 Mask pattern

The choice of the mask pattern should be taken carefully in CAI. The first suggestion was to use randomly distributed pinholes, but in the following decades many more mask patterns have been proposed. This includes Fresnel Zone Plates[81], geometric patterns[82,83], patterns based on pseudo random products and non[84]- or uniformly redundant arrays[85].

In the consideration about the mask pattern the reconstruction method plays a crucial role. When using a mathematical deconvolution method for image reconstruction, it is preferable to use a design in which the autocorrelation function of the pattern has a central peak and flat sidelobes. This allows a reliable reconstruction without ghost images. Another desirable property of a mask used for CAI is the high open fraction, that is the ratio of the transparent area to the whole area of the mask.

The mask pattern used for the here described experiments is a no-two-holes-touching (NTHT) modified uniformly redundant array (MURA) based pattern. A rectangular MURA, which is the basis of our pattern, has been proposed for CAI in astronomy by

Gottesman and Fenimore[85] and is built after the following rules:

$$M(x, y) = \begin{cases} 0 & \text{if } x = 0 \\ 1 & \text{if } y = 0 \text{ and } x \neq 0 \\ 1 & \text{if x and y are quadratic residues mod L} \\ 1 & \text{if x and y are not quadratic residues mod L} \\ 0 & \text{otherwise} \end{cases} \quad (4.5)$$

x and y are the indices of the rows and columns of the MURA array. A zero means an opaque mask element (material), a one is a transparent mask element (hole). A MURA sequence can be built in any length L with L being prime and $L = 4 \cdot m + 1$, where m is an integer. L is called the rank of the MURA. It has been reported[86] that this type of mask has good imaging and reconstruction properties and a large open area of 0.5, meaning that half of the area of the mask is transparent for X-rays.

For simulations, an inverted MURA with exchanged zeros and ones in the building equation 4.5 was also investigated, because it turned out to be suitable for the construction of the antimask in all investigated geometrical arrangements, as is described in section 4.1.5.

To get a self-supporting mask, a column of zeros is inserted between every two columns and a line of zeros is inserted between every two lines of the original pattern, this yields a NTHT mask. This reduces the open area of the mask to 0.125 in the case when the spacing between the holes has the same size as the holes themselves and the holes are squared. An example of a MURA of rank 29, the corresponding inverted MURA and its NTHT version are shown in Fig. 4.7.
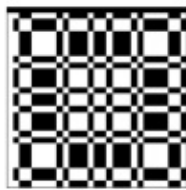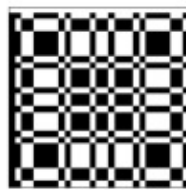
a) MURA with $L = 29$ b) Inverted MURA   c) NTHT inverse MURA
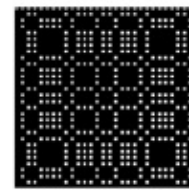
Figure 4.7: MURA and MURA based mask patterns

In astrophysics, often a mask pattern is used that consists of a periodical arrangement of the single mask. This is done to get a larger fully coded field of view, that is the area of the projected object that casts a full cycle of the mask pattern onto the detector.

Haboub *et al.*[69] also proposed a replication and tiling of their basic mask pattern to construct the antimask, in the field of fluorescent X-rays, while using a single mask for the projection.

The comparison of simulations of imaging and reconstruction with the deconvolution method with an antimask built from the single mask and the reconstruction with an antimask built from a pattern of 3 x 3 basis masks, as proposed by Haboub *et al.*[69], showed good results with both types of antimasks for a large range of geometrical arrangements. Replication and tiling were not necessary for the construction of the antimask.

4.1.4 Projection function

As preparatory work for experiments, simulations were carried out. First, a raytracing program was developed in Python to simulate the image formation with coded apertures. The parameters to be set allow accurate reproduction of the experimental conditions. This involves the distances d_1 and d_2, the detector length and the detector pixel size as well as the mask length, hole size, thickness and rotation relative to the detector.

The thickness of the mask is an important parameter that must not be neglected if it is in the same range as the hole size. The angular acceptance is considerably reduced compared to an infinitely thin mask and this leads to a collimation effect (see Figure 4.3 c)).

It is assumed that a ray comes from the middle of an object pixel, completely fills a mask hole and can hit, depending on the geometry, several detector pixels. In the raytracing simulation, the intensity deposited in each detector pixel is proportional to the percentage of the area hit. So, if the whole detector pixel is illuminated, an intensity value equal to the object pixel intensity is added to the actual intensity value, if only half of the detector pixel is illuminated, half of the object pixel intensity value is added, and so on. Every object pixel can contribute to the intensity in several detector pixels. The result of the raytracing simulation is a matrix which contains the contribution of each object pixel to each detector pixel (or, the other way round, stores the information which object pixels contribute to every detector pixel).

As the size of the FOV is defined by Equation 4.1 or 4.2, the object size is also defined but the object pixel size can be chosen. Hereby, it is possible to consider the partially coded or fully coded FOV. This defines the number of pixels of the object and the resolution of the reconstructed image. Limits are set by the physical resolution, which is determined mostly by the hole size of the mask, and the available computer memory. For example, 264 x 264 detector pixels and 264 x 264 object pixels result in a 69696 x 69696 projection matrix, which can be a memory problem when working with dense matrices and a normal laptop. The use of sparse matrices is very useful in terms of memory.

Once the projection function calculated the raytracing process reduces to one single matrix multiplication.

The projection function for one fix experimental setup describes how an arbitrary object is projected through the mask onto the detector. This projection function can be used to simulate the measurements and it is necessary to know the projection function of the system for the reconstruction with the iterative and evolutionary algorithm.

4.1.5 Reconstruction methods

Reconstruction with antimask (deconvolution)

The reconstruction of the recorded images can be performed with an antimask. To derive the construction of the antimask, the following case without noise is considered: The image formation process can be described as

$$I(x,y) = O(x,y) * M(x,y) \tag{4.6}$$

where $I(x,y)$ is the image obtained by projecting the object $O(x,y)$ through the mask $M(x,y)$. $*$ is the convolution operator. The reconstructed object $O'(x,y)$ is the convolution of the image and an appropriate antimask $AM(x,y)$.

$$\begin{aligned} O'(x,y) &= I(x,y) * AM(x,y) \\ &= O(x,y) * M(x,y) * AM(x,y) \end{aligned} \tag{4.7}$$

The convolution becomes a simple multiplication in the Fourier space:

$$FT\left(O'(x,y)\right) = FT\left(O(x,y)\right) \cdot FT\left(M(x,y)\right) \cdot FT\left(AM(x,y)\right) \tag{4.8}$$

Consequently, the object is perfectly reconstructed, when the product of the Fourier transforms of the mask and the antimask is the delta function. Thus, the antimask can be derived from the used mask:

$$AM(x,y) = FT^{-1}\left(\frac{1}{FT\left(M(x,y)\right)}\right) \tag{4.9}$$

As shown, the imaging process can be described as a convolution. Therefore, the reconstruction process with an antimask is also called deconvolution. The projection and reconstruction as convolution can be easily performed if object, mask and detector are all the same size. In astrophysical applications, for example, the objects can be assumed to be infinitely distant, so that the incident light is parallel, and the mask can be as large as the detector. In near field applications, this assumption holds no longer (Figure 4.3).

The magnification must be considered, and the mask must be scaled before calculating the antimask.

On the base of the above described considerations, a new way to build the antimask for near field applications was developed. The scaling and the rotation of the mask is taken into consideration as follows: A point in the middle of the object plane is raytraced through the middle of each mask hole with the same parameters for the distances d_1, d_2 and rotation of the mask as in the experiment. The result is a scaled and rotated mask, SM, of the size of the detector with as many detector pixels containing a 1 as there are holes in the original mask (Figure 4.4). It has been shown[87] that for the construction of the antimask it is sufficient to take into account only the mask pattern, and not the size or shape of the holes. This is the so called delta decoding. For some reconstructions the results were better when the detector pixels were refined for the scaling of the mask, *e.g.*, 528 x 528 or 1056 x 1056 instead of 264 x 264, which is the physical size of our detector. This refinement allows to locate the positions of the holes more precisely in the scaled mask. The antimask is then constructed as indicated in Equation 4.9, but with the scaled antimask:

$$AM(x,y) = FT^{-1}\left(\frac{1}{FT\left(SM\left(x,y\right)\right)}\right) \tag{4.10}$$

As the Fourier transform of the scaled antimask is in the denominator, this expression must not contain zeros. It turned out, that for some scaling factors in MURA based masks of arbitrary length, there appear zeros in the FT of the scaled mask. This is not the case for an inverted MURA based mask. Therefore, some simulations were carried out with the inverted MURA pattern.

This reconstruction method is mathematically well defined and widely applied in astrophysical applications[88]. Some masks are better suited than others[89] and there have been many different propositions of mask designs[66]. For the purposes of this project the chosen MURA pattern worked reasonably well. The construction of the antimask is computationally easy as there exist fast fourier transform packages in Python (and other programming languages). The method is sensible to the exact position of the holes in the scaled mask, so that a shift of one pixel can make the reconstruction impossible. Hence it is indispensable to know the experimental arrangement. When the antimask is built correctly, the reconstruction via deconvolution is easy and fast (less than 0.1 s).

Reconstruction with iterative algorithm

Another reconstruction method, that is used for example in computed tomography (CT) applications, is iterative reconstruction.

A flow scheme of the iterative reconstruction method is shown in Figure 4.8. The projection of a first guess is simulated and the result of this simulation is compared to the original detected image. As the contribution of every object pixel to every detector pixel is known, it is possible to optimize the guess by changing the values in the pixels. The updated guess is projected again and the result compared to the recorded image. This step is repeated until a predefined number of iterations or limit of improvement of the difference between projected guess and recorded image is reached.

The difference is defined as the mean of the square root of the squared difference between projected guess and recorded image for all pixels:

$$\text{diff} = \frac{1}{N} \cdot \sum_{j=1}^{N} \sqrt{(g_j - i_j)^2} \tag{4.11}$$

The optimization is done with a self written Python program using the Adam optimizer of the tensorflow package. Besides the physical parameters, that are defined by
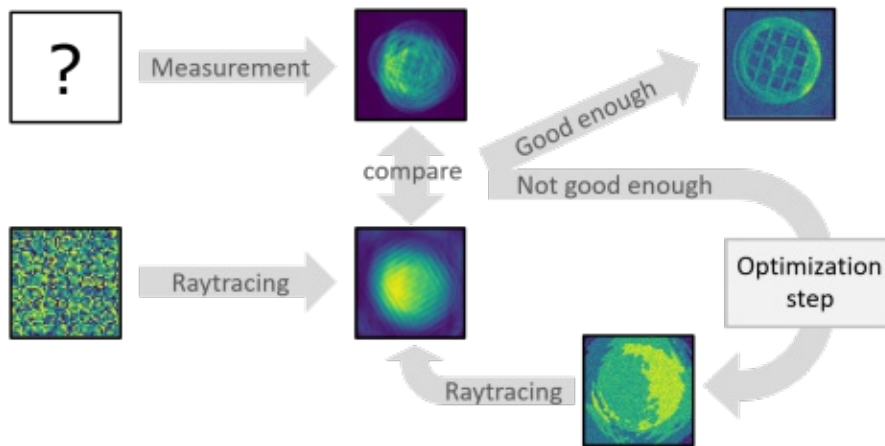
Figure 4.8: Scheme of the iterative reconstruction method

the projection function, the first guess can be chosen as well as the smallest improvement from one iteration to the next and a maximum number of iterations as breakoff criteria, and the learning rate of the optimizer.

This reconstruction method is mathematically defined and gives good results when the projection function is well known. In principle the resolution can be chosen by adjusting the object pixel size. For example a lower resolution can be used to get a first idea about the sample and then the object pixels can be refined until no more improvement is achieved, *e.g.*, the physical limits of the resolution are reached.

The iterative reconstruction can take very long, up to several hours for one reconstruction, depending on the size of the object. Furthermore, if the projection function matrix gets to large this could be a problem for the computer memory. The calculations

were performed on a normal laptop (Intel(R) Core(TM) i5 - 5200U CPU @2.20 GHz, 2 kernels, 4 CPUs, Memory 238 GB). With this computer objects of sizes up to approximately 225 x 225 pixels and detector size of 264 x 264 pixels could be handled with dense matrices. The use of sparse matrices allowed larger objects to be reconstructed.

Reconstruction with evolutionary algorithm

An evolutionary algorithm is an optimization method that aims to model the process of natural evolution. A flow scheme of this reconstruction method is shown in Figure 4.9. First, a parental generation is initialized. It consists of a number, *popsize*, of random first guesses for the object to reconstruct. Every individual of this first generation is raytraced and the simulated projection is compared to the measured data. The difference between the simulated and the real projection is used as a measure for the so called fitness of each individual. The lower the difference, calculated as the mean of the squared pixel differences, the higher the fitness. A predefined proportion of the parental generation is used to produce offspring. Therefore, two of the fittest individuals are chosen at random and transmit their pixel values to a new individual according to their fitness. In a mutation step, the pixels of the offspring are mutated with a predefined probability, for example the pixel value is changed according to a Gauss distribution. This step is repeated until *popsize* offspring are created that form the next generation. After a fix number of iterations or when the best difference is smaller than a set *breakoff* value, the reconstruction is stopped.
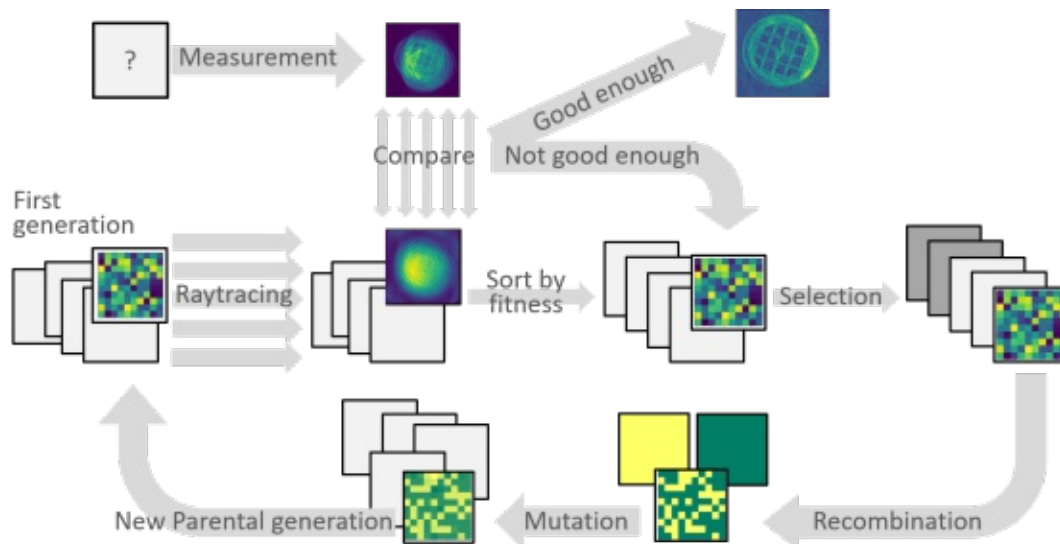
Figure 4.9: Scheme of the evolutionary algorithm

The evolutionary algorithm reconstruction process is an entirely random process with evolutionary selection. The recombination and mutation also take place entirely ran-

domly. As for the creation of each new generation all the individuals must be projected and *popsize* recombinations of parents must be performed, this algorithm is slower than the iterative reconstruction. However, its invaluable advantage is that it is less likely to run into local minima.

There are different parameters that influence the quality of the reconstruction with the evolutionary algorithm. These are the population size, the mutation probability, the mutation function and its parameters and the fraction of the population that is used to create offspring. The optimization of these parameters must be a compromise between the computational cost and the improvement of the reconstruction. For example, a larger population size increases the probability to have good guesses, but it slows down the calculation. A large fraction of individuals to create offspring means more diversity and more changes from generation to generation, that could accelerate the evolution, but at the same time this means that less fit individuals contribute to the next generation. The mutation function determines how much the individual is changed independently of their predecessors. If the changes are too large the advantages of inheritance from good individuals are neglected. If the changes are too small, it can take very long to find a suitable reconstruction. One possibility is to use an adaptive mutation function. Here, the strength of the mutation can be coupled for example with the average fitness of the ancestors, *e.g.*, the fitter the ancestors, the smaller the mutation. The multitude of parameters to adapt requires a careful optimization

Reconstruction with machine learning algorithm

For the image reconstruction with a machine learning algorithm, a mixed-scale dense convolutional neural network as proposed by D. M. Pelt and J. A. Sethian in 2018[90] was used. This type of network is easy to implement and applicable to different problems in the domain of imaging applications. A schematic representation of its architecture is shown in Figure 4.10.

In imaging problems the task for a neural network is always to model an unknown function that maps the input to an output. This can be for example for an image classification task a function that assigns 1 or 0 to an input image, depending on whether the image contains the target object or not, or a denoising function that outputs a denoised image of the same size as the input image. In our case the input is the recorded image with overlapping projections, and the output is the reconstructed object. The neural network models the imaging function by using several layers, where each layer transforms an input image to an output image, called feature map. Each layer can consist of several different operations; for a convolutional network this includes the convolution with different filters, the addition of a bias, and a nonlinear operation, the activation

function, to each pixel.

In the training process, the different parameters, *i.e.*, the filters, biases and weights for the activation must be learned. In supervised learning, as used in this work, training data consisting of known input-output pairs are used to sequentially optimize all parameters. Therefore, the output of the network is compared to the known target output, and the difference between the network output and the target is minimized by optimizing the learnable training parameters by gradient descent in the course of the training cycles.

Deep convolutional neural networks (DCNN) have a large number of layers and can learn more complicated functions. DCNN use a large number of intermediate pictures and different operations, for example, often they use downscaling in the first part of the network, and upscaling in the second part, to capture features on different scales. These DCNN have often several millions of training parameters to learn. Different layers use different sets of operations and the connection between the layers can also be adapted, which leads to an architecture that is very problem specific, but must be changed when another task should be performed. The large amount of learnable parameters leads to an increase in training time, and increases also the likelihood of overfitting, when the network adapts too well to the training set and is not able to generalize to unknown data.

In the mixed-scale dense convolutional neural network (MSDNet) all layers use the same set of operations and are connected in the same way. The used dilated convolutions can capture features at different image scales without down- and upscaling. Hence, all feature maps have the same dimensions (unlike in networks that use down- and upscaling), and this allows to use all feature maps as input for every layer. This means a maximal use of feature maps and, in turn, less feature maps, and in consequence less layers, are needed. All this together leads to a network architecture with relatively few training parameters, that is easier to implement, train, and apply in practice. For more information about the MSDNet see[90].

The network used for the reconstruction in this work was built using the Python implementation of the Mixed-Scale Dense Convolutional Neural Network by Pelt and Sethian[90][91]. The parameters are the same as in the example in the corresponding paper, *i.e.*, the number of layers is 100, the dilations are defined as in the paper, and 1 input and 1 output channel are used. The input is the recorded detector data, the output is the reconstructed object.

Training data for the network is produced as follows: For most of the samples there is at least one projection of the mask pattern (see Figure 4.19 e)). This mask pattern is extracted to get information about the projection function of the experimental setup. This includes the angle of rotation of the mask relative to the detector and the relation between the distances between object, mask and detector that defines the magnification
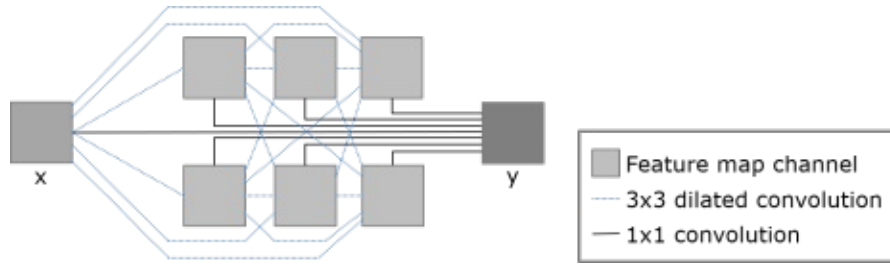
Figure 4.10: Schematic representation of an mixed-scale dense convolutional neural network with three layers and two channels per feature map. This picture is adapted from the publication by D. M. Pelt and J. A. Sethian[90].

factor. Training data is obtained by convolving input images with this projected mask. Thus, pairs of example input images and simulated projections of these input images are obtained that are used for the training of the network, e.g., the optimization of all learnable training parameters in the network. In this way, the network models the reconstruction function.

The choice of the training input data has to be made carefully. All sort of structures that are contained in the sample should be represented in the training data to get good results, *e.g.*, points, lines and areas of different intensities.

The training process is stopped, when the accuracy of the reconstruction of the training data does not improve any more over 20 iterations. This method is called early stopping. The quality of the reconstruction of the network can be controlled in the course of the training by testing a set of validation images with the actual network parameters. For this purpose, input/output image pairs that are not contained in the training data set are used.

4.2 Simulations

Different series of simulations have been performed to characterize the system and compare the different reconstruction methods.

4.2.1 Influence of the mask thickness

First, the influence of the mask thickness on the reconstructions has been investigated. Therefore, experiments with three different masks were simulated, with the only difference being the thickness. The mask is an inverted NTHT MURA mask of rank 29 with a hole size of 50 μm and a spacing between two holes of equally 50 μm. Hence, the physical size of the mask is 2.9 mm. The values for the thickness of the mask are 0 μm, 50 μm and 100 μm respectively. The detector has 262 x 262 pixels with a size of

(50 x 50) µm^2, the object has 40 x 40 pixels with a size of (55 x 55) µm^2 and values of 0 and 1, representing three circles with different diameters. The distances are $d_1 = 10\,\text{mm}$ and $d_2 = 20\,\text{mm}$. These parameters are realistic also for real experiments. The results of these simulations are shown in Figure 4.11.

The projections of the object through the masks have the same structure but the intensity decreases with increasing mask thickness because of the collimation effect for thicker masks. For the same region of the object, the intensity is relatively higher on the edges of the projections the thinner the mask is. For this reason, in Figure 4.11 the middle region of the projection is slightly brighter relative to the outer regions the thicker the mask is.

The reconstruction with the antimask (method 1, deconvolution) is the convolution of the simulated detector image with the calculated antimask. This is a single computation step and very fast; the results shown here are achieved in less than 0.1 seconds. With the new method for the construction of the antimask, pictures projected through inverted (NTHT) MURA masks of arbitrary side length (in accordance with the MURA building rules) and for arbitrary scaling factors can be reconstructed. The reconstructed objects with the antimask reconstruction method have not the original object size, but the scaled size. Here, the original object had a length of 40 pixels $\cdot$ 55 µm $= 2200\,\text{µm}$. The reconstructed object has a side length of 88 detector pixels, that is a size of $88 \cdot 50\,\text{µm} = 4400\,\text{µm}$. This is exactly the expected size, because the scaling factor is $d_2/d_1 = 20/10 = 2$. To obtain the original size, a central extension with the inverse scaling factor can be performed. The reconstruction in the ideal case of an infinitely thin mask is nearly perfect. But for thicker masks, system inherent distortion is inserted. The contrast gets worse the thicker the mask, and furthermore, ghost images appear. Simulations with other distances d_1 and d_2 but the same quotient d_2/d_1 show that the collimation effect becomes more important the smaller the distances are. This is due to the fact that in the reconstruction with the antimask the projection process is only approximated by a convolution and the mask thickness is not taken into account. This means that for an experiment with limited space, where only small distances are possible, or when the experimental requirements are such that the distances should be kept very small, for example to avoid absorption of radiation in air, this reconstruction method could come to its limits.

The iterative algorithm reconstruction method (method 2) works well for all tested mask thicknesses. The results shown in Figure 4.11 are obtained in 50 iterations and the learning rate is 1. The initial guess is a random matrix from an uniform distribution with values between 0 and 1 of the same size as the original object. For thicker masks an object pixel contributes to less detector pixels and there are less entries in the transfer matrix and therefore less ambiguity in the reconstruction. The calculation time for the
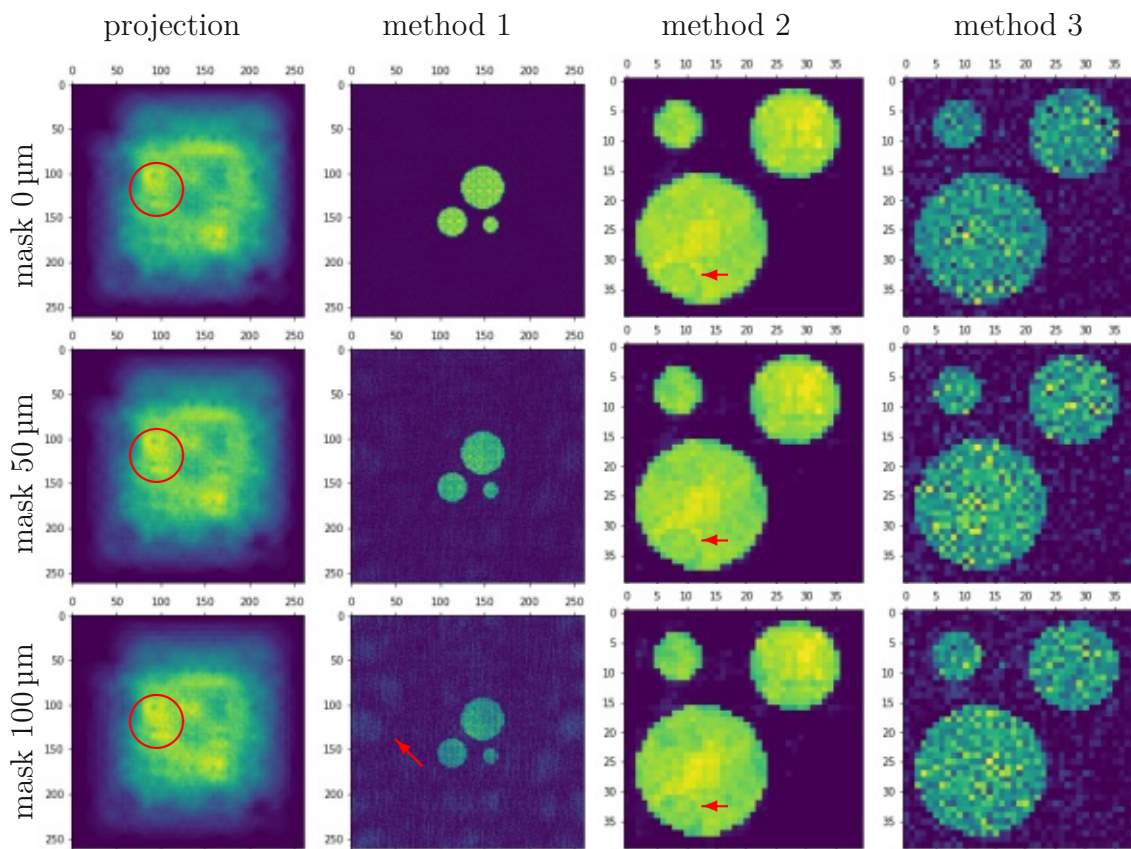
Figure 4.11: Comparison of the simulated projection and reconstruction with different mask thicknesses and different reconstruction methods. The mask thicknesses are 0 μm (top), 50 μm (middle) and 100 μm (bottom). The first column shows the simulated projection. The differences are not very clearly visible. There are small differences in the intensities of the structures in the middle of the projection (red circles). The second column shows the reconstruction with deconvolution (method 1). The reconstruction for the thin mask is nearly perfect, but for the thicker masks the intensity of the discs decreases and ghost images appear (red arrow). This is due to the fact that the projection with a thick mask at small distances is not a perfect convolution of the object and the mask pattern, and hence the deconvolution cannot be a perfect reconstruction. The third column shows the reconstruction with iterative algorithm (method 2), the fourth column the reconstruction with evolutionary algorithm (method 3). For these two methods, there are no systematic differences between the different masks. This reflects the fact that the mask thickness is modeled and used in these reconstruction methods. In the reconstruction with method 2, there are structures in the reconstructed images that are similar for all mask thicknesses. This is a result of the deterministic algorithm. In the reconstruction with method 3, there are no structures, because this reconstruction method involves random changes in every iteration step.

reconstruction was between 80 and 140 seconds for the shown results.

For all mask thicknesses the original object is clearly recognizable, even if there are some structures in the reconstructed object which are introduced by the reconstruction algorithm. The mask thickness has no negative impact on the reconstruction because it is modeled in the projection function used for the iterative reconstruction. The structures are similar in all three reconstructions, which indicates that they are due to the iterative algorithm. It shows that this algorithm is deterministic, and with the same first guess, for the same input always the same result is obtained. For simulations with this simple object and without noise, it is in principle possible to get perfect reconstructions with more iterations. The reconstruction process was stopped before to show the effect of the iterative algorithm on the reconstruction.

The reconstruction with the evolutionary algorithm (method 3) was also possible for all three tested masks. The mutation probability was 0.05, meaning that about 5% of the pixels of each offspring are mutated. Here, the mutation is the addition of a value from a normal distribution with a standard deviation of $\sigma = 0.1$. The population size was 60, the fraction of best individuals for the creation of offspring was 12.5% and each reconstruction was run for 5000 steps. The reconstruction time was around one and a half hours for the fastest reconstruction. There is no quality loss in the reconstruction when thicker masks are used and there are no structures in the reconstructed objects. However, the computational effort is high and the results not as satisfactory as for the iterative algorithm. But contrary to the iterative algorithm there are no structures in the reconstruction. This is due to the fact that the mutation in each iteration loop adds a purely random element.

It should be mentioned that the reconstruction time depends on all other processes running on the computer and that the times stated here should not be seen as absolute values, but they can help to estimate and compare the computational effort necessary for the different reconstruction methods.

The comparison of the three methods shows that in principle all of them can be used for the reconstruction of images projected through a coded aperture. However, for some cases the collimation effect of thicker masks becomes important for the reconstruction method 1, whereas methods 2 and 3 are not affected in the case that the mask thickness is carefully considered in the calculation of the projection function. The results suggest furthermore that the insertion of randomness could avoid the structures seen in the reconstructions with the iterative algorithm as the (random) evolutionary algorithm does not show these structures.

4.2.2 Resolution

Further simulations have been performed to test the system's resolution. Therefore, a simple test arrangement was chosen: Objects consisting of vertical stripes with a width of one pixel are projected through a mask onto a detector with a size of 60 x 60 pixels each with a side length of (50 x 50) µm². Different masks are used, but the hole size is always 50 µm and the thickness 50 µm. One mask consists of only one pinhole, another mask is a MURA of rank 5 with 12 holes with a distance of 200 µm between two neighboring holes. Three series of simulations are performed with distances $d_1 = d_2 = 10$ mm, once with the pinhole, once with a non-rotated mask and once with a MURA turned by 15 degree. The series with the non-rotated MURA is repeated with distances $d_1 = 10$ mm and $d_2 = 11$ mm. The object pixel sizes are 20, 25, 30, 40 and 50 µm. The reconstruction is performed with the iterative algorithm for 500 steps. The results are shown in Figure 4.12.

The results suggest a better resolution than calculated in Equation 4.4 which would be 200 µm for the simulated geometrical arrangement. This discrepancy is due mostly to two facts: In the projection function, only the middle of each object pixel is considered, not the real dimension of the pixel. Furthermore, the mask thickness is neglected in Equation 4.4. The mask thickness leads to a collimation effect as shown in Figure 4.3 c) that affects the resolution because the actual hole size is smaller depending on the position of the object pixel. This leads to a better resolution on the edges of the object (see Figure 4.12 pixel size 40 µm for the pinhole and the MURA without rotation). Therefore, the simulated resolution is not the resoultion of the real system. Despite this discrepancy the results of the simulation can illustrate the effect of the projection of the same object shifted by values of less than one detector pixel length, the multiframe super-resolution. Due to the highly symmetric arrangement and the idealized simulation, the pixel shifts of the projections are integer multiples of the detector pixel length in the case of the non-rotated MURA mask, hence there is only a small advantage compared to the pinhole. When the MURA mask is rotated, the shifts become non-integer multiples and the resolution becomes significantly better. The same effect can be achieved when d_1 and d_2 or the distances between two holes in the mask, d_h, are chosen suitably. This means that the expression

$$\frac{d_1 + d_2}{d_1} \cdot d_h$$

must not be an integer multiple of the detector pixel size. Let's consider the here described simulation with distances $d1 = d2 = 10$ mm.

For the non-rotated mask, the distances in x- and y-direction between two holes are
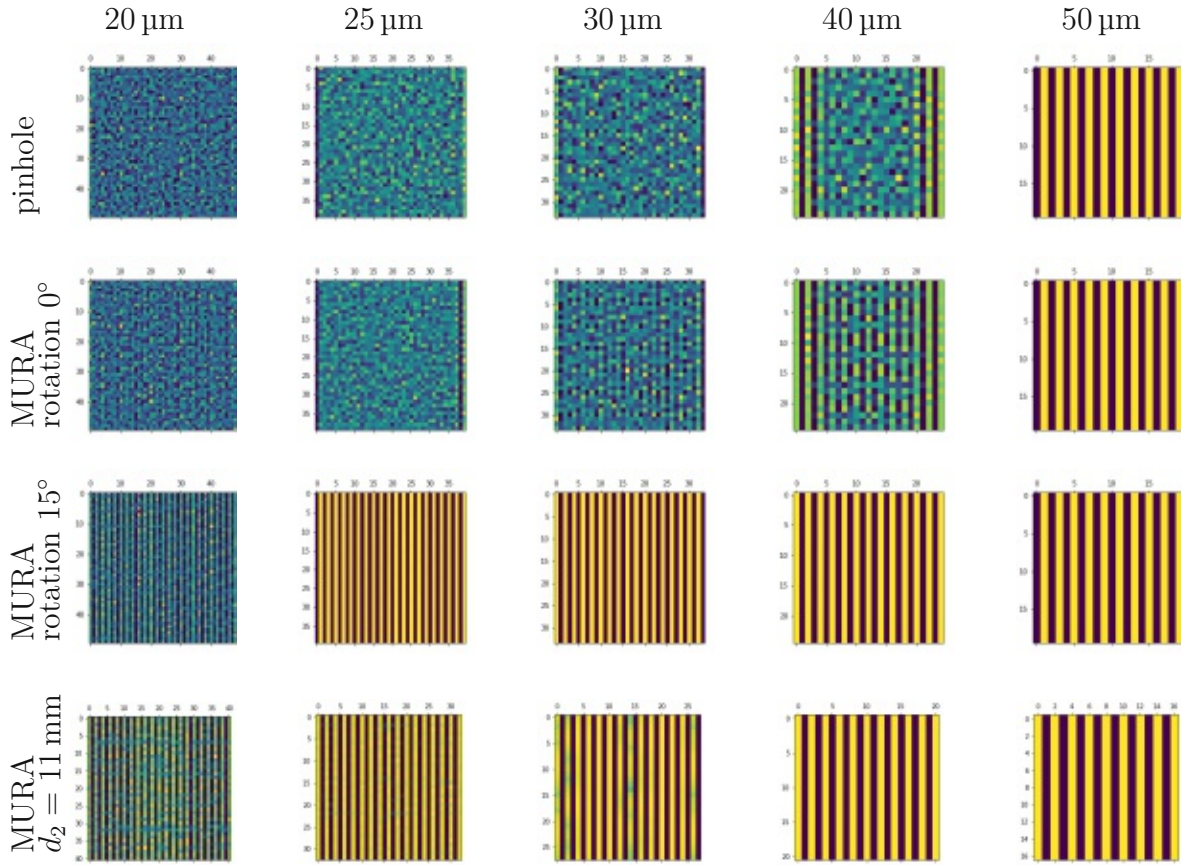
Figure 4.12: Simulations to test the resolution with a pattern of vertical stripes. The geometry of the setup is the same for the simulations shown in the first four lines, $d_1 = d_2 = 10\,\mathrm{mm}$. For the simulations in the last line $d_1 = 10\,\mathrm{mm}$ and $d_2 = 10\,\mathrm{mm}$. The side length of one pixel is indicated on top of the columns. The simulations were performed with three different masks, one single pinhole, a NTHT MURA of rank 5 without rotation and the same mask, but rotated by 15° relative to the detector. For the non-rotated MURA and $d_1 = d_2 = 10\,\mathrm{mm}$, the different projections are shifted always by integer multiples of the detector pixel size in x- and y-direction. The resolution of the reconstructed object is similar to that of the projection through a single pinhole. For the rotated mask, there are different shifts of the projections on the detector, including non-integer multiples of the detector pixel size, which is the condition of multiframe super-resolution. The same is true for the projection through a non-rotated mask with distances $d_1 = 10\,\mathrm{mm}$ and $d_2 = 10\,\mathrm{mm}$ (last line). These simulations show that the multiframe super-resolution is inherent in the iterative reconstruction method, when the mask hole pattern, mask orientation and distances between object, mask and detector are carefully chosen.

always integer multiples of the distance between two neighboring holes, *i.e.*:

$$d_h = n \cdot 200\,\mu\mathrm{m}$$

$$\text{and } \frac{d_1 + d_2}{d_1} \cdot d_h = \frac{20\,\mathrm{mm}}{10\,\mathrm{mm}} \cdot n \cdot 200\,\mu\mathrm{m} = n \cdot 400\,\mu\mathrm{m},$$

which is an integer multiple of the detector pixel size of $50\,\mu\mathrm{m}$. This means that no multiframe super-resolution is possible and the gain in resolution compared to a single pinhole is negligible. If there is an effect on the resolution, this is only due to the collimation effect that leads to slight differences between the projections through the different holes, and thus adds information to the projected image that is not contained in the single pinhole projection.

For the mask rotated by 15 degree, the distance between two neighboring holes in x- and y-direction are:

$$d_x = 200\,\mu\mathrm{m} \cdot cos(15°) \approx 193.2\,\mu\mathrm{m}$$

$$d_y = 200\,\mu\mathrm{m} \cdot sin(15°) \approx 51.8\,\mu\mathrm{m},$$

leading to

$$\frac{d_1 + d_2}{d_1} \cdot d_x = \frac{20\,\mathrm{mm}}{10\,\mathrm{mm}} \cdot 193.2\,\mu\mathrm{m} = 386.4\,\mu\mathrm{m}$$

$$\text{and } \frac{d_1 + d_2}{d_1} \cdot d_y = 103.5\,\mu\mathrm{m}.$$

Distances between the projections through arbitrary holes are integer multiples of these distances in x- and y-direction. Thus, the shifts are non-integer multiples of the detector pixel size and the resolution gets better through the principle of multiframe super-resolution.

A similar effect can be seen when the distances d_1 and d_2 are well chosen. For example, for distances $d_1 = 10\,\mathrm{mm}$ and $d_2 = 11\,\mathrm{mm}$ (see Figure 4.12)

$$\frac{d_1 + d_2}{d_1} \cdot d_h = \frac{21\,\mathrm{mm}}{10\,\mathrm{mm}} \cdot n \cdot 200\,\mu\mathrm{m} = n \cdot 420\,\mu\mathrm{m},$$

which is again a non-integer multiple of the detector pixel size.

The simulations show that in principle the multiframe super-resolution is inherent in the CAI with an iterative reconstruction process, when the experimental setup is carefully chosen.

4.3 Experiment

4.3.1 Experimental setup

All measurements were carried out at the BAM*line* at BESSY II (HZB). The X-ray source provides hard X-rays in the energy range between 4 and $100\,\text{keV}$[27]. For the experiments an excitation energy of 15 keV was chosen. The setup is shown in Figure 4.13. The incoming x-rays hit the sample that is placed on a stage allowing the adjustment of the position in the beam and the angle between beam and sample. The fluorescence radiation falls through the mask and is detected by a detector placed at 90° relative to the incoming beam. The distance d_1 between sample and mask can be easily adjusted by means of the sample stage. The minimum distance d_2 between mask and detector is determined by the distance between entrance window of the camera and the chip, which is 6.2 mm. The distance d_2 can be changed, when the mask holder (see Figure 4.14) is screwed more or less into the optics mounting, or turned. In addition a number of different aluminum spacers could be used to enlarge the distance between mask and detector. However, the experiments presented here are performed without spacers. The vertical beam size was between 0.2 mm and 0.95 mm, the tilting angle of the sample relative to the incoming beam was up to 0.4°. The illuminated area on the sample is defined as $A = beamwidth \cdot beamheight \cdot sin\alpha$. For example, with a beam width of 10 mm, a beam height of 0.5 mm and an angle a of 0.4° an illuminated area of 10 mm x 71.62 mm is achieved. For every sample, first the projected image on the detector screen was optimized. Afterwards images were recorded from 1 minute exposure time up to 15 hours. The data was stored in .h5-files, containing information about the measurement time and the events recorded by the detector.

4.3.2 Mask

The MURA used for the experiments has rank 5. It possesses 12 holes of $90\,\mu\text{m}$ diameter drilled in a $25\,\mu\text{m}$ thick platinum foil. The area of the mask has a side length of 1 mm. Figure 4.15 shows the mask in its holder. As the holes have circular shape, the open fraction, f_o, of the mask can be calculated as follows:

$$f_o = \frac{12 \cdot (45\,\mu\text{m})^2 \cdot \pi}{1\,\text{mm}^2} \approx 7.6\%$$ (4.12)
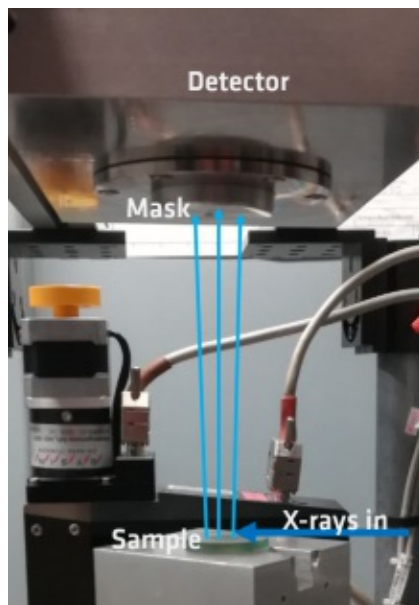
Figure 4.13: The experimental setup. The beam comes from the right (broad arrow) and hits the sample which is located on an Euler cradle. The fluorescence (small arrows) is detected by the pnCCD. The distance d_1 between sample and mask can be changed easily. For the photo the distance is enlarged to show the setup more clearly. In the experiments much smaller distances d_1 were used. The distance d_2 can be adjusted by spacers. The minimum distance between mask and detector chip is determined by the position of the chip behind the entrance window of the camera, which is $6.2\,\mathrm{mm}$.

a) View from above

b) View from below

c) Different spacers
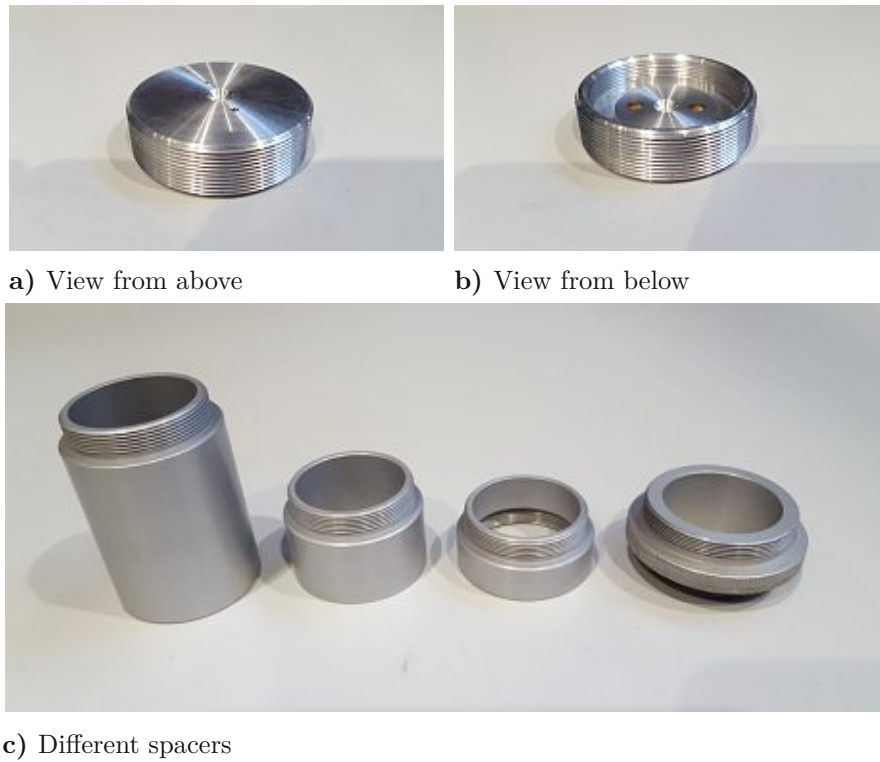
Figure 4.14: Mask holder and spacers

Figure 4.15: Mask in its holder. The 12 holes are drilled in a 25 mm thick platinum foil. The foil is placed into a holder manufactured for this purpose that can be screwed into the optics mounting of the camera.

4.3.3 Detector

The detector is an energy dispersive array detector, in this case a pnCCD. Normally, this detector is used together with a polycapillary optic for full field X-ray fluorescence methods, and is then called "color X-ray camera"[77,92]. It has been developed and tested in a cooperation between the Instutite for Scientific Instruments GmbH (IfG), the Federal Institute for Materials Research and Testing (BAM), PNSensor GmbH, and the Insitut für Angewandte Photonik e.V. (IAP). The CXC consists of a pnCCD detector, a polycapillary optic, the housing, cooling, data acquisition system and dedicated analysis software. In this work, the polycapillary optic is replaced by a coded aperture. The pnCCD detector has 264 x 264 = 69696 pixels, each with an area of 48 x 48µm^2. The imaging area is 12.7 x 12.7mm^2. It is designed for an ultrafast channel parallel readout, has a high quantum efficiency in the X-ray range, an energy resolution of 152 eV at the manganese K_α energy (5898.75 eV), which is comparable to that of a SDD, and a high frame rate (400 Hz up to 1000 Hz). The most important characteristics of this detector are summarized in Table 4.1. The detector consists of a 450 µm thick n- doped silicon substrate. On both sides of this substrate highly doped p+ structures are implanted. On the back side, the p+ doped layer is homogeneous and unstructured. It serves as the radiation entrance window. On the opposite side, the p+ doped implants are structured in a 3-phase register structure, where three registers form one pixel in the direction of the charge transfer. The applied voltage leads to a complete depletion of the n- doped silicon substrate, so that the whole thickness of 450 µm is sensitive to radiation. An incoming X-ray photon creates electron-hole pairs that are separated by the applied voltage. The electrons are trapped in the electric potential minima of the single pixels. The charge transfer to the neighboring pixel is performed by fast switching of the register voltages, and has a very high efficiency of > 0.99995. Figure 4.16 shows a simplified scheme of the working principle of the pnCCD. All pixels in a row are read out in parallel (channel parallel readout). At the end of each channel an on-chip junction field effect transistor (JFET) amplifier operated in source follower configuration provides the first signal amplification of the charge signals. Further processing is performed by four dedicated programmable analog signal processor chips (CAMEX).

The location and energy of the incoming photon can be reconstructed by considering the number and location of produced electrons. The probability for so-called split events, when the electron cloud produced by a single event is spread over more than one pixel, is relatively high. However, the data analysis software accounts for these split events by summing up the electrons that have been detected in neighboring pixels. This algorithm is very precise unless the count rate is too high and lead to an overlap of events, which is a limiting factor for the count rate.
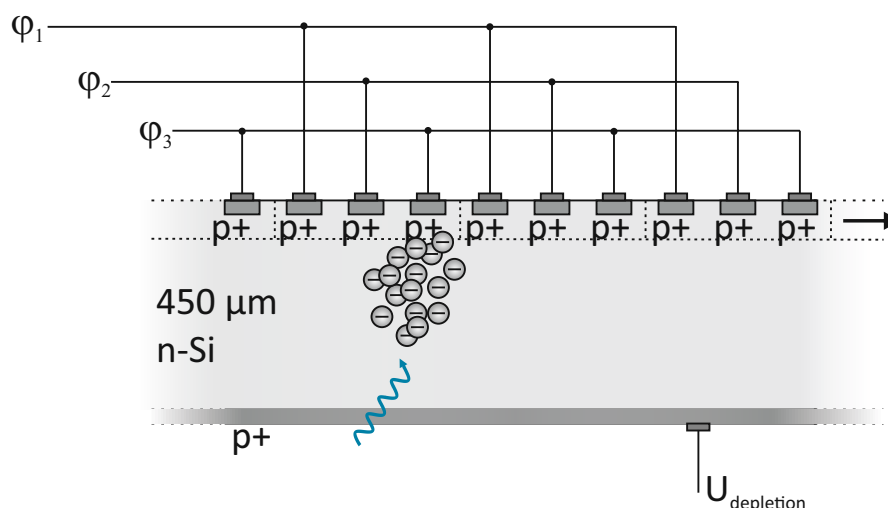
Figure 4.16: Scheme of the working principle of the pnCCD. The photons entering from the back side of the detector produce electron clouds that are confined in the electric potential minima. Three registers per pixel (ϕ_1, ϕ_2, ϕ_3) transport the signal charges towards a JFET at the end of each row. This is done for all channels in parallel.

Table 4.1: Summary of the pnCCD characteristics

parameter	value
pixel size	48 µm x 48 µm
number of pixels	264 x 264 = 69696
image area	12.7 mm x 12.7 mm
frame rate	400 hertz
pixel readout speed	28 Mpixel/s
quantum efficiency	> 95 % at 3 keV - 10 keV; > 30 % at 20 keV
sensitive thickness	450 µm
readout noise (rms)	3 e$^-$ / pixel
charge transfer efficiency	> 0.99995

4.3.4 Samples

For the shown experiments three different samples were used. Sample 1 is a polished ammonite as a representative natural example. The other two samples are printed patterns of different elements by drop on demand printing, performed at the institute for anorganic and analytical chemistry of the Technical University Clausthal-Zellerfeld. Detailed information about the printing of the pattern can be found in[93].

The patterns were printed on poly(methyl methacrylate) (PMMA) carriers (Bruker Nano, Berlin, Germany) (30 mm diameter, 3 mm thickness) without further modification. The distance between two residues was approx. 140 µm. In Figure 4.17 sketches of the printed patterns are shown as well as microscope images of sample 3. These microscope images show that the patterns consist of single droplets arranged to lines and areas. In

the sketches each colour represents a different solution in a different cartridge.

The mass of the residues was calculated using the results of the quantification with the internal standard as described in[93].

The first pattern represents the stylized logo of the BAM (Bundesanstalt fuer Materialforschung und –pruefung) and contains the elements Fe and Ga in different concentrations with a total mass of 104(5) ng of Fe and 106(3) ng of Ga.

The second pattern shows geometric figures without overlap with total masses of 25.9(8) ng Fe, 97(7) ng Co, 44(3) ng Ni, 56(4) ng Cu and 0.26(2) ng Sr.

a)   b)   c)   d)   e)
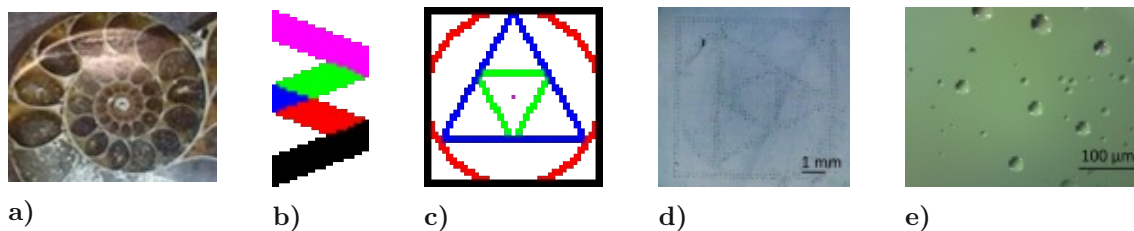
Figure 4.17: The investigated samples. a) Sample 1, a polished ammonite. b) Sketch of (printed) sample 2 (27 x 50 Px): Ga and Fe in different concentrations, black: 400 mg · L^{-1} / 0 mg · L^{-1} , red: 280 mg · L^{-1} / 120 mg · L^{-1}, blue: 200 mg · L^{-1} / 200 mg · L^{-1}, green: 120 mg · L^{-1} / 280 mg · L^{-1}, pink: 0 mg · L^{-1} / 400 mg · L^{-1}. c) Sketch of (printed) sample 3 (49 x 49 Px): black: Co, red: Ni, blue: Cu, green: Fe, pink: Sr; each 400 mg · L^{-1}. d) Microscope image of sample 3. The single droplets can be distinguished. e) Microscope image of sample 3, close up to the droplets.

4.3.5 Data treatment

The data from the experiment were handled with Python. The spectrum gives information about the counts per energy channel summed up over all detector pixels. The scale can easiliy be changed to energy, using the camera conversion factor. The scale can be verfied with the position of the peaks of the fluorescence radiation from known elements present in the sample. An example spectrum of sample 3 is shown in Fig. 4.18. In this case, the four main peaks between approximtately 6 keV and approximately 8 keVare associated to the K$_\alpha$ fluorescence lines of cobalt, nickel, copper and iron present in sample 3.

The projection image to reconstruct is contained in the 'raw' data, where the energy spectra are stored for every pixel. For the reconstruction of the different elements one by one, the recorded picture must be decomposed first. The simplest approach to perform the decomposition is to look at the spectrum and to chose different regions of interest corresponding to the different peaks in the spectrum. Then, all events in the chosen energy range can be depicted (see Figure 4.19 a) to e)). Another possibility is to use

118
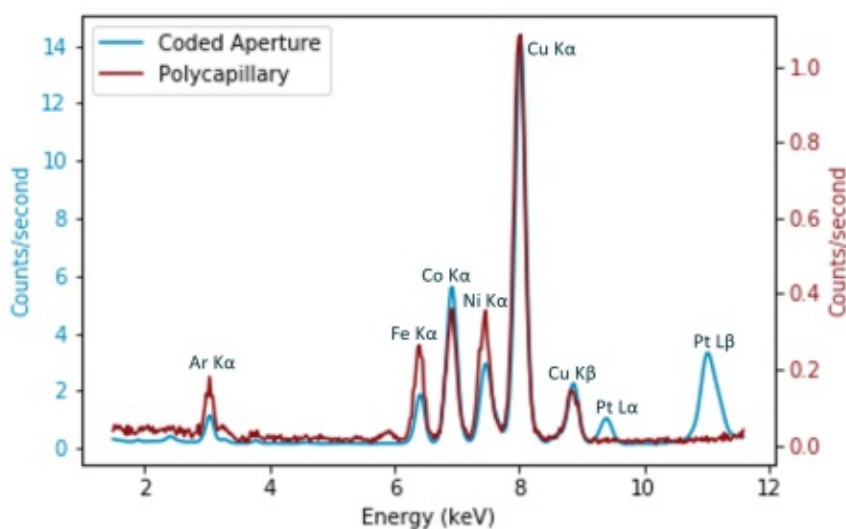
Figure 4.18: The energy spectrum of sample 3, recorded with the coded aperture (blue line) and the polycapillary (red line) (see Figure 4.20), summarized over a comparable region of the detector. In the spectrum of the coded aperture measurement, one can see additional peaks from the platin mask. Note the different scales.

principal component analysis (PCA) or non-negative matrix factorization (NMF), which are both contained in the sklearn.decomposition package for Python. This can be the method of choice for more complicated spectra or samples with unknown elemental composition.

a) Iron   **b)** Cobalt   **c)** Nickel   **d)** Copper   **e)** Coded Aperture
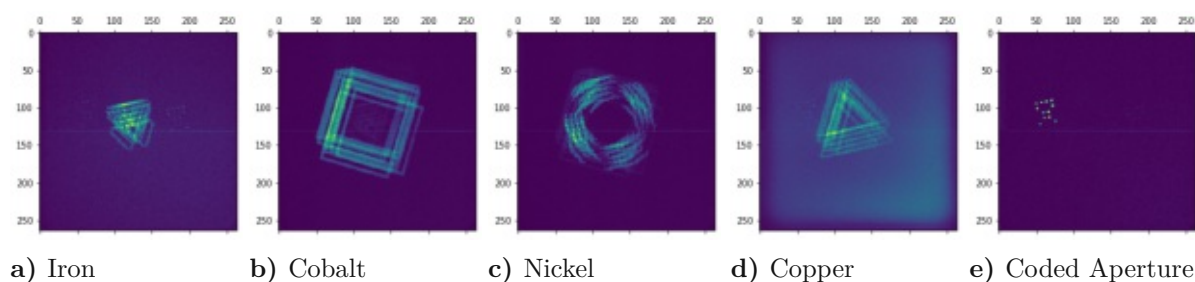
Figure 4.19: The distribution of events with energies corresponding to the different components of sample 3, the regions of interest are chosen to be the obvious peaks in Figure 4.18; a) 6.28 keV to 6.55 keV; b) 6.68 keV to 7.19 keV; c) 7.31 keV to 7.64 keV; d) 7.79 keV to 8.25 keV; e) 8.45 keV to 8.58 keV.

4.4 Results and discussion

The comparison of the records with the polycapillary and the coded aperture of three different samples are shown in Figure 4.20.

a) Sample 1, polycapillary **b)** Sample 2, polycapillary **c)** Sample 3, polycapillary

d) Sample 1, coded aperture **e)** Sample 2, coded aperture **f)** Sample 3, coded aperture
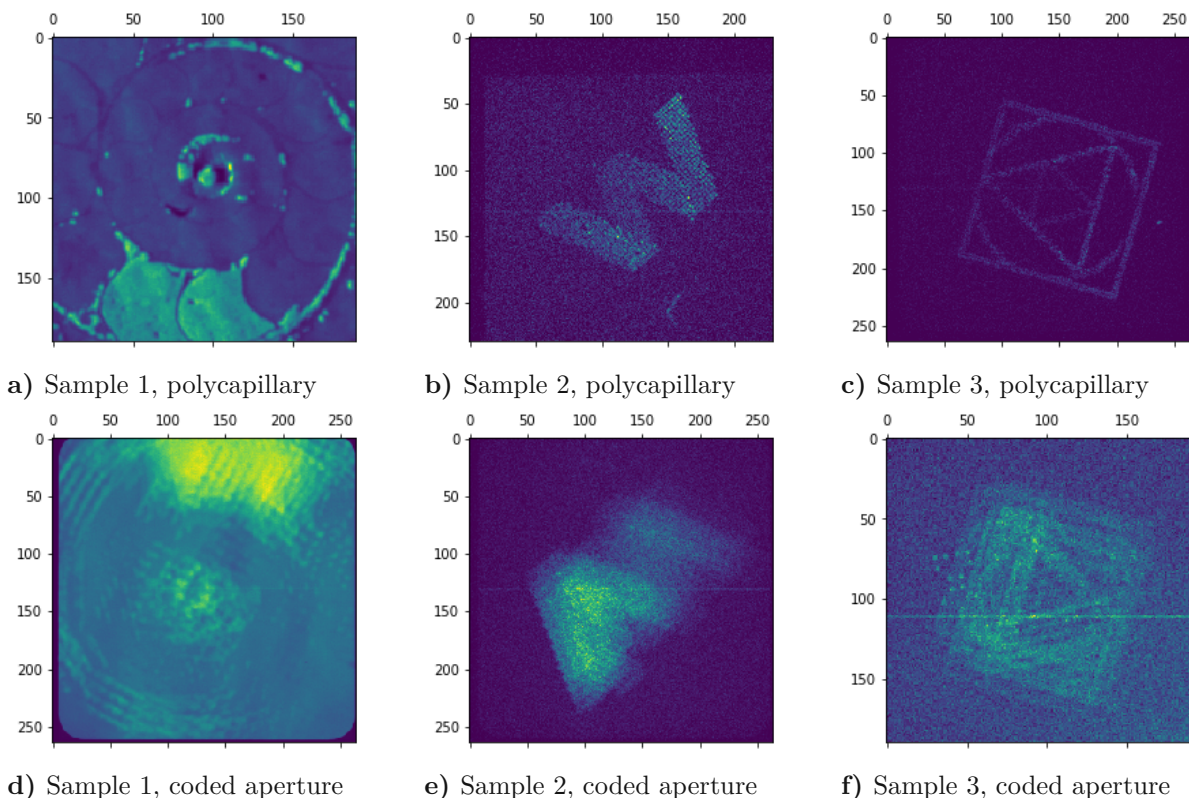
Figure 4.20: Different samples, measured with the polycapillary (a to c) and the coded aperture (d to f). Sample 1 shows an ammonite, sample 2 and sample 3 are printed with different elements. Pictures a, b and d are recorded in 10 minutes, pictures c and f are recorded in 13 minutes and picture e is recorded in 42 minutes. The pictures show the distribution of all events recorded in the energy channels 50 to 500 (of 1024) of the pnCCD. The sections of the detector screen are chosen such that approximately the same part of the object is displayed.

4.4.1 Count rate

One of the main advantages of the coded aperture is the higher count rate compared to the polycapillary optic. Here, the count rates of different measurements are compared. The corresponding recorded images are shown in Figure 4.20. The average count rate per second depends on the section of the object that is depicted on the detector. As the polycapillary used is a 1:1 polycapillary it shows always the same section of the object that has the size of the detector screen without magnification. The coded aperture

images can be magnified or downscaled, depending on the distances in the experiment. This means that not always the same section of the object is displayed as recorded by the polycapillary. This is reflected in clearly different count rates (counts per second averaged over the hole measurement) as can be seen in the upper part of table 4.2.

To get a better measure for the actual count rate, cut-outs of the detector images were used to get approximately the same part of the object for the polycapillary and the coded aperture. Then, the whole energy deposited in this area or the integrated raw spectra of the energy channels 50 to 500 were considered, normalized to ten minutes measurement time. The chosen energy region excludes the scatter peak of the incident energy. The results are summarized in table 4.2.

Table 4.2: Comparison between the count rates of measurements with the polycapillary and coded aperture

	polycapillary	coded aperture	ratio
counts per second			
(original image)			
sample 1	$1.1 \cdot 10^5$	$4.8 \cdot 10^5$	4.4
sample 2	$7.3 \cdot 10^3$	$5.8 \cdot 10^4$	7.9
sample 3	$2.8 \cdot 10^3$	$5.3 \cdot 10^4$	18.7
energy deposited			
[$\propto$ charge per pixel]			
(cut image area)			
sample 1	$3.2 \cdot 10^{11}$	$2.8 \cdot 10^{12}$	8.9
sample 2	$7.5 \cdot 10^{10}$	$6.4 \cdot 10^{11}$	8.5
sample 3	$3.2 \cdot 10^{10}$	$3.0 \cdot 10^{11}$	9.5
integrated raw spectra			
[counts per channel]			
(cut image area)			
sample 1	$4.0 \cdot 10^7$	$2.3 \cdot 10^8$	5.9
sample 2	$1.1 \cdot 10^5$	$8.5 \cdot 10^5$	7.6
sample 3	$5.4 \cdot 10^4$	$4.9 \cdot 10^5$	9.1

The simplest approach to calculate the increase in count rate theoretically is to normalize to the size of one single capillary and to multiply this by the size of a hole of the coded aperture and the number of holes:

$$cr_{ca} \approx cr_{pc} \cdot 12 \cdot \frac{90\,\mu m}{50\,\mu m} \tag{4.13}$$

$$\Rightarrow \frac{cr_{ca}}{cr_{pc}} \approx 21.6$$

The actual increase in count rate is smaller. This can be explained by the different geometries of the measurements with the polycapillary and the coded aperture. The photons entering the polycapillary are forwarded onto the detector, there is nearly no geometrical loss. In contrary, when using the coded aperture at the same distance to the object, some of the photons passing through the mask won't hit the detector because of their divergence. Further deviations in the gain in count rate, deposited energy and integrated raw spectra are due to the fact that only approximately the same section of the objects was used to calculate these quantities.

4.4.2 Reconstruction of the measured samples

The samples 1 and 3 could be reconstructed from the pictures recorded with the coded aperture (see Figure 4.21 on the left).

The original images are recorded in 10 minutes (sample 1) and 15 hours (sample 3).

Sample 3 consists of different geometric figures that are printed with different elements (see section 4.3.4). In Figure 4.21 the reconstruction of two different energy regions (Co, 6.68 keV to 7.19 keV and Cu, 7.79 keV to 8.25 keV) and the combination of all reconstructions is shown.

The reconstruction of sample 1 was done for the whole energy range between 1.5 keV and 12.8 keV at once.

In the measured projections of sample 2 there was no projection of the mask and the exact parameters d_1, d_2 and the rotation angle of the mask from the data could not be determined. This made the reconstruction difficult and the results are not satisfactory.

Reconstruction with the antimask (deconvolution)

For the reconstruction with the antimask, the antimask built as described in section 4.1.5 was used. The construction of the antimask and the reconstruction of the image is computationally easy and doesn't require much computational effort, if the mask is scaled according to the experiment. A first idea of the rotation of the mask and the magnification factor can be gained from the projection of the mask onto the detector. These parameters are scanned to refine them. To do this the reconstruction of the image is performed with several antimasks built from differently scaled and turned masks. The reconstructions are compared to find the best parameter combination.

The mask is always scaled to the detector size, so that the smallest mask (and antimask) element is the pixelsize of the detector. There are cases where a refinement of the recorded image by dividing pixels into subpixels yields better results in the reconstruction.
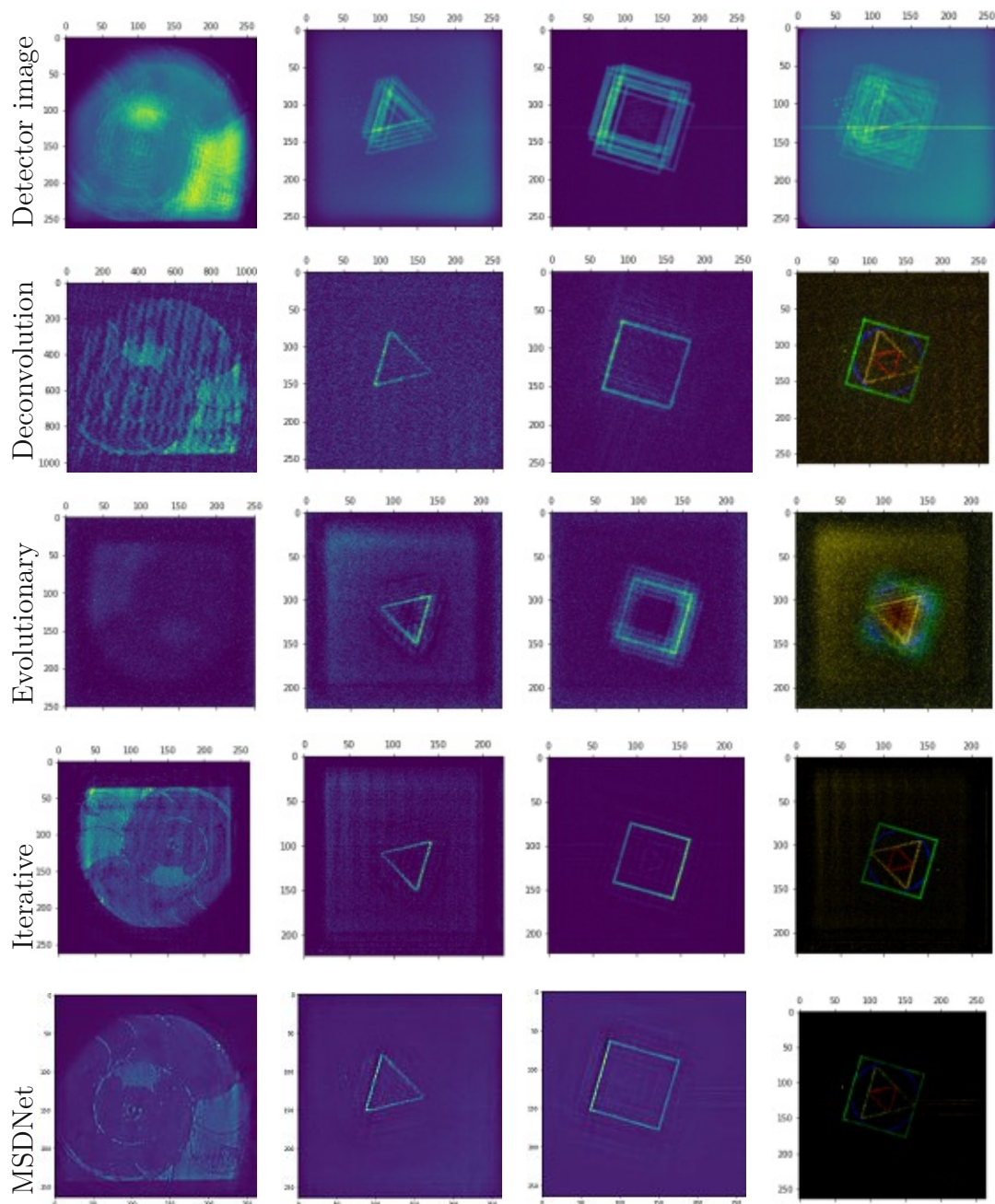
Figure 4.21: Comparison of reconstructions of samples 1 and 3 with different methods. First line: Detector images of sample 1 (first column), energies from 1.5 keV to 12.8 keV, and sample 3, different energy regions (second column: 7.79 keV to 8.25 keV (Cu Kα); third column: 6.68 keV to 7.19 keV (Co Kα); fourth column: combination of all energy regions (1.8 keV to 12.8 keV). The different lines correspond to the reconstruction method indicated on the left. The reconstructions shown in the last column are a combination of the reconstructions of the different energy regions, not the reconstruction of the hole energy range at once. The intensities of the combined reconstructions are adjusted, so that all patterns are visible.

For sample 1 the best results are obtained with a rotation angle of 81.47° and a magnification factor of $\frac{d_2}{d_1} = 0.575$. For this sample the refined detector image was used. The original recorded image and the reconstruction with the refined image are shown in Figure 4.21. The reconstruction with the original image was not possible.

For sample 3 the best results are obtained with a rotation angle of 281.31° and a magnification factor of $\frac{d_2}{d_1} = 0.64$. For this sample it was possible to use the original image. The refined images can also be reconstructed, but the results are not substantially better.

The reconstructions with the antimask are possible, but not always with the raw image. The method is very sensitive to little changes in the scaled mask. In the scaling algorithm, the middle of the object plane is calculated as the product of the central pixel and the pixel size plus one half times the pixel size. This is the origin of all rays that are traced through the middle of each mask hole. Because of this fact, the pixel size of the object has an influence on the scaled mask and there are differences in the reconstruction when different object pixel sizes are assumed.

Sometimes there are more than one best reconstruction for different scaling factors. It is necessary to make sure that the scaling factor is a realistic one that matches the experiment.

The size of the reconstructed pictures is determined by the size of the recorded image. The size of the original object can be calculated by scaling with the inverse scaling factor.

Reconstruction with the evolutionary algorithm

For the reconstruction with the evolutionary algorithm the same values for the rotation angle and the magnification factor found for the reconstruction with the antimask were used. The results shown in Figure 4.21 are achieved after 10000 iterations. Every reconstruction took about 4 to 5 hours.

Sample 1 was reconstructed considering the partially coded FOV, assuming an object pixel size of 90 μm, so that the reconstructed object has 251 x 251 pixels. The structure of the ammonite can be distinguished, but the contrast is not good and no details can be seen.

Sample 3 was also reconstructed with the partially coded FOV, but assuming an object pixel size of 100 μm, resulting in 224 x 224 object pixels.

Compared to the reconstructions with the antimask, the reconstructed objects are inversed. This orientation corresponds to the real orientation of the object, as the algorithm simulates realistically the projection process, and only an object with the correct orientation yields a realistic projection. Similarly, the size of the reconstructed object corresponds to the real object size.

The reconstructions with the evolutionary algorithm are recognizable, but not of high quality. The evolutionary algorithm requires a lot of computation time for the reconstructions.

Reconstruction with the iterative algorithm

For the reconstruction with the iterative algorithm the same values for the rotation angle and the magnification factor found for the reconstruction with the antimask were used. For all reconstructions the partially coded FOV was considered.

The object pixel size of the reconstructions of sample 1 in Figure 4.21 is 94 µm, resulting in 235 x 235 object pixels. The results shown here are achieved after 200 iterations of the optimization algorithm. One reconstruction took around 40 minutes.

The object pixel size of the reconstructions of sample 3 in Figure 4.21 is 100 µm, resulting in 264 x 264 object pixels. The result shown here is achieved after 500 iterations.

To show the differences between reconstructions with varying object pixel size, the reconstruction of the cobalt square of sample 3 is shown in Figure 4.22 for object pixel sizes of 100 µm, 75 µm and 50 µm, each result obtained after 500 iterations. The single droplets of the printed pattern are recognizable in the reconstruction with the smallest object pixel size.

a) 100 µm   **b)** 75 µm   **c)** 50 µm   **d)** zoom in 50 µm
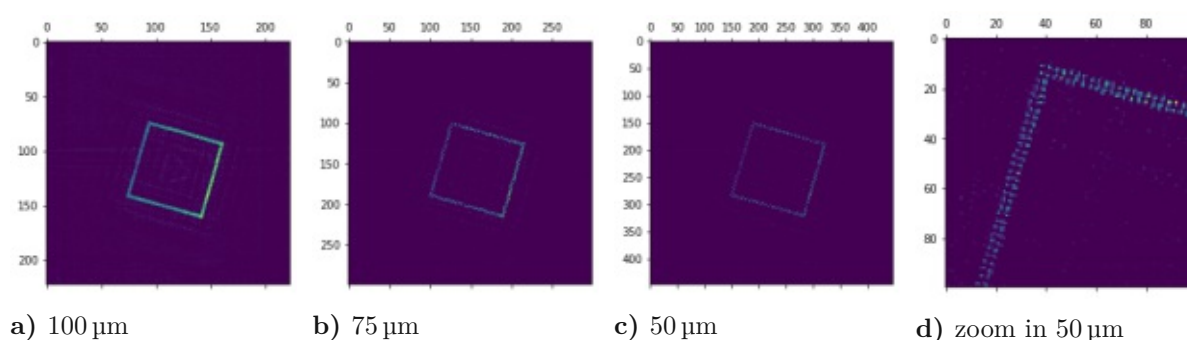
Figure 4.22: The influence of the object pixel size on the reconstruction.

Similarly to the reconstruction with the evolutionary algorithm, the size and the orientation of the reconstructed object correspond to the size and orientation of the real object.

The reconstructions with the iterative algorithm give satisfactory results, when a good projection function is found. In principle, the size of the object pixels can be chosen freely and herewith the resolution of the reconstructed image. In practice, a good resolution for a large field of view yields very many object pixels which slows down or even disables the reconstruction when there is not enough memory. The calculation of the projection function as described in 4.1.5 takes 300 seconds for 264 x 264 detector pixels and 118 x 118

object pixels. Once the projection function built, every component of every recorded picture with this same experimental arrangement can be reconstructed, one at a time or the hole energy range at once. The computation times for the reconstructions vary strongly with the number of pixels and the available memory, but they are in the range of several minutes up to one hour.

The reconstructions suffer from some artifacts. Sometimes, ghost images are visible. By improving the projection function or by data handling before the reconstruction such as background removal, this method can be further improved.

### Reconstruction with the machine learning algorithm

The results of the reconstruction with the MSDNet vary strongly with the choice of the training data. The influence of the training data on the reconstruction of sample 1 is shown in Figure 4.23. When using only randomly distributed points or single illuminated pixels for the training, the network can difficultly reconstruct areas. In contrary, when using only squares as training data the network reconstructed image is built from rectangles.

For the ammonite sample (sample 1) 800 pictures from the NASA Picture of the Day Archive were chosen, which contains images or photographs of the universe, including different sky objects such as galaxies, stars, planets, seen from the earth or from space telescopes. For the training, 10000 pictures were used, produced by inverting and rotating the NASA pictures. The projection was obtained by the convolution of the picture with the mask extracted from the measured data.

After the training of the MSDNet, the reconstruction of the images can be done very fast for every component of the recorded image. The input has the same number of pixels as the output, so if the 264 x 264 pixels image recorded by the detector is used, the result is an object with 264 x 264 pixels. The production of the training data involves a region that is slightly larger than the fully coded FOV but smaller than the partially coded FOV. For example, for sample 3 the fully coded FOV has a side length of 16.18 mm, the partially coded FOV has a side length of 23.62 mm and the reconstruction with the MSDNet covers a quadratic area with a side length of approximately 20.51 mm. This value was found by comparing the size of the reconstructed object to the known size of the real object. This means that the size of one pixel is about 78 μm.

The training data was obtained as described in section 4.1.5, with given values for the magnification and rotation of the mask. Hence, for every experimental setup a new training process is necessary. In principle, the parameters magnification and rotation could also be learned by the neural network. This would mean much more training data and effort.

126
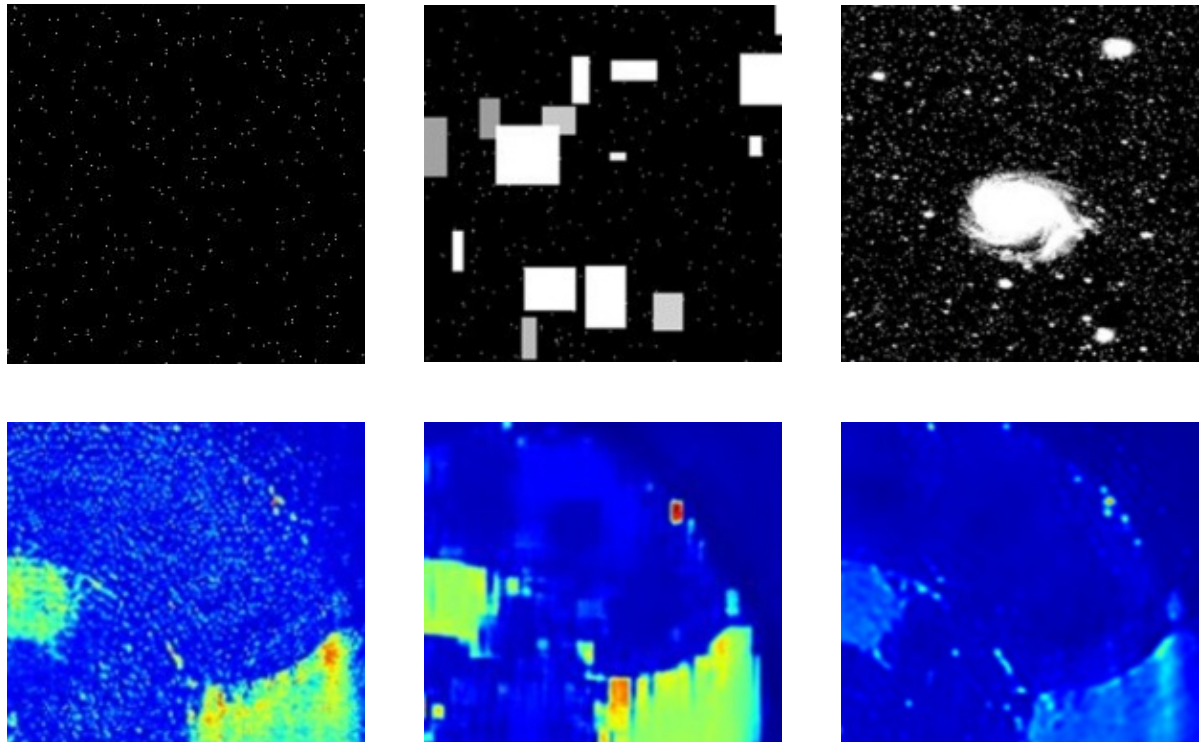
Figure 4.23: The influence of the training data on the reconstruction. Above three typical examples of different training training sets and below the reconstruction of sample 1 with the network trained with the respective training set. Left: Training data are images of randomly distributed points; middle: Training data are squares with different gray values; right: Training data are pictures from the NASA Picture of the Day Archive.

The reconstructions with the MSDNet are promising. This method could also benefit from an improved projection function that could be used for the generation of training data. In principle, an accurate raytracing would produce more realistic projections than the convolution method used for the training data generation.

4.5 Conclusions

A setup for full field X-ray fluorescence imaging with a coded aperture and an energy dispersive array detector has been implemented. In full field XRF experiments using the coded aperture a significant increase of up to factor 9.5 in count rate compared to identical experiments using polycapillary optics was found.

The recorded images of two samples could be reconstructed with four different methods, the convolution with a scaled antimask, the iterative reconstruction, the evolutionary algorithm and the MSDNet machine learning approach. It was possible to reconstruct the object with all four methods for different tested samples.

In the case of sample 2 no satisfactory results for the reconstructions were obtained. This is mainly due to the fact that the exact experimental parameters from the recorded data could not be extracted as there was no projection of the mask pattern and shows that it will be necessary to implement a standardized small point to the sample holder that ensures the projection of the mask at the same time as the sample is recorded.

The used mask has only 12 holes. A further increase in count rate can be expected when new masks with more holes are used. This will reduce the recording time for lower concentrations. Other mask patterns can also be tested. The MURA pattern is a good choice for CAI when the reconstruction is performed with an antimask. However, simulations suggested that other mask patterns might be better suited for iterative reconstruction, *e.g.*, random masks with random distances between the holes.

The hole size was $90\,\mu m$, which is the limiting factor for the resolution. In principle the detector allows to use a subpixel algorithm, described by Nowak *et al.*[78] to refine the detector pixel size, but as long as the hole size is substantially larger, this remains the limiting factor for the resolution. In the next experiments the gain in resolution when using multiple pinholes compared to one pinhole of the same size, as found in the resolution simulations, must be proven. In future experiments the gain in resolution by using smaller pinholes should be evaluated.

As the method has a high count rate compared to other full field optics and is much faster than the scanning method, it allows the fast detection of the elemental distribution in a 2D sample. For the moment, the results have only a qualitative character. In the long term, calibration should ensure that quantitative statements can also be made.

5 Conclusions

This work presented the implementation of new experimental possibilities at the BAM*line*. The developed methods help to extend BAM's wide expertise in the fields of synchrotron based X-ray absorption and X-ray fluorescence spectroscopy.

The first new method is time- and laterally-resolved XAFS spectroscopy based on dispersive XAFS. The developed setup consists of a so-called wafer bender for the flexible bending of a Si (111) wafer, an area sensitive CCD camera, and a frame that allows the independent rotation of wafer bender and camera with respect to the incoming beam as well as the adjustment of the distance between wafer and camera. Contrary to established dispersive XAFS methods the sample is placed in front of the bent wafer, hence only the transmitted X-rays are reflected and recorded by the detector. This setup allows the simultaneous detection of a whole XANES or EXAFS spectrum in down to 1 s, which is considerably faster than the conventional point-by-point acquisition, and is suitable for homogeneous samples.

Different tests with metal foils have been performed with this setup at the BAM*line*. The energy calibration that is necessary to assign an energy to every pixel in the detector image, has been performed experimentally and by simulation. The results showed good agreement for most cases. The setup has also been used for the time-resolved study of the early stages of ZIF-8-crystallization. Spectra were recorded with a time resolution of 2 s to follow the structural evolution of the coordination environment of zinc ions and gain insight into the synthesis process. The study helped to confirm tetrakis(2-MeIM)zinc2+ to be a key intermediate during ZIF-8 crystallization.

Beside the development of the setup and the experiments, the wafer bending has been investigated and the beam path has been calculated and simulated. The results from these simulations can be used to calculate the experimental parameters. A simulation of the beam path can help to optimize these parameters and to adapt them to the actual experiment, and to perform the energy calibration.

The lateral resolution of the setup has not been shown in this work. In principle, the vertical dimension of the beam can be used to investigate horizontally layered samples.

The presented setup is now available at the BAM*line* and can be used to perform time-resolved XANES and EXAFS studies, for example to follow chemical reactions, where the structural changes occur on the second timescale, or in-situ studies, where

the changes in a material are investigated depending on changing conditions. Further experiments should also include the use of lateral resolution using the vertical width of the beam, *e.g.*, to track gradients of oxidation states, *e.g.*, in catalyst materials.

The second part of this work deals with the implementation of a method for full field X-ray fluorescence imaging with coded apertures. This method allows the scanning-free recording of element distribution maps of a sample. The use of a coded aperture, that consists of many pinholes in an X-ray opaque material, yields a higher count rate compared to a single pinhole or a polycapillary optic. Furthermore, the transmission is not energy dependent, unlike when using polycalpillary optics.

The projection through multiple pinholes leads to overlapping images on the 2D energy-dispersive detector, a pnCCD. Therefore, a reconstruction step is an integral part of the method. Thus, a large part of this work was the development of programs for different reconstruction methods, including the reconstruction with an antimask, an iterative algebraic reconstruction, the reconstruction with an evolutionary algorithm and with a neural network.

As the iterative reconstruction and the evolutionary algorithm include the simulation of the projection process, a projection function was calculated for different experimental parameters. This projection function could be used for the simulation of experiments to better understand the performance of the system, *e.g.*, to compare the different reconstruction methods, and investigate the resolution of the system.

Tests at the BAM*line* could confirm an increase in count rate up to a factor of 9.5, depending on the sample and the geometrical arrangement of sample, optics and detector. Different samples were measured and most of them could be successfully reconstructed with the four different reconstruction methods.

As the method has a high count rate compared to other full field optics and is much faster than the scanning method, it allows the fast detection of the elemental distribution in a 2D sample and exploit the outstanding properties of the pnCCD.

Further developments of the method could lead to better results. The optimization possibilities are listed in the following:

The mask used in the experiments had only 12 holes. The increase in count rate will be more important when using more holes. Thus, the recording time can be further reduced.

The MURA pattern chosen for the mask is a good choice for the reconstruction with an antimask. Eventually, other patterns are better suited, when using other reconstruction methods, *e.g.*, random masks with random distances between the holes.

The hole size of the mask was $90\,\mu m$, which is the limiting factor for the resolution. As long as the hole size is the determining factor for the resolution, it is not practical to use a subpixel algorithm, described by Nowak *et al.*[78] to refine the detector pixel size, but when

the detector pixel size becomes the limiting factor for the resolution, *e.g.*, when smaller holes are used, this subpixel algorithm could be used to further enhance the resolution. The experimental resolution has not yet been determined. Further experiments are necessary to confirm the gain in resolution when using multiple pinholes compared to one pinhole of the same size, as found in the resolution simulations. In future experiments the gain in resolution by using smaller pinholes should be evaluated.

In principle, a calibration with samples with known elemental concentrations would allow quantification of elements.

On the side of the reconstruction algorithms, the optimization of the projection function remains a challenging task. The quality of the projection function is decisive for the quality of the reconstruction with the iterative or evolutionary algorithm. A realistic projection function could also help to produce realistic training data for the neural network.

Bibliography

[1] 2010; `https://www.nist.gov/pml/xcom-photon-cross-sections-database`.

[2] Hodoroaba, V. D.; Radtke, M.; Reinholz, U.; Riesemeier, H.; Vincze, L.; Reuter, D. X-ray scattering in X-ray fluorescence spectra with X-ray monochromatic, polarised excitation – Modelling, experiment, and Monte-Carlo simulation. *Nuclear Instruments and Methods in Physics Research Section B: Beam Interactions with Materials and Atoms* **2011**, *269*, 1493–1498.

[3] 2004; `https://www.nist.gov/pml/x-ray-mass-attenuation-coefficients`.

[4] Pietsch, U.; Holy, V.; Baumbach, T. *High-resolution X-ray scattering: from thin films to lateral nanostructures*, 2nd ed.; Springer-Verlag: New York, 2004.

[5] Van Grieken, R.; Markowicz, A. *Handbook of X-Ray Spectrometry*; CRC Press, 2001.

[6] Beckhoff, B.; Kanngießer, B.; Langhoff, N.; Wedell, R.; Wolff, H. *Handbook of Practical X-Ray Fluorescence Analysis*; Springer Berlin Heidelberg, 2007.

[7] Iwanenko, D.; Pomeranchuk, I. On the Maximal Energy Attainable in a Betatron. *Physical Review* **1944**, *65*, 343–343.

[8] Elder, F. R.; Gurewitsch, A. M.; Langmuir, R. V.; Pollock, H. C. Radiation from Electrons in a Synchrotron. *Physical Review* **1947**, *71*, 829–830.

[9] Martensson, N.; Eriksson, M. The saga of MAX IV, the first multi-bend achromat synchrotron light source. *Nuclear Instruments and Methods in Physics Research Section A: Accelerators, Spectrometers, Detectors and Associated Equipment* **2018**, *907*, 97–104.

[10] Liu, L.; Milas, N.; Mukai, A. H. C.; Resende, X. R.; de Sa, F. H. The Sirius project. *Journal of Synchrotron Radiation* **2014**, *21*, 904–911.

[11] Liuzzo, S. M.; Carmignani, N.; Franchi, A.; Perron, T.; Scheidt, K. B.; Taurel, E.; Torino, L.; White, S. M.; Iop, *10th International Particle Accelerator Conference*; Journal of Physics Conference Series; Iop Publishing Ltd: Bristol, 2019; Vol. 1350.

[12] Pollock, H. C. The discovery of synchrotron radiation. *American Journal of Physics* **1983**, *51*, 278 – 280.

[13] Buzanich, G. Characterization of Compound Refractive Lenses for synchrotron µ-XRF and µ-XAS and applications with high spatial resolution. Dissertation, 2012.

[14] Meirer, F. Applications of Synchrotron Radiation induced Total Reflection X-Ray Fluorescence Analysis in Absorption Spectroscopy. Dissertation, 2008.

[15] Schwinger, J. On the Classical Radiation of Accelerated Electrons. *Physical Review* **1949**, *75*, 1912 – 1925.

[16] Duke, P. *Synchrotron Radiation: Production and Properties*; Oxford University Press, 2000.

[17] Wiedemann, H. *Synchrotron Radiation*; Springer, 2003.

[18] Koch, E.; Brown, G.; Moncton, D. *Handbook on Synchrotron Radiation*; North Holland Publishing Company, 1987.

[19] `https://www.criticalmass-hamburg.de/wp-content/uploads/2019/02/die-wesentlichen-unterschiede-zwischen-einem-synchrotron-und-einem-zyklotron1.jpg`.

[20] Eberhardt, W. Synchrotron radiation: A continuing revolution in X-ray science—Diffraction limited storage rings and beyond. *Journal of Electron Spectroscopy and Related Phenomena* **2015**, *200*, 31–39.

[21] Jackson, J. D. *Classical Electrodynamics*; John Wiley and Sons, 1998.

[22] Mills, D.; Helliwell, J.; Kvick, A.; Ohta, T.; Robinson, I.; Authier, A. Report of the Working Group on Synchrotron Radiation Nomenclature – brightness, spectral brightness or brilliance? *Journal of Synchrotron Radiation* **2005**, *12*, 385.

[23] Thomson, A.; Attwood, D.; Gullikson, E.; Howells, M.; Kim, K.-J.; Kirz, J.; Kortright, J.; Lindau, I.; Liu, Y.; Pianetta, P.; Robinson, A.; Scofield, J.; Underwood, J.; Williams, G.; Winick, H. *X-Ray Data Booklet*; 2009.

[24] Batrakov, A.; Bekhtenev, E.; Borovikov, V.; Djurba, V.; Fedurin, M.; Repkov, V.; Karpov, G.; Khruschev, S.; Kulipanov, G.; Kuzin, M. Superconducting Wavelength Shifters and Multipole Wigglers Developed in Budker INP. Proceedings of the Second Asian Particle Accelerator Conference. 2001; pp 251–253.

[25] https://photon-science.desy.de/research/students__teaching/primers/synchrotron_radiation/index_eng.html.

[26] Klementiev, K.; Chernikov, R. *Powerful scriptable ray tracing package xrt*; SPIE Optical Engineering + Applications; SPIE, 2014; Vol. 9209.

[27] Riesemeier, H.; Ecker, K.; Görner, W.; Müller, B. R.; Radtke, M.; Krumrey, M. Layout and first XRF applications of the BAMline at BESSY II. *X-Ray Spectrometry* **2005**, *34*, 160–163.

[28] Schäfers, F. In *Modern Developments in X-Ray and Neutron Optics*; Erko, A., Idir, M., Krist, T., Michette, A. G., Eds.; Springer Berlin Heidelberg: Berlin, Heidelberg, 2008; pp 9–41.

[29] Görner, W.; Hentschel, M.; Müller, B. R.; Riesemeier, H.; Krumrey, M.; Ulm, G.; Diete, W.; Klein, U.; Frahm, R. BAMline: the first hard X-ray beamline at BESSY II. *Nuclear Instruments and Methods in Physics Research A* **2001**, *467-468*, 703–706.

[30] Newville, M. Fundamentals of XAFS. **2004**,

[31] Stern, E. A. Theory of the extended x-ray-absorption fine structure. *Physical Review B* **1974**, *10*, 3027 – 3037.

[32] Lytle, F. W.; Sayers, D. E.; Stern, E. A. Extended x-ray-asorption fine-structure technique. II. Experimental practice and selected results. *Physical Review B* **1975**, *11*, 4825 – 4835.

[33] Stern, E. A.; Sayers, D. E.; Lytle, F. W. Extended x-ray-absorption fine-structure technique. III. Determination of physical parameters. *Physical Review B* **1975**, *11*, 4836 – 4846.

[34] Rehr, J. J.; Albers, R. C. Theoretical approaches to x-ray absorption fine structure. *Reviews of Modern Physics* **2000**, *72*, 621–654.

[35] Rehr, J. J.; Kas, J. J.; Prange, M. P.; Sorini, A. P.; Takimoto, Y.; Vila, F. Ab initio theory and calculations of X-ray spectra. *Comptes Rendus Physique* **2009**, *10*, 548–559.

[36] Rehr, J. J.; Kas, J. J.; Vila, F. D.; Prange, M. P.; Jorissen, K. Parameter-free calculations of X-ray spectra with FEFF9. *Physical Chemistry Chemical Physics* **2010**, *12*, 5503–5513.

[37] Joly, Y. X-ray absorption near-edge structure calculations beyond the muffin-tin approximation. *Physical Review B* **2001**, *63*, 125120.

[38] Ravel, B.; Newville, M. ATHENA, ARTEMIS, HEPHAESTUS: data analysis for X-ray absorption spectroscopy using IFEFFIT. *J Synchrotron Radiat* **2005**, *12*, 537–41.

[39] Kirby, J. A.; Goodin, D. B.; Wydrzynski, T.; Robertson, A.; Klein, M. P. State of Manganese in the Photosynthetic Apparatus. 2. X-ray Absorption Edge Studies on Manganese in Photosynthetic Membranes. *Journal of the American Chemical Society* **1981**, *103*, 5537 – 5542.

[40] Guda, A.; Guda, S. A.; Martinin, A.; Bugaev, A.; Soldatov, M.; Soldatov, A. V.; Lamberti, C. Machine learning approaches to XANES spectra for quantitative §D structural determination: The case of CO2 adsorption on CPO-27-Ni MOF. *Radiation Physics and Chemistry* **2020**, *175*.

[41] Vanhoof, C.; Bacon, J. R.; Ellis, A. T.; Fittschen, U. E. A.; Vincze, L. 2019 atomic spectrometry update – a review of advances in X-ray fluorescence spectrometry and its special applications. *Journal of Analytical Atomic Spectrometry* **2019**, *34*, 1750–1767.

[42] Frahm, R. Quick scanning exafs: First experiments. *Nuclear Instruments and Methods in Physics Research Section A: Accelerators, Spectrometers, Detectors and Associated Equipment* **1988**, *270*, 578–581.

[43] Frahm, R.; Stuetzel, J.; Luetzenkirchen-Hecht, D. State of the art Quick-EXAFS: Applications in Catalysis. **2009**,

[44] Müller, O.; Lützenkirchen-Hecht, D.; Frahm, R. Instrumentation for QEXAFS Spectroscopy at P64. **2013**,

[45] Mueller, O.; Nachtegaal, M.; Just, J.; Lutzenkirchen-Hecht, D.; Frahm, R. Quick-EXAFS setup at the SuperXAS beamline for in situ X-ray absorption spectroscopy with 10 ms time resolution. *J Synchrotron Radiat* **2016**, *23*, 260–6.

[46] Mathon, O.; Beteva, A.; Borrel, J.; Bugnazet, D.; Gatla, S.; Hino, R.; Kantor, I.; Mairs, T.; Munoz, M.; Pasternak, S.; Perrin, F.; Pascarelli, S. The time-resolved and extreme conditions XAS (TEXAS) facility at the European Synchrotron Radiation Facility: the general-purpose EXAFS bending-magnet beamline BM23. *J Synchrotron Radiat* **2015**, *22*, 1548–54.

[47] Matsushita, T.; Phizackerley, R. P. A Fast X-Ray Absorption Spectrometer for Use with Synchrotron Radiation. *Japanese Journal of Applied Physics* **1981**, *20*, 2223.

[48] Flank, A. M.; Fontaine, A.; Jucha, A.; Lemonnier, M.; Raoux, D.; Williams, C. EXAFS in dispersive mode. *Nuclear Instruments and Methods in Physics Research* **1983**, *208*, 651–654.

[49] Dartyge, E.; Depautex, C.; Dubuisson, J. M.; Fontaine, A.; Jucha, A.; Leboucher, P.; Tourillon, G. X-ray absorption in dispersive mode: A new spectrometer and a data acquisition system for fast kinetics. *Nuclear Instruments and Methods in Physics Research Section A: Accelerators, Spectrometers, Detectors and Associated Equipment* **1986**, *246*, 452–460.

[50] Ukyo, K.; Tadashi, M.; Kazutake, K. A Dispersive Method of Measuring Extended X-Ray Absorption Fine Structure. *Japanese Journal of Applied Physics* **1981**, *20*, L355.

[51] S. Pascarelli, S. D. P., T. Neisius Turbo-XAS: dispersive XAFS using sequential acquisition. *J. Synchritron Rad.* **1999**, *6*, 1044–1050.

[52] Pascarelli, S.; Aquilanti, G.; Dubrovinsky, L.; Guilera, G.; Mathon, O.; Munoz, M.; Newton, M.; Pasquale, M.; Trapananti, A. Dispersive XAS on a High Brilliance Source: Highlights and Future Opportunities. AIP Conference Proceedings. p 608.

[53] Baudelet, F.; Kong, Q.; Nataf, L.; Cafun, J. D.; Congeduti, A.; Monza, A.; Chagnot, S.; Itié, J. P. ODE: a new beam line for high-pressure XAS and XMCD studies at SOLEIL. *High Pressure Research* **2011**, *31*, 136–139.

[54] Diaz-Moreno, S.; Hayama, S.; Amboage, M.; Freeman, A.; Sutter, J.; Duller, G. I20; the Versatile X-ray Absorption spectroscopy beamline at Diamond Light Source. *Journal of Physics: Conference Series* **2009**, *190*.

[55] Katayama, M.; Miyahara, R.; Watanabe, T.; Yamagishi, H.; Yamashita, S.; Kizaki, T.; Sugawara, Y.; Inada, Y. Development of dispersive XAFS system for analysis of time-resolved spatial distribution of electrode reaction. *Journal of Synchrotron Radiation* **2015**, *22*, 1227–1232.

[56] Terzano, R.; Denecke, M. A.; Falkenberg, G.; Miller, B.; Paterson, D.; Janssens, K. Recent advances in analysis of trace elements in environmental samples by X-ray based techniques (IUPAC Technical Report). *Pure and Applied Chemistry* **2019**, *91*, 1029–1063.

[57] Cavallari, E.; Frontera, F. Hard X-Ray/Soft Gamma-Ray Experiments and Missions: Overview and Prospects. *Space Science Reviews* **2017**, *212*, 429–518.

[58] Accorsi, R. Design of near-field coded aperture cameras for high-resolution medical and industrial gamma-ray-imaging. Doctor thesis, 2001.

[59] Rauwolf, M.; Turyanskaya, A.; Roschger, A.; Prost, J.; Simon, R.; Scharf, O.; Radtke, M.; Schoonjans, T.; Guilherme Buzanich, A.; Klaushofer, K.; Wobrauschek, P.; Hofstaetter, J. G.; Roschger, P.; Streli, C. Synchrotron radiation micro X-ray fluorescence spectroscopy of thin structures in bone samples: comparison of confocal and color X-ray camera setups. *J Synchrotron Radiat* **2017**, *24*, 307–311.

[60] Grunwaldt, J.-D.; Schroer, C. G. Hard and soft X-ray microscopy and tomography in catalysis: bridging the different time and length scales. *Chemical Society Reviews* **2010**, *39*, 4741–4753.

[61] Kirkpatrick, P.; Baez, A. V. Formation of Optical Images by X-Rays. *Journal of the Optical Society of America* **1948**, *38*, 766–774.

[62] Snigirev, A.; Kohn, V.; Snigireva, I.; Lengeler, B. A compound refractive lens for focusing high-energy X-rays. *Nature* **1996**, *384*, 49–51.

[63] MacDonald, C. A. Focusing Polycapillary Optics and Their Applications. *X-Ray Optics and Instrumentation* **2010**, *2010*, 1–17.

[64] Dicke, R. H. Scatter-hole cameras for X-rays and gamma rays. *The Astrophysical Journal* **1968**, *153*, L101 – L106.

[65] Ables, J. G. Fourier Transform Photography: A New Method for X-Ray Astronomy. *Publications of the Astronomical Society of Australia* **1968**, *1*, 172–173.

[66] Caroli, E.; Stephen, J. B.; Di Cocco, G.; Natalucci, L.; Spizzichino, A. Coded aperture imaging in X- and gamma-ray astronomy. *Space Science Reviews* **1987**, *45*, 349–403.

[67] Cieślak, M. J.; Gamage, K. A. A.; Glover, R. Coded-aperture imaging systems: Past, present and future development – A review. *Radiation Measurements* **2016**, *92*, 59–71.

[68] Haboub, A.; MacDowell, A. A.; Marchesini, S.; Parkinson, D. Y. *Coded Aperture Imaging for Fluorescent X-rays-Biomedical Applications*; Conference: Fully Three-Dimensional Image Reconstruction in Radiology and Nuclear Medicine,

Granlibakken, Lake Tahoe, June 16 to June 21, 2013; ; Ernest Orlando Lawrence Berkeley National Laboratory, Berkeley, CA (US), 2013; p Medium: ED; Size: 4.

[69] Haboub, A.; MacDowell, A. A.; Marchesini, S.; Parkinson, D. Y. Coded aperture imaging for fluorescent x-rays. *Rev Sci Instrum* **2014**, *85*, 063704.

[70] Sowa, K. M.; Last, A.; Korecki, P. Grid-enhanced X-ray coded aperture microscopy with polycapillary optics. *Sci Rep* **2017**, *7*, 44944.

[71] Dąbrowski, K. M.; Dul, D. T.; Korecki, P. X-ray imaging inside the focal spot of polycapillary optics using the coded aperture concept. *Optics Express* **2013**, *21*, 2920–2927.

[72] Kohman, T. P. Coded-aperture x- or gamma-ray telescope with least-squares image reconstruction. I. Design considerations. *Review of Scientific Instruments* **1989**, *60*, 3396–3409.

[73] Geyer, L. L.; Schoepf, U. J.; Meinel, F. G.; Nance, J. W.; Bastarrika, G.; Leipsic, J. A.; Paul, N. S.; Rengo, M.; Laghi, A.; De Cecco, C. N. State of the Art: Iterative CT Reconstruction Techniques. *Radiology* **2015**, *276*, 339–357.

[74] Yang, X.; van Ommen, J. R.; Mudde, R. F. Comparison of genetic algorithm and algebraic reconstruction for X-ray tomography in bubbling fluidized beds. *Powder Technology* **2014**, *253*, 626–637.

[75] Bautu, A.; Bautu, E.; Popa, C.; Luchian, H. Improving Image Reconstruction with Evolutionary Algorithms. 7th Balkan Conference on Operational Research. 2005.

[76] Ducros, N.; Lorente Mur, A.; Peyrin, F. A Completion Network for Reconstruction from Compressed Acquisition. *hal-02342766* **2019**,

[77] Scharf, O. et al. Compact pnCCD-Based X-ray Camera with High Spatial and Energy Resolution: A Color X-ray Camera. *Analytical Chemistry* **2011**, *83*, 2532–2538.

[78] Nowak, S. H.; Bjeoumikhov, A.; von Borany, J.; Buchriegler, J.; Munnik, F.; Petric, M.; Radtke, M.; Renno, A. D.; Reinholz, U.; Scharf, O.; Wedell, R. Sub-pixel resolution with a color X-ray camera. *Journal of Analytical Atomic Spectrometry* **2015**, *30*, 1890–1897.

[79] Nowak, S. H.; Petric, M.; Buchriegler, J.; Bjeoumikhov, A.; Bjeoumikhov, Z.; von Borany, J.; Munnik, F.; Radtke, M.; Renno, A. D.; Reinholz, U.; Scharf, O.;

Tilgner, J.; Wedell, R. Road to micron resolution with a color X-ray camera - polycapillary optics characterization. **2017**,

[80] Buchriegler, J.; Klingner, N.; Hanf, D.; Munnik, F.; Nowak, S. H.; Scharf, O.; Ziegenrücker, R.; Renno, A. D.; von Borany, J. Enhancements in full-field PIXE imaging - Large area elemental mapping with increased lateral resolution dvoid of optics artefacts. *X-Ray Spectrom.* **2018**, *47*, 327–338.

[81] Ceglio, N. M.; Sweeney, D. W. In *Progress in Optics*; Wolf, E., Ed.; Elsevier, 1984; Vol. 21; pp 287–354.

[82] Gourlay, A. R.; Stephen, J. B. Geometric coded aperture masks. *Applied Optics* **1983**, *22*, 4042–4047.

[83] Gourlay, A.; Stephe, J.; Young, N. Geometrically designed coded aperture mask arrays. *Nuclear Instruments and Methods in Physics Research* **1984**, *221*, 54 – 55.

[84] Golay, M. J. E. Point Arrays Having Compact, Nonredundant Autocorrelations. *Journal of the Optical Society of America* **1971**, *61*, 272–273.

[85] Gottesman, S. R.; Fenimore, E. E. New family of binary arrays for coded aperture imaging. *Applied Optics* **1989**, *28*, 4344–4352.

[86] Busboom, A.; Elders–Boll, H.; Schotten, H. D. Uniformly Redundant Arrays. *Experimental Astronomy* **1998**, *8*, 97–123.

[87] Fenimore, E. E. Coded aperture imaging: the modulation transfer function for uniformly redundant arrays. *Applied Optics* **1980**, *19*, 2465 – 2471.

[88] Skinner, G. K. Imaging with Coded-Aperture Masks. *Nuclear Instruments and Methods in Physics Research* **1984**, *221*, 33 – 40.

[89] Skinner, G. K. Coding (and decoding) coded mask telescopes. *Experimental Astronomy* **1995**, *6*, 1 – 7.

[90] Pelt, D. M.; Sethian, J. A. A mixed-scale dense convolutional neural network for image analysis. *Proc Natl Acad Sci U S A* **2018**, *115*, 254–259.

[91] `https://github.com/dmpelt/msdnet`.

[92] Ordavo, I. et al. A new pnCCD-based color X-ray camera for fast spatial and energy-resolved measurements. *Nuclear Instruments and Methods in Physics Research Section A: Accelerators, Spectrometers, Detectors and Associated Equipment* **2011**, *654*, 250–257.

[93] Kulow, A.; Buzanich, A. G.; Reinholz, U.; Emmerling, F.; Hampel, S.; Fittschen, U. E. A.; Streli, C.; Radtke, M. Comparison of three reconstruction methods based on deconvolution, iterative algorithm, and neural network for X-ray fluorescence spectroscopy with coded apertures. *Journal of Analytical Atomic Spectrometry* **2020**, 1423–1434.

Appendix

Curriculum Vitae

Personal

Name	Anicó Kulow
Address	Eisenacher Str. 66
	12109 Berlin, Germany
Email	a.kulow@gmx.net
Date of birth	02.12.1986 in Berlin
Nationality	German

Professional Experience

since September 2016	**PhD student at BAM, Berlin** Development of spectroscopic methods
May 2015 - September 2016	**Freelance editor** Projects in the textbook area Manuscript and author work
November 2012 - January 2013	**Institute of Physics, Humboldt-University, Berlin** Student assistant in the basic practical course (physics) Preparation and implementation of experiments Correction and evaluation of experiment protocols
March 2011 - May 2015	**Cornelsen Schulverlage GmbH, Berlin** Trainee in the mathematics editorial office Manuscript work an corrections Communication with authors, editors and service providers

Formation

October 2010 - March 2015	Master of Physics, Humboldt-University, Berlin Specialisation: Statistical physics and nonlinear dynamics **Degree: Master of Science; Grade 1.2**
October 2007 - October 2010	Bachelor of Physics, Humboldt-University, Berlin Major subject physics, minor subject mathematics **Degree: Bachelor of Science; Grade 1.4**
August 1999 - July 2006	Luise-Henriette-Schule (Gymnasium), Berlin **High school graduation; Grade 1.2**
August 2003 - July 2004	Lycée Henri Poincaré, Nancy, France **Baccalauréat in French (verbal/written)**

Internships

31.08.2009 - 02.10.2009	**Paul-Klee-Grundschule, Berlin** Intern in a mixed class (1st to 3rd grade)
October 2011 - June 2007	**Advertising angency Frenkelson, Potsdam** Assistance with the organization of an education fair Communication with service providers Exhibitor acquisition and support Reports to the client (Stadt Potsdam)
13.08.2007 - 21.09.2007	**Max Planck Institute of colloids and interfaces, Berlin** Intern in the electronic workshop Conception, manufacture and repair of electronic devices Office work

Languages

German	Native language
English	oral and written very good
French	oral and written very good

IT

MS Office	Daily competent use of Word, Excel, PowerPoint
C++, IDL	Extendet basic knowledge
Python	Daily competent use
LaTeX	Independent use

Publications

A. Kulow, S. Witte, S. Beyer, A.G. Buzanich, M. Radtke, U. Reinholz, H. Riesemeier, and C. Streli, Journal of Analytical Atomic Spectrometry, 2019, 34 (1), 239 - 246.

A. Kulow, A.G. Buzanich, U. Reinholz, C. Streli, and M. Radtke, Journal of Analytical Atomic Spectrometry, 2020, 35 (2), 347 - 356.

A. Kulow, A.G. Buzanich, U. Reinholz, F. Emmerling, S. Hampel, U.E.A. Fittschen, C. Streli, and M. Radtke, Journal of Analytical Atomic Spectrometry, 2020, 35, 1423 - 1434.

Participation in conferences

2017	CSI XL Congress 2017, Pisa, Italy: Poster
2019	Adlershofer Forschungsforum, Berlin, Germany: Poster
	Anakon, Münster, Germany: Oral presentation
	BESSY Usermeeting, Berlin, Germany: Poster
	PRORA, Berlin, Germany: Poster
	SXR, Berlin, Germany: Poster
	Symposium IRIS, Berlin, Germany: Poster
	BAM PhD-Day, Berlin, Germany: Poster
2020	CONEXS, Newcastle, Great Britain: Poster prize
	BAM PhD-Day, Berlin, Germany: Pitch winner